Study on high resolution and speckle reduction optical coherence tomography using tunable quasi-supercontinuum laser source

Chen Ying

2024

Nagoya University
Graduate School of Engineering

Contents

Chapter 1 Introduction 1
1.1 General Introduction 1
1.2 Optical coherence tomography 1
1.2.1 High-speed highly sensitive OCT (SD-OCT) 3
1.2.2 High-resolution OCT imaging (broadband light source) 4
1.2.3 Deep tissue OCT imaging (detection light wavelength) 7
1.2.4 Image contrast-enhanced OCT (speckle reduction) 8
1.3 Purpose and organization of this thesis 11
Reference for Chapter 1 14
Chapter 2 Theory of optical coherence tomography 20
2.1 Introduction 20
2.2 Michelson interferometer 20
2.2.1 Interferometer with coherent light 20
2.2.2 Axial resolution 22
2.2.3 Confocal grating and lateral resolution 25
2.3 Time-domain and Fourier-domain optical coherence tomography 27
2.3.1 Time-domain (TD) OCT 27
2.3.2 Fourier-domain (FD) OCT 28
2.4 Spectral domain (SD) optical coherence tomography 31
2.4.1 Axial resolution limits for OCT 31
2.4.2 Sensitivity and dynamic range in OCT 33
2.5 Speckle origins in OCT 35
2.6 Summary 36
Reference for Chapter 2 37
Chapter 3 Supercontinuum and quasi-supercontinuum sources for OCT 38
3.1 Introduction 38
3.2 Supercontinuum (SC) generation 38
3.3 Quasi-supercontinuum (SC) generation 39
3.3.1 Wavelength-tunable ultrashort pulse generation 39
3.3.2 Quasi-SC generation 40
3.4 Pulse propagation in fibers 42
3.4.1 Fiber loss 42
3.4.2 Chromatic dispersion 43

3.4.3 Nonlinear effects 45
3.4.4 Soliton effect 49
3.5 Summary 51
Reference for Chapter 3 52
Chapter 4 Development of tunable quasi-supercontinuum laser source 53
4.1 Introduction 53
4.2 Principle of quasi-supercontinuum generation 55
4.3 Experimental setup for quasi-supercontinuum laser source 56
4.3.1 Ultrashort pulse fiber laser using a single-wall carbon nanotube (SWNT) polyimide film 57
4.3.2 Wavelength-tunable ultrashort pulse generation using polarization-maintaining (PM) fiber 59
4.3.3 Tunable Gaussian-like quasi-supercontinuum (SC) generation by fast intensity modulation 62
4.4 Results 65
4.5 Summary 68
Reference for Chapter 4 69
Chapter 5 High resolution and larger penetration depth imaging using 1.7 μm broadband quasi-supercontinuum (SC) 72
5.1 Introduction 72
5.2 Broadband quasi-supercontinuum (SC) generation and experimental setup for SD-OCT 73
5.3 Characteristics of SD-OCT imaging 74
5.3.1 Imaging sensitivity and axial resolution 74
5.3.2 Lateral resolution 77
5.3.3 Imaging depth 80
5.4 Imaging results 82
5.5 Discussion 86
5.6 Summary 86
Reference for Chapter 5 88
Chapter 6 Speckle reduction imaging using tunable quasi-supercontinuum generation 89
6.1 Introduction 89
6.2 Tunable quasi-supercontinuum (SC) generation and characteristics in tissue imaging 91
6.2.1 Wavelength-tunable quasi-SC generation 91
6.2.2 Imaging characteristics using multiple spectral quasi-SCs 92
6.3 Speckle-reduced imaging by spectral compounding 94
6.3.1 Imaging of tape stacks 94
6.3.2 Imaging of pig thyroid gland 97
6.4 Discussion 101
6.5 Summary 101

Reference for Chapter 6 103
Chapter 7 Conclusions 105
7.1 Summary of this thesis 105
7.2 Outlook for the future 106
Reference for Chapter 7 108
Acknowledgment 109

Chapter 1 Introduction

1.1 General Introduction

In a life system, such as the human body, various enzymatic reactions, transcription and translation of genetic information, immune responses, and the occurrence of complex and highly intricate life phenomena, such as diseases, are constantly taking place. Understanding these life phenomena holds significant value for fundamental biology in exploring the essence of "life" and for medical research in studying disease mechanisms, treatment methods, and prevention strategies. In the process of understanding life phenomena, biomedical imaging methods that directly visualize these phenomena are a crucial technology. The spatiotemporal information obtained from images can assist us in comprehending complex life phenomena more simply and deeply. In the imaging of life phenomena, optical imaging methods with minimal damage to the biological entity and high spatial resolution are powerful tools [1-5].

Since the 1990s, optical coherence tomography (OCT) with micrometer resolution and cross-sectional imaging capabilities has become a prominent biomedical tissue-imaging technique, which continuously picked up new technical capabilities and was gradually being applied to diagnostics in fields such as ophthalmology, gastroenterology, and cardiology. OCT has always been dedicated to fine-scale structure imaging with higher resolution, larger penetration depth, and enhanced image contrast with more detailed information. The progress of OCT imaging technology is inseparable from innovations in the detection light source, as the detection light source largely determines the imaging performance of OCT, including sensitivity, resolution, penetration depth, and so on [6-8].

This thesis deals with research on 1.7 μm spectral tunable quasi-supercontinuum (SC) source with respect to different applications in biological imaging. The main focus was quasi-SC generation based on wavelength tunable ultrashort pulse source, where the insertion of a fast-optical intensity modulator enables the output ultrashort pulse tuning with high speed. In this way, the quasi-SC spectrum was observed with high tunability in terms of spectral shape, bandwidth, and wavelength range, due to the adjustable intensity modulation function. The successful application in the field of biological imaging is optical coherence tomography (OCT), where quasi-SC sources allow for both high-resolution deep tissue imaging and speckle-reduced imaging. Several characteristics of OCT using quasi-SC, such as sensitivity, axial resolution, lateral resolution, penetration depth, and imaging contrast were investigated.

In this chapter, I describe the background of this thesis. First, Section 1.2 presents the background of OCT, and describes the development with respect to the imaging speed, sensitivity, spatial resolution, penetration depth, and imaging contrast. The development in these aspects relies on innovations in SD-OCT detection methods, and the choice of light sources. Finally, the aims and organization of this thesis are described in Section 1.3.

1.2 Optical coherence tomography

Biomedical imaging is a vital and invaluable tool that enhances our understanding of biological structures, processes, and events by visualizing and portraying them. This technique is capable of detecting and describing features and characteristics related to the structure and function of biological tissues [1,9]. Its applications extend beyond clinical diagnosis and treatment, encompassing a wide range of uses in biological and medical research and investigations. Biomedical imaging began with the discovery of X-rays in the late

1800s, and chest X-ray imaging became one of those early applications [9]. The era of modern biological medical imaging did not begin until the 1970s. This modern era was once again ushered in by an X-ray imaging device called a "CAT" scanner or computed tomography, later shortened to computed tomography, or CT [9]. From the 1970s to the early years of this century, in just a short span of thirty years, various biomedical imaging technologies such as ultrasound imaging, X-ray CT, and magnetic resonance imaging (MRI) have undergone development and have been applied in clinical healthcare and biomedical investigation.

In clinical care and biomedical research, OCT is a commonly used imaging and measurement technique that emerged in the early 1990s and has rapidly developed over the past few decades. Essentially, OCT is a low-coherence interferometry modality capable of non-invasive, high-resolution (micron-level), cross-sectional, and three-dimensional imaging of biomedical tissues [6,7]. Its principles are similar to ultrasound imaging, but OCT uses near-infrared (NIR) light instead of sound waves as the light source for scanning samples. In comparison to some other commonly used biomedical imaging technologies in clinical medicine, OCT exhibits relatively high axial resolution, ranging from a few micrometers to about 10 micrometers [8]. Additionally, unlike confocal microscopy, CT, MRI, and ultrasound imaging, OCT is able to provide deeper tomographic imaging. For the above reasons, OCT is considered a technology that fills the gap between various biomedical imaging techniques, enabling high-resolution and depth-resolved in vivo imaging of biological structures, as illustrated in Fig.1.1 [1,8]. Due to these advantages, OCT has garnered significant attention from biomedical engineers and researchers, being recognized as a highly promising imaging technology in the fields of biology and medicine.

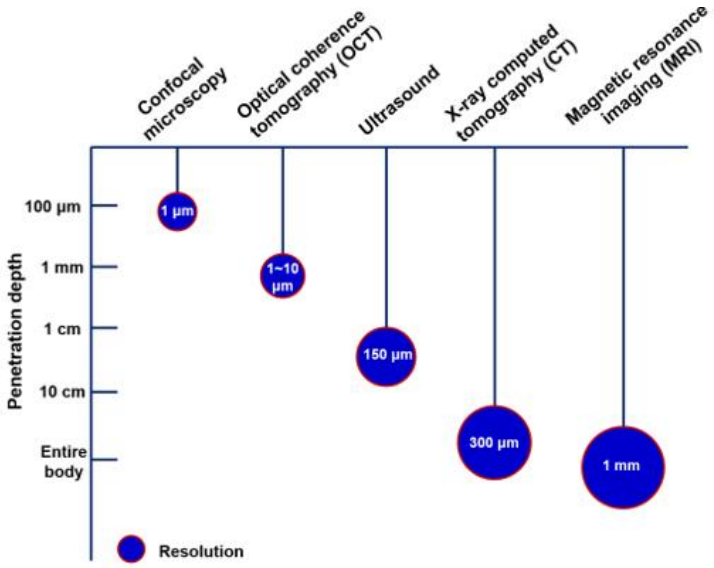

Fig. 1.1 Comparison of resolution and penetration depth between OCT and other biological imaging technologies [8].

The concept of OCT was first demonstrated by James G. Fujimoto *et al.* in 1991 [6]. The technique was originally intended for noninvasive cross-sectional imaging of the human retina and the coronary artery. The first OCT equipment was commercialized in 1994 and was used in ophthalmic clinical practice [10-12]. This allowed physicians to view fundus structures with high resolution and sensitivity without the need for surgery. As the technology evolved, OCT began to be used in the detection of neoplastic changes. Early studies were

performed *ex vivo* to correlate OCT images with histology for gastrointestinal [13-16], biliary [17], female reproductive [18,19], pulmonary [20], and urinary [21,22] pathologies. Its high resolution and non-invasive nature made it a powerful tool for viewing tissue structures. Since then, OCT technology has continued to improve and innovate around imaging speed, sensitivity, spatial resolution, penetration depth, and image contrast, enabling it to become a powerful tool in medical and biological research.

1.2.1 High-speed highly sensitive OCT (SD-OCT)

First-generation OCT systems before 1995 employed time-domain detection with an interferometer using a low-coherence light source and scanning reference delay arm, called time-domain (TD) OCT [23]. The development of Fourier-domain detection enabled a breakthrough in OCT imaging sensitivity and speed. The utilization of high-speed diffraction grating dispersion-compensating delay scanners has enabled OCT imaging speeds of several thousand axial scans per second and video rate imaging [24,25]. In 1995, the implementation of spectral domain (SD) OCT was first reported [26], classified as Fourier domain (FD) OCT. This approach exhibits significant advantages in signal-to-noise ratio (SNR), even though reports date back as early as 1997 [27,28]. However, it took approximately 50 years for this approach to gain full recognition in the OCT community, finally achieving widespread acceptance in 2003 [29-31]. In 2002, SD-OCT was first used for in *vivo* retinal imaging [32], and its sensitivity advantages in high-speed three-dimensional volumetric imaging [34], ultra-high-resolution video-rate imaging [35,36], and human retinal Doppler blood flow measurements [37,38] were subsequently fully realized. Pioneering studies by Nassif *et al.* demonstrated video-rate retinal imaging using SD-OCT with line scan cameras, achieving 29,000 axial scans per second with an axial image resolution of 6 μm [39].

The principle of SD-OCT can be comprehended by considering the Michelson interferometer as an aperiodic frequency filter, where the periodicity is determined by the path difference between the sample and reference arms. The interference of the two beams induces a spectral modulation based on frequency, and this modulation can be detected using a spectrometer. The periodicity of the modulation is inversely related to the echo time delay. Consequently, different echo delays give rise to distinct frequency modulations. The measurement of echo delays involves converting the spectrometer output from wavelength to frequency and subsequently applying a Fourier transform to the interference signal. This process yields an axial scan that provides information about the magnitude and echo delay of the light signal originating from the tissue. SD-OCT imaging enables the imaging speed of about 50-100 times greater than TD-OCT systems. Meanwhile, the superior sensitivity of SD-OCT, combined with the lack of need for a fast scanning mechanism, has opened up the possibility of much faster scanning without loss of image quality and provided a paradigm shift from point sampling to volumetric mapping of biological tissue. Figure 1.2 (a) shows a cross-section centered on the optic nerve head, while Figure 1.2(b) illustrates the corresponding *en-face* image derived from the 3-D dataset [23].

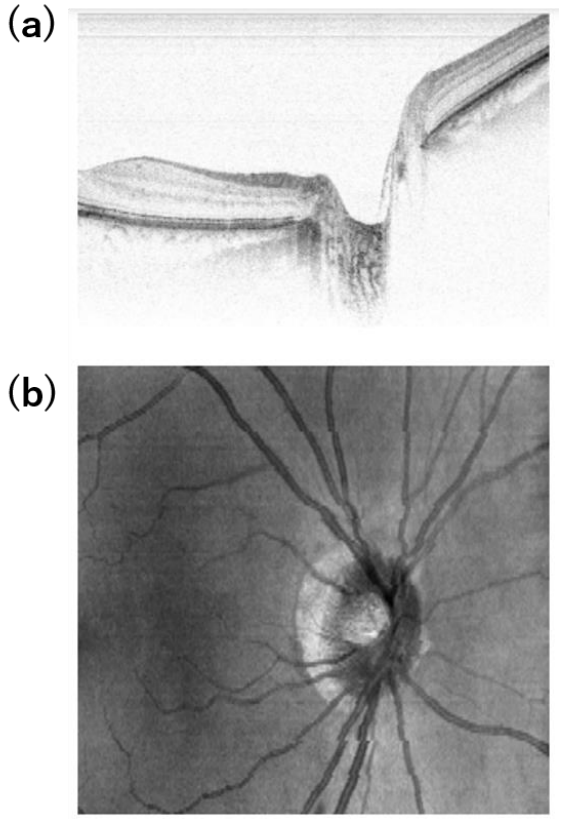

Fig. 1.2 (a) High-resolution SD-OCT image of a human retina in vivo, centered on the optic nerve head. (b) *En-face* reconstruction of the optic nerve head region of the retina from a volumetric SD-OCT data set [8].

Actually, there is another FD-OCT, which is based on wavelength-swept light sources, called as swept-source OCT (SS-OCT). SS-OCT employs high-speed, balanced photodetectors instead of a spectrometer and line-scan camera utilized in SD-OCT [23]. The use of photodetectors in SS-OCT leads to reduced detection losses compared to SD-OCT, owing to the enhanced efficiency of the photodetectors. Furthermore, SS-OCT demonstrates a significant reduction in parasitic signal roll-off with imaging depth—a characteristic present in SD-OCT. This improvement is attributed to the coherence properties of tunable lasers and the capacity to detect high-frequency signals using broad bandwidth detection and data acquisition systems. Notably, SS-OCT offers high-speed and high-sensitivity imaging. However, it is crucial to highlight that wavelength-swept lasers play a pivotal role in the technology of SS-OCT. The properties of swept source are very different from the light source developed in this thesis. Therefore, SS-OCT is not the focus of this study.

1.2.2 High-resolution OCT imaging (broadband light source)

OCT achieves very high axial image resolutions independent of focusing conditions because the axial and lateral resolutions are determined independently by different physical mechanisms. This implies that axial resolution can be enhanced using broad bandwidth, low-coherence length light sources, which is explained in Chapter 2. A minimum output power with low amplitude noise is also crucial for enabling high sensitivity

and high-speed real-time OCT imaging. Therefore, it is evident that the light source stands out as the key technological parameter for an OCT system, and making the proper choice is imperative [40].

When selecting a light source for OCT imaging, several key criteria must be taken into consideration. The characterization of a light source and its suitability for OCT can be evaluated based on: (1) central wavelength, (2) bandwidth and spectral shape, (3) averaged power, (4) noise, and (5) stability. So far, there are three common types of broadband light sources for high resolution OCT imaging, including superluminescent diode (SLD), solid-state laser, and supercontinuum (SC) source.

Superluminescent diodes (SLDs) are widely employed as the primary light sources in OCT due to their compact size and cost-effectiveness. The distinctive feature of SLDs lies in their ability to combine laser diode-like output power and brightness with a broad, LED-like optical spectrum. This unique combination is made possible by the high optical gain and wide gain spectrum found in semiconductor laser materials. Substantial enhancements in SLD performance parameters have led to the creation of highly powerful and broadband SLD-based light sources across various spectral bands, ranging from 680 to 1,600 nm. Currently, SLDs exhibit output power comparable to that of single-mode laser diodes and coherence length down to 10 mm and less, particularly at specific wavelengths. The utilization of "combined" SLD light sources, based on two or more SLDs, has enabled the generation of ultrahigh-resolution (2.5–3.5 μm) OCT images of the human eye and tissues. [41]. Table 1.1 shows the summary of SLDs specifications for OCT with respect to the active layer structure, power, and bandwidth. The bandwidths of SLDs are typically less than 100 nm with output power in the range of 10-200 mW.

Table 1.1 Gain material dependence of central wavelength, power, and bandwidth

Active materials	Active layer structure	Bandwidth [nm]	Power [mW]	Wavelength [nm]
AlGaInp	Bulk	8-10	4	680
	QW	8-10	50	
AlGaAs	Bulk	50	100~	780-870
	QW	50	50	
	Combined MQW	~100	-	
InGaAs	Bulk	70	30	920-980
	SQW	100	10	
InGaAs/GaAs	Heterostructure	-	10~	1050
	QD	60	200	
InGaAsP/InP	MQW/QD	60	10	1300-1600

The term solid-state laser typically refers to lasers that utilize a gain medium in crystalline or glass form, with ions introduced as an impurity in an otherwise transparent dielectric host material (whether in crystalline

or glass form). These lasers have been a subject of considerable research interest since the invention of the first ruby laser by Maiman in 1960 [40]. Various solid-state lasers offer optical gain across a wide frequency range, allowing for high output powers with ultrabroad bandwidth laser emission. Table 1.2 shows a comparison of optical properties of main broadband solid state laser materials for OCT. Solid-state lasers with a bandwidth of a few hundred nanometers and an output power of a few tens of milliwatts can achieve ultra-high axial resolution (<5 μm) for OCT imaging.

Table 1.2 Optical properties of broadband solid-state laser materials

Materials	Bandwidth [nm]	Power [mW]	Wavelength [nm]	Corresponding OCT axial resolution [μm]
Ti^{3+}:sapphire	176	20	776	1.7
Cr^{3+}:LiCAF	300	90	800	1.3
Cr^{4+}:Forsterite	210	50	1200	5
Cr^{4+}:YAG	190	-	1450	-

Supercontinuum (SC) sources have been investigated since their discovery in the late 1960s by Alfano and Shapiro [42]. Thanks to the excellent features of high output power, broad spectrum, and high degree of spatial coherence, SC generation has been widely studied for various applications, such as ultra-high-resolution OCT, multi-photon excited fluorescence microscopy, frequency metrology, extremely short pulse generation, and optical communications [43-46]. The development of highly nonlinear optical fiber brought a dramatic bandwidth expansion of over an octave [47, 48]. In 2001, Nishizawa and Goto demonstrated an all-fiber SC source emitting at around 1.55 μm by use of a passively mode-locked Er-doped fiber laser and highly nonlinear fiber [49]. Recently, because of investigating the principles of SC generation, high-quality SC has been generated [50-52].

Table 1.3 Optical properties of broadband light sources

	Wavelength [nm]	Bandwidth [nm]	Power [mW]
SLD	400-1700	< 100	10-200
Solid state laser	800-1500	< 300	< 100
SC	800-2000	100-400	10-100

The above description has outlined the primary options for broadband light sources. Table 1.3 provides an overview of the different broadband light sources for high axial resolution OCT. SC sources offer a broader bandwidth and a wider range of detection wavelengths compared to both SLDs and solid-state lasers.

1.2.3 Deep tissue OCT imaging (detection light wavelength)

The light source not only determines axial resolution via its bandwidth and central emission wavelength but also determines the penetration in the sample (biological tissue), and the lateral resolution.

Figure 1.3 shows the wavelength dependence of light attenuation caused by water absorption and light scattering at different wavelength ranges for biological tissue imaging. As the wavelength increases, the scattering of light by biological tissues decreases. There is a local minimum water absorption in the narrow wavelength ranges of 0.8, 1.1, 1.7, and 2.2 μm. When using optical imaging techniques to observe deeper positions within biological organisms with high resolution, near-infrared light (wavelength > 0.8 μm), which has fewer light-absorbing elements and less scattering compared to visible light (wavelength 0.4–0.8 μm), is employed as the light source [53-56]. Recent research in the field of biomedical imaging has indicated that in the imaging of highly scattering tissues using near-infrared light, signal attenuation caused by light scattering dominates over water absorption [57-60]. While past biomedical imaging primarily employed light sources with a wavelength of around 0.8 μm, researchers have been striving to achieve greater penetration depth by utilizing the 1.1 μm and 1.3 μm wavelength bands, where signal attenuation due to scattering is reduced. In practice, improvements in penetration depth have been achieved [61-66]. However, even when using light sources in the 1.1 μm and 1.3 μm bands, imaging of highly scattering tissues such as the brain and skin still faces limitations, with penetration depths typically ranging from a few hundred micrometers to about 1 millimeter, making it challenging to achieve sufficient depth for deep tissue observation.

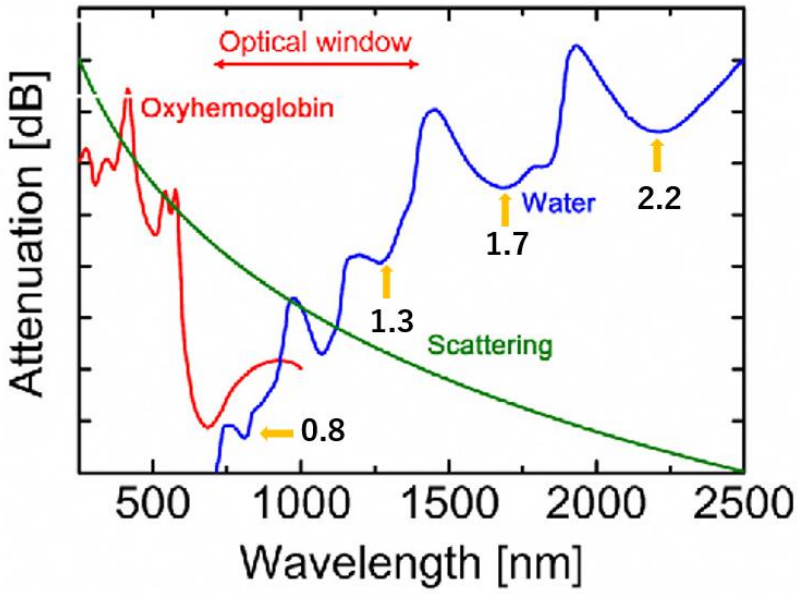

Fig.1.3 Wavelength dependence of light attenuation caused by water absorption and light scattering at different wavelength ranges [56].

In recent years, there has been significant attention on wavelength bands around 1.7 μm to achieve high-penetration biomedical imaging with depths exceeding 1 mm, as the signal attenuation due to scattering is even smaller than that in the 1.1 μm and 1.3 μm bands [67-69].

As mentioned above, considering both broadband width for high axial resolution and detection wavelength

range for deep tissue imaging, 1.7 μm SC source is a good choice for high resolution OCT with large penetration depth. It is reported that a maximum imaging depth of 1.6 mm in mouse brain imaging has been achieved by 1.7 μm light source [70]. Figures 1.4 show the OCT images of a mouse brain at different imaging depths and reconstructed OCT images.

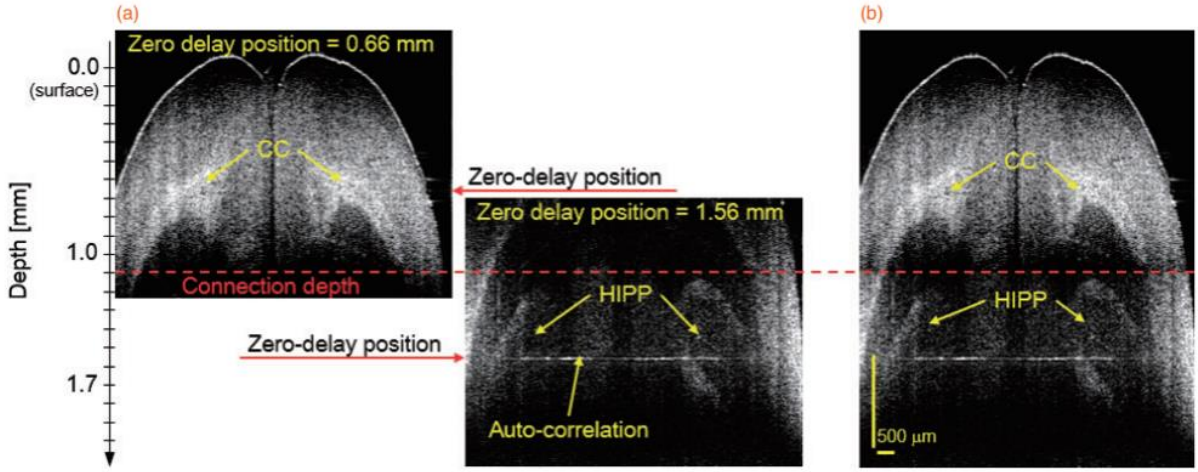

Fig. 1.4 (a) Full-range OCT images of a mouse brain at different imaging depths and (b) connected OCT image [70].

Furthermore, the wavelength of the Raman soliton pulse depends on the fiber length and the input laser power [71]. Therefore, by varying them, the wavelength-tunable soliton pulse can be generated. The wavelength of the soliton pulse can be tuned simply by controlling the input voltage into the AOM based on an all-fiber ultrashort pulse laser. This generation system of the wavelength-tunable soliton pulse is very simple and does not require troublesome operation in the wavelength-tuning. This development can be employed as the light source of SS-OCT. In 2008, Sumimura *et al.* developed a new broadband light source—a quasi- supercontinuum (SC) source based on the wavelength tunable pulse generation [72]. The quasi-SC source not only has similar spectral properties to SC, but also has a high tunability on spectra. The implementation of highly tunable quasi-SC on OCT enables a functional OCT, such as speckle-reduced OCT.

1.2.4 Image contrast-enhanced OCT (speckle reduction)

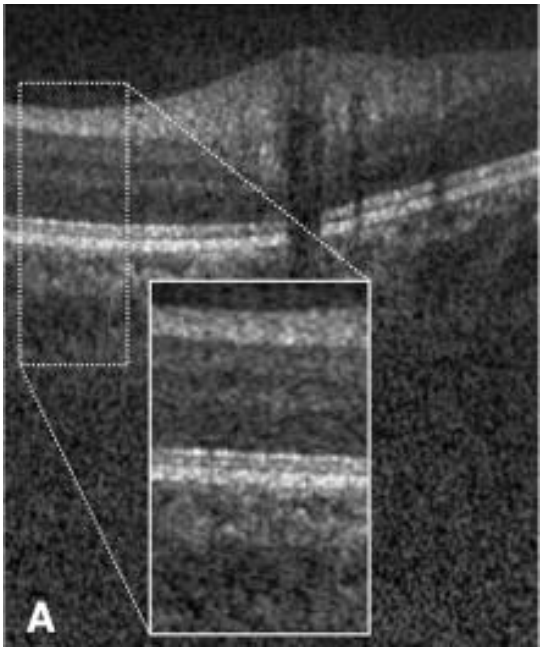

Fig. 1.5 Cross-sectional image of a human optic nerve head [73].

Figure 1.5 shows the OCT image of a human optic nerve head [73]. From the cross-sectional image, the boundaries for these retinal layers were blurred because of some dark and bright dot patterns. They are speckles. The appearance of speckle patterns degrades the image contrast and hinders the visibility of fine-scale structures, such as this layer structure.

Speckle is one of the most distracting artifacts of OCT images (as well as in other coherent ranging techniques like ultrasound). It is often difficult to distinguish the features caused by speckles from other features of interest. However, the phenomenon of speckle is what enables methods such as OCT to be useful. As the scatterers are typically randomly distributed in most objects, each frequency band used for probing the object contains useful details. This inherent property makes coherent ranging techniques practically useful. If the scatterers were not randomly distributed, leading to the absence of speckles, it's conceivable that probing an object within a specific frequency band might reveal no details at all (an example being the imaging of a Bragg grating with a resonant frequency outside the probed bandwidth). Unfortunately, when discerning details at the instrument's resolution limit, there is a likelihood that the details may be modulated by speckle, resulting in apparent noise [74].

Speckle arises when scatterers are distributed randomly, and the backscattered reflections from each scatterer superimpose with random phase and amplitude in the OCT interferogram. This phenomenon can be visualized as a "random walk" of two-dimensional vectors, each vector representing the complex-valued reflectance of an unresolved scatterer [74,75]. The summation of these vectors is approximated by a complex Gaussian random variable, with its length following a Rayleigh probability distribution. It's important to note that this implies the magnitude squared of the vector has an exponential or Boltzmann probability distribution. When considering multiple polarizations of the return signal, the magnitude squared of the reflectance aligns more closely with a gamma distribution [75-77]. The detailed origins of speckles are explained in Chapter 2.

Various approaches have been employed to tackle this persistent issue. They are categorized in two groups:

software-based and hardware-based methods, as shown in Table 1.4.

Table 1.4 Categories of speckle reduction methods

Hardware-based group	Software-based group
Amplitude compounding	Wavelet or curvelet transforms
Angular compounding	Non-local means algorithms
Frequency compounding	Sparse representation
Spatial compounding	…
…	

In the software group, one approach treats speckle as ordinary image noise and uses a common image denoising algorithm - spatially adaptive 2D wavelet filters to reduce speckle noise in OCT images. This method transforms speckles, considered as multiplicative noise, into additive noise by logarithmically transforming the OCT image amplitude. It enhances the discrimination of noise by exploiting correlations between wavelet coefficients at multiple scales, arising from object features. This enables the removal of uncorrelated speckle features while preserving scale-invariant features that generate the largest wavelet coefficients. When applying this filter to ophthalmic OCT images, a signal-to-noise ratio improvement of 0.7 dB is achieved, with an image sharpness decrease of 3% [78]. Additionally, a multidimensional wavelet technique utilizes correlations in time-series data to suppress speckle noise via decorrelation [79]. A comparable method, based on the curvelets transform, has also been demonstrated [80,81]. An alternative method for speckle suppression concurrently limits the magnitude to align with a blurred rendition of the image. Simultaneously, it preserves the details by constraining the image to align with the data in a least-squares manner [82]. The blurred OCT image serves as a "default" reference, guiding the assignment of magnitude where the data leaves the magnitude of the reconstructed image unspecified. The applied constraint is a relative entropy constraint known as the I-divergence between the default image and the reconstructed image [83].

Hardware-based ways to eliminate speckle effects are to incorporate several images into a single image, a technique commonly referred to as compound averaging [76,77]. Speckle appears because most objects exhibit features at length scales smaller than the minimum resolvable area of an OCT instrument. This phenomenon results from the interference among randomly positioned scatterers, each individually beyond the resolution capability of the OCT instrument due to its finite bandwidth and focused spot size. In OCT images, speckle manifests as a random modulation in the demodulated amplitude image, arising from the interference among scattered waves from these unresolved scatterers. Unfortunately, in practical scenarios, features generated by the random interference of speckles and those of other points of interest often become indistinguishable. When multiple images of the same static object are acquired and remain unchanged between sequences, they will display identical speckle patterns, even if the noise is independent among the images. Consequently, if these images are averaged, the speckle pattern persists, even with an improved signal-to-noise ratio. To diminish speckles, the averaged images must each exhibit slight variations by probing different coherent superpositions of the sub-resolution scatterers responsible for generating speckles. Achieving this involves implementing a diversity mechanism designed to alter the phase of interference

among the sub-resolution scatterers. Ideally, the diversity mechanism induces independent amplitude modulation due to speckle at each resolvable point in each image. By measuring various combinations of interference among the sub-resolution scatterers, the scatterer density in the image can be more accurately estimated by averaging the randomized amplitudes of the constituent images. So far, there are four main diversity mechanisms used to reduce speckle. One of them is frequency compounding, which merges the images of the identical object captured in some different optical frequency bands. Figure 1.6 shows the experimental setup for speckle reduction in OCT by frequency compounding. Typically, particles scatter at wavelengths within the near-infrared (NIR) range. By introducing two light sources with diverse frequency bands within the NIR and corresponding detectors, it induces a modification in the phase shift of the interference among scatterers, resulting in the generation of two uncorrelated speckle patterns in each band. Due to the largely uncorrelated speckle patterns in both frequency bands, their compounding significantly reduces speckle and increases contrast in the image [84]. Polarization diversity involves assessing the same object using orthogonal polarizations to generate different speckle patterns for each polarization, which can then be averaged [85]. Angular compounding captures the sample with varied tilts of the axial scan relative to the transverse scan direction, deviating from the conventional approach of always having the axially focused beam perpendicular to the transverse scanning direction. Illuminating the scatterers in the object at different angles results in measuring different combinations of scatterers, altering the speckle pattern [86,87]. Spatial compounding de-speckles by averaging different parts of an image are particularly beneficial when object properties are uniform, such as in a sample of human skin [88]. In some techniques, gradually increasing strain is applied to the sample, effectively decorrelating speckle between successive B-scans. Incoherent averaging of these decorrelated images reduces the speckle noise [89,90]. In another method, image registration followed by averaging of multiple B-scans is used to reduce speckle [91].

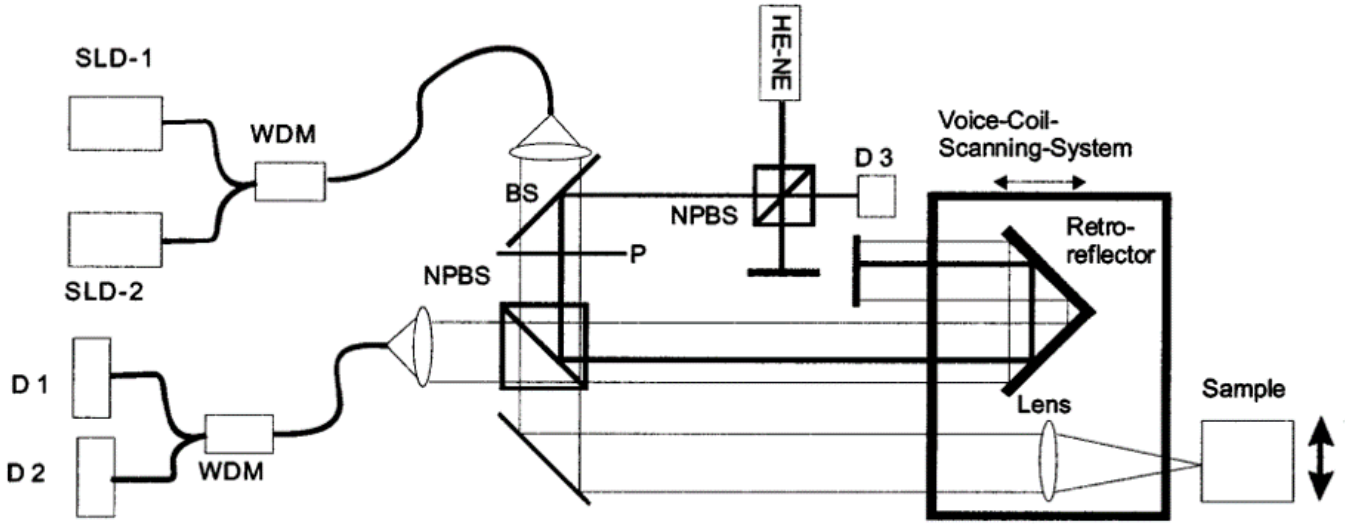

Fig.1.6 Experimental setup for speckle reduction in OCT by frequency compounding. SLD-1 and SLD-2 with center wavelengths of 1312 and 1488 nm, respectively; BS, beamsplitter; P, polarizer; NPBS, nonpolarizing beamsplitter; HE-NE, helium-neon laser; D1–D2, detectors; WDM, wavelength division multiplexer [84].

1.3 Purpose and organization of this thesis

Based on the above backgrounds, the objective of this study is to enhance the performance and expand the capabilities of OCT by introducing a novel light source – a 1.7 μm supercontinuum (SC) source, aiming to further improve its applicability and versatility. To achieve this goal, the study is divided into three phases in detail.

First, one important part of the research work was the development and characterization of 1.7 μm quasi-SC sources, which are based on wavelength-tunable ultrashort pulse generation and fast intensity modulation. The spectral tunability of quasi-SC output in terms of spectral shape, bandwidth, and central wavelength was investigated by adjustable intensity modulation. Then, the noise property was evaluated with the comparison of conventional SC.

The second part of the research work focused on the investigation of high-resolution deep tissue OCT imaging using a broadband quasi-SC. The characteristics of OCT imaging, including sensitivity, lateral resolution, axial resolution, and imaging depth, were examined for the demonstration of possibility of quasi-SC as a source of OCT. Then, comparative imaging between quasi-SC and conventional SC for the biological tissue were performed to validate the feasibility of quasi-SC.

In the final stage, the speckle reduction and image contrast enhancement were investigated by using multiple quasi-SC outputs in OCT imaging. The uncorrelated speckle pattern was obtained by utilizing the wavelength tunability of quasi-SC, and the speckle reduction was achieved through compounding average.

The contents of the chapters making up this thesis are listed below with brief summaries:

In Chapter 2, the theory of optical coherence tomography is explained. The basic characteristics of OCT are presented including lateral and axial resolutions, imaging range of confocal grating, and sensitivity. To realize ultrahigh axial resolution, the dependence of the coherence length on chromatic and polarization dispersion and the bandwidth of the system components are explained. To realize a high-sensitivity system, the causes of noise, such as laser intensity noise and detector sensitivity are explained. Finally, for image contrast improvement, speckle origins in OCT are explained.

In Chapter 3, supercontinuum (SC) and quasi-supercontinuum (SC) sources for high-resolution OCT are explained. For SC and quasi-SC generation, ultrashort pulses and the nonlinear properties of optical fibers are used. Therefore, the theory of pulse propagation in fibers and the principle of Raman soliton generation are explained. The characteristics of optical loss, chromatic dispersion, and nonlinear effects induced in optical fibers are also mentioned.

In Chapter 4, the development of a 1.7 μm quasi-supercontinuum (SC) source using an ultrashort pulse fiber laser and a PM fiber is described. First, an ultrashort pulse generation is demonstrated. In order to obtain 1.7 μm spectral band, an all-fiber amplifier and PM fiber are used for wavelength-tunable Raman soliton generation. To realize tunable quasi-SC, a functional intensity modulation is demonstrated. Variable spectral quasi-SCs are shown by the adjustment of the modulation function.

In Chapter 5, high-resolution deep tissue imaging using 1.7 μm broadband Gaussian-shaped quasi-SC is described. For high-resolution deep tissue imaging, a broadband Gaussian-like quasi-SC is generated with similar spectra to SC. A quantitative comparison of OCT imaging properties, such as imaging sensitivity, axial resolution, lateral resolution, and imaging depth using quasi-SC and conventional SC is presented. Finally, comparative imaging for tissue samples is demonstrated.

In Chapter 6, speckle-reduced imaging using multiple quasi-SCs is demonstrated. For speckle decorrelation,

seven quasi-SCs are obtained by the adjustable intensity modulation. In tape stack imaging, the decorrelation results were demonstrated by the index of correlation coefficient, and the fine-scale layer structure of tape stack are presented. In pig thyroid gland imaging, penetration depth, the image index of SNR, contrast, and CNR are examined in compound averaged images.

Finally, Chapter 7 summarizes the contents of this thesis and presents the outlook.

Reference for Chapter 1

[1] P. Morris, Biomedical Imaging: Applications and Advances (Elsevier, 2014).

[2] R. Liang, ed., Biomedical Optical Imaging Technologies: Design and Applications, Biological and Medical Physics, Biomedical Engineering (Springer-Verlag, 2013).

[3] L. G. Griffith, and M. A. Swartz, "Capturing complex 3D tissue physiology in vitro," Nat. Rev. Mol. Cell Biol. 7, 211–224 (2006).

[4] K. M. Yamada, and E. Cukierman, "Modeling Tissue Morphogenesis and Cancer in 3D," Cell 130, 601–610 (2007).

[5] R. Edmondson, J. J. Broglie, A. F. Adcock, and L. Yang, "Three-Dimensional Cell Culture Systems and Their Applications in Drug Discovery and Cell-Based Biosensors," Assay Drug Dev Technol. 12(4), 207–218 (2014).

[6] D. Huang, E. A. Swanson, C. P. Lin, J. S. Schuman, W. G. Stinson, W. Chang, M. R. Hee, T. Flotte, K. Gregory, C. A. Puliafito, and J. G. Fujimoto, "Optical Coherence Tomography," *Science* **254**(5035), 1178–1181 (1991).

[7] J. M. Schmitt, "Optical coherence tomography (OCT): A Review," *IEEE J. Sel. Topics Quantum Electron.* **5**(4), 1205–1215 (1999).

[8] W. Drexler and J. G. Fujimoto, "Optical Coherence Tomography: Technology and Applications," 2rd ed. Springer Reference, Chapter 1 (2015).

[9] R. A. Riobb, "Biomedical Imaging: Past, Present and Predictions," *Medical Imaging Technology*, **24**(1),25-37(2006).

[10] E.A. Swanson, J.A. Izatt, M.R. Hee, D. Huang, C.P. Lin, J.S. Schuman, C.A. Puliafito, J.G. Fujimoto, "In vivo retinal imaging by optical coherence tomography," *Opt. Lett.* **18**, 1864–1866 (1993).

[11] M.R. Hee, J.A. Izatt, E.A. Swanson, D. Huang, J.S. Schuman, C.P. Lin, C.A. Puliafito, J.G. Fujimoto, "Optical coherence tomography of the human retina," *Arch. Ophthalmol.* **113**, 325–332 (1995).

[12] C.A. Puliafito, M.R. Hee, C.P. Lin, E. Reichel, J.S. Schuman, J.S. Duker, J.A. Izatt, E.A. Swanson, J.G. Fujimoto, "Imaging of macular diseases with optical coherence tomography," *Ophthalmology* **102**, 217–229 (1995).

[13] J.A. Izatt, M.D. Kulkarni, H.-W. Wang, K. Kobayashi, M.V. Sivak Jr., "Optical coherence tomography and microscopy in gastrointestinal tissues," *IEEE J. Sel. Top. Quantum Electron*. **2**, 1017–1028 (1996).

[14] G.J. Tearney, M.E. Brezinski, J.F. Southern, B.E. Bouma, S.A. Boppart, J.G. Fujimoto, "Optical biopsy in human gastrointestinal tissue using optical coherence tomography," *Am. J. Gastroenterol.* **92**, 1800–1804 (1997).

[15] K. Kobayashi, J.A. Izatt, M.D. Kulkarni, J. Willis, M.V. Sivak Jr., "High-resolution crosssectional imaging of the gastrointestinal tract using optical coherence tomography: preliminary results," *Gastrointest. Endosc.* **47**, 515–523 (1998).

[16] C. Pitris, C. Jesser, S.A. Boppart, D. Stamper, M.E. Brezinski, J.G. Fujimoto, "Feasibility of optical coherence tomography for high-resolution imaging of human gastrointestinal tract malignancies," *J.*

Gastroenterol. **35**, 87–92 (2000).

[17] G.J. Tearney, M.E. Brezinski, J.F. Southern, B.E. Bouma, S.A. Boppart, J.G. Fujimoto, "Optical biopsy in human pancreatobiliary tissue using optical coherence tomography," *Dig. Dis. Sci.* **43**, 1193–1199 (1998).

[18] C. Pitris, A. Goodman, S.A. Boppart, J.J. Libus, J.G. Fujimoto, M.E. Brezinski, "High-resolution imaging of gynecologic neoplasms using optical coherence tomography," *Obstet. Gynecol.* **93**, 135–139 (1999).

[19] S.A. Boppart, A. Goodman, J. Libus, C. Pitris, C.A. Jesser, M.E. Brezinski, J.G. Fujimoto, "High resolution imaging of endometriosis and ovarian carcinoma with optical coherence tomography: feasibility for laparoscopic-based imaging," *Br. J. Obstet. Gynaecol.* **106**, 1071–1077 (1999).

[20] C. Pitris, M.E. Brezinski, B.E. Bouma, G.J. Tearney, J.F. Southern, J.G. Fujimoto, "High resolution imaging of the upper respiratory tract with optical coherence tomography: a feasibility study," *Am. J. Respir. Crit. Care Med.* **157**(5 Pt 1), 1640–1644 (1998).

[21] G.J. Tearney, M.E. Brezinski, J.F. Southern, B.E. Bouma, S.A. Boppart, J.G. Fujimoto, "Optical biopsy in human urologic tissue using optical coherence tomography," *J. Urol.* **157**, 1915–1919 (1997).

[22] C.A. Jesser, S.A. Boppart, C. Pitris, D.L. Stamper, G.P. Nielsen, M.E. Brezinski, J.G. Fujimoto, "High resolution imaging of transitional cell carcinoma with optical coherence tomography: feasibility for the evaluation of bladder pathology," *Br. J. Radiol.* **72**, 1170–1176 (1999).

[23] W. Drexler and J. G. Fujimoto, "optical coherence tomography: technology and applications," 2rd ed. Springer Reference, Chapter 10 (2015).

[24] G. J. Tearney, B. E. Bouma, and J. G. Fujimoto, "High-speed phase-and group-delay scanning with a grating-based phase control delay line," *Optics Letters*, **22**(23), 1811-1813(1997).

[25] A. M. Rollins, M. D. Kulkarni, S. Yazdanfar, R. Ung-Arunyawee, and J. A. Izatt, "In vivo video rate optical coherence tomography," *Optics Express*, **3**(6), 219-229(1998).

[26] A.F. Fercher, C.K. Hitzenberger, G. Kamp, S.Y. Elzaiat, "Measurement of intraocular distances by backscattering spectral interferometry," *Opt. Commun.* **117**(1–2), 43–48 (1995).

[27] G. Hausler, M.W. Lindner, "Coherence radar and spectral radar – new tools for dermatological diagnosis," *J. Biomed. Opt.* **3**(1), 21–31 (1998).

[28] T. Mitsui, "Dynamic range of optical reflectometry with spectral interferometry," *Jpn. J. Appl. Phys*. **38**(10), 6133–6137 (1999).

[29] R. Leitgeb, C.K. Hitzenberger, A.F. Fercher, "Performance of fourier domain vs. time domain optical coherence tomography," *Opt. Express* **11**(8), 889–894 (2003).

[30] J.F. de Boer, B. Cense, B.H. Park, M.C. Pierce, G.J. Tearney, B.E. Bouma, "Improved signalto-noise ratio in spectral-domain compared with time-domain optical coherence tomography," *Opt. Lett.* **28**(21), 2067–2069 (2003).

[31] M.A. Choma, M.V. Sarunic, C.H. Yang, J.A. Izatt, "Sensitivity advantage of swept source and Fourier domain optical coherence tomography," *Opt. Express* **11**(18), 2183–2189 (2003).

[32] M. Wojtkowski, R. Leitgeb, A. Kowalczyk, T. Bajraszewski, A.F. Fercher, "In vivo human retinal

imaging by Fourier domain optical coherence tomography," *J. Biomed. Opt*. **7**(3), 457–463 (2002).

[33] N. Nassif, B. Cense, B.H. Park, S.H. Yun, T.C. Chen, B.E. Bouma, G.J. Tearney, J.F. de Boer, "In vivo human retinal imaging by ultrahigh-speed spectral domain optical coherence tomography," *Opt. Lett.* **29**(5), 480–482 (2004).

[34] N.A. Nassif, B. Cense, B.H. Park, M.C. Pierce, S.H. Yun, B.E. Bouma, G.J. Tearney, T.C. Chen, J.F. de Boer, "In vivo high-resolution video-rate spectral-domain optical coherence tomography of the human retina and optic nerve," *Opt. Express* **12**(3), 367–376 (2004).

[35] B. Cense, N. Nassif, T.C. Chen, M.C. Pierce, S.H. Yun, B.H. Park, B.E. Bouma, G.J. Tearney, J.F. de Boer, "Ultrahigh-resolution high-speed retinal imaging using spectral-domain optical coherence tomography," *Opt. Express* **12**(11), 2435–2447 (2004).

[36] M. Wojtkowski, V.J. Srinivasan, T.H. Ko, J.G. Fujimoto, A. Kowalczyk, J.S. Duker, "Ultrahigh-resolution, high-speed, Fourier domain optical coherence tomography and methods for dispersion compensation," *Opt. Express* **12**(11), 2404–2422 (2004).

[37] R.A. Leitgeb, L. Schmetterer, W. Drexler, A.F. Fercher, R.J. Zawadzki, T. Bajraszewski, "Real-time assessment of retinal blood flow with ultrafast acquisition by color Doppler Fourier domain optical coherence tomography," *Opt. Express* **11**(23), 3116–3121 (2003).

[38] B.R. White, M.C. Pierce, N. Nassif, B. Cense, B.H. Park, G.J. Tearney, B.E. Bouma, T.C. Chen, J.F. de Boer, "In vivo dynamic human retinal blood flow imaging using ultra-high-speed spectral domain optical Doppler tomography," *Opt. Express* **11**(25), 3490–3497 (2003).

[39] B. Cense, N. A. Nassif, T. C. Chen, M. C. Pierce, S. H. Yun, B. H. Park, and J. F. de Boer, "Ultrahigh-resolution high-speed retinal imaging using spectral-domain optical coherence tomography," *Optics Express*, **12**(11), 2435-2447 (2004).

[40] W. Drexler and J. G. Fujimoto, "Optical Coherence Tomography: Technology and Applications," 2rd ed. Springer Reference, Chapter 19 (2015).

[41] W. Drexler and J. G. Fujimoto, "Optical Coherence Tomography: Technology and Applications," 2rd ed. Springer Reference, Chapter 17 (2015).

[42] R. R. Alfano, S. L. Shapiro, "Emission in the region 4000 to 7000 Å via four-photon coupling in glass," *Physical Review Letters*, **24**(11), 584 (1970).

[43] I. Hartl, X. D. Li, C. Chudoba, R. K. Ghanta, T. H. Ko, J. G. Fujimoto, R. S. Windeler, "Ultrahigh-resolution optical coherence tomography using continuum generation in an air–silica microstructure optical fiber," *Optics letters*, **26**(9), 608-610 (2001).

[44] K. Isobe, W. Watanabe, S. Matsunaga, T. Higashi, K. Fukui, K. Itoh, "Multi-spectral two-photon excited fluorescence microscopy using supercontinuum light source," *Japanese Journal of Applied Physics*, **44**(1L), L167(2005).

[45] T. Udem, R. Holzwarth, T. W. Hänsch, "Optical frequency metrology," *Nature*, **416**(6877), 233-237(2002).

[46] H. Takara, T. Ohara, K. Mori, K. Sato, E. Yamada, Y. Inoue, K. I. Sato, "More than 1000 channel optical frequency chain generation from single supercontinuum source with 12.5 GHz channel spacing," *Electronics Letters*, **36**(25), 1(2000).

[47] J. K. Ranka, R. S. Windeler, A. J. Stentz, “isible continuum generation in air–silica microstructure optical fibers with anomalous dispersion at 800 nm,” *Optics Letters*, **25**(1), 25-27(2000).

[48] T. A. Birks, W. J. Wadsworth, P. S. J. Russell, “Supercontinuum generation in tapered fibers,” *Optics Letters*, *25*(19), 1415-1417(2000).

[49] N. Nishizawa and T. Goto “Widely Broadened Super Continuum Generation Using HighlyNonlinear Dispersion Shifed Fibers and Femtosecond Fiber Laser,” *Jpn. J. Apply. Phys*. **40**, L36 (2001).

[50] T. Hori, N. Nishizawa, and T. Goto,"Experimental and numerical analysis of widely broadened supercontinuum generation in highly nonlinear dispersion-shifted fiber with a femtosecond pulse," *J. Opt. Soc. Am. B* **21**, 1969-1980 (2004).

[51] T. Hori, J. Takayanagi, N. Nishizawa, and T. Goto, "Flatly broadened, wideband and low noise supercontinuum generation in highly nonlinear hybrid fiber," *Opt. Express* **12**(2), 317-324 (2004).

[52] N. Nishizawa, and J. Takayanagi, "Octave spanning high-quality supercontinuum generation in all-fiber system," *J. Opt. Soc. Am. B* **24**(8), 1786-1792 (2007).

[53] R. Weissleder, “A clearer vision for in vivo imaging,” *Nat. Biotechnol.* **19**, 316–317 (2001).

[54] V. J. Pansare, S. Hejazi, W. J. Faenza, and R. K. Prudhomme, “Review of Long Wavelength Optical and NIR Imaging Materials: Contrast Agents, Fluorophores, and Multifunctional Nano Carriers,” *Chem. Mater.* **24**, 812–827 (2012).

[55] T. Jin, “Non-Invasice Near-Infrared Fluorescence Imaging in the Second Optical Window,” *JJSLSM* **36**(2), 195–200 (2015).

[56] K. K. Tsia, “Essential Basics of Light-Matter Interaction in Biophotonics,” Chap. 2 in Understanding Biophotonics, Fundamentals, Advances, and Applications, L. L. Tsia, Ed., 57–198, Pan Stanford (2015).

[57] R. R. Anderson and J. A. Parrish, “The Optics of Human Skin,” *J. Invest. Dermatol.* **77**, 13–19 (1981).

[58] Johnsen and E. A. Widder, “The Physical Basis of Transparency in Biological Tissue: Ultrastructure and the Minimization of Light Scattering,” *J. Theor. Biol.* **199**, 181–198 (1999).

[59] A. N. Yaroslavsky, P. C. Schulze, I. V. Yaroslavsky, R. Schober, F. Ulrich and H. J. Schwarzmaier, “Optical properties of selected native and coagulated human brain tissues in vitro in the visible and near infrared spectral range,” *Phys. Med. Biol.* **47**, 2059–2073 (2002).

[60] R. H. Wilson, K. P. Nadeau, F. B. Jaworski, B. J. Tromberg, and A. J. Durkin, “Review of short-wave infrared spectroscopy and imaging methods for biological tissue characterization,” *J. Biomed. Opt.* **20**(3), 030901 (2015).

[61] P. Theer, M. T. Hasan, and W. Denk, “Two-photon imaging to a depth of 1000 mm in living brains by use of a Ti:Al2O3 regenerative amplifier,” *Opt. Lett.* **28**(12), 1022–1024 (2003).

[62] D. Kobat1, M. E. Durst, N. Nishimura, A. W. Wong, C. B. Schaffer, and C. Xu, “Deep tissue multiphoton microscopy using longer wavelength excitation,” *Opt. Express* **17**(16), 13354–13364 (2009).

[63] D. Kobat, N. G. Horton, and C. Xu, “In vivo two-photon microscopy to 1.6-mm depth in mouse cortex,” *J. Biomed. Opt.* **16**(10), 106014 (2011).

[64] R. Kawakami, K. Sawada, A. Sato, T. Hibi, Y. Kozawa, S. Sato, H. Yokoyama, and T. Nemoto, “Visualizing hippocampal neurons with in vivo two-photon microscopy using a 1030 nm picosecond pulse

laser," *Sci. Rep.* **3**, 1014 (2013).

[65] J. M. Schmitt, A. Knüttel, M. Yadlowsky, and M. A. Eckhaus, "Optical-coherence tomography of a dense tissue: statistics of attenuation and backscattering," *Phys. Med. Biol.* **39**(10), 1705–1720 (1994).

[66] M. A. Choma, K. Hsu, and J. A. Izatt, "Swept source optical coherence tomography using an all-fiber 1300-nm ring laser source," *J. Biomed. Opt.* ***10***(4), 044009 (2005).

[67] L. A. Sordillo, Y. Pu, S. Pratavieira, Y. Budansky, and R. R. Alfano, "Deep optical imaging of tissue using the second and third near-infrared spectral windows," *J. Biomed. Opt.* **19**(5), 056004 (2014).

[68] L. A. Sordillo, L. Lindwasser, Y. Budansky, P. Leproux, R. R. Alfano, "Near-infrared supercontinuum laser beam source in the second and third near-infrared optical windows used to image more deeply through thick tissue as compared with images from a lamp source," *J. Biomed. Opt.* **20**(3), 030501 (2015).

[69] L. Shi, L. A. Sordillo, A. R. Contreras, and R. Alfano, "Transmission in near-infrared optical windows for deep brain imaging," *J. Biophotonics* **9**(1–2), 38–43 (2016).

[70] H. Kawagoe, M. Yamanaka, S. Makita, Y. Yasuno, and N. Nishizawa, "Full-range ultrahigh-resolution spectral-domain optical coherence tomography in 1.7 μm wavelength region for deep-penetration and high-resolution imaging of turbid tissues," *Appl. Phys. Express* **9**(12), 127002 (2016).

[71] N. Nishizawa, and T. Goto, "Compact system of wavelength-tunable femtosecond soliton pulse generation using optical fibers," *IEEE Photon. Technol.* **11**(3), 325-327 (1999).

[72] K. Sumimura, T. Ohta, and N. Nishizawa, "Quasi-super-continuum generation using ultrahigh-speed wavelength-tunable soliton pulses," *Opt. Lett.* **33**(24), 2892-2894 (2008).

[73] S. K. Devalla, G. Subramanian, T. H. Pham, X. Wang, S., Perera, T. A. Tun, M. J. Girard, "A deep learning approach to denoise optical coherence tomography images of the optic nerve head," *Scientific Reports*, ***9***(1), 14454(2019).

[74] W. Drexler and J. G. Fujimoto, "Optical Coherence Tomography: Technology and Applications," 2rd ed. Springer Reference, Chapter 13 (2015).

[75] J. Goodman, Statistical Optics (Wiley, New York, 1985).

[76] J.M. Schmitt, S.H. Xiang, K.M. Yung, "Speckle in optical coherence tomography," *J. Biomed. Opt.* **4**, 95–105 (1999).

[77] M. Bashkansky, J. Reintjes, "Statistics and reduction of speckle in optical coherence tomography," *Opt. Lett.* **25**, 545–547 (2000).

[78] D.C. Adler, T.H. Ko, J.G. Fujimoto, "Speckle reduction in optical coherence tomography images by use of a spatially adaptive wavelet filter," *Opt. Lett.* **29**, 2878–2880 (2004).

[79] T.S. Ralston, I. Atkinson, F. Kamalabadi, S.A. Boppart, "Multi-dimensional denoising of realtime OCT imaging data," in Proceedings of the IEEE, ICASSSP International Conference on Acoustic, Speech and Signal Processing EEE, Piscataway, pp. II-1148–II-1151 (2006).

[80] Z. Jian, Z. Yu, L. Yu, B. Rao, Z. Chen, B.J. Tromberg, "Speckle attenuation in optical coherence tomography by curvelet shrinkage," *Opt. Lett.* **34**, 1516–1518 (2009).

[81] Z. Jian, L. Yu, B. Rao, B.J. Tromberg, Z. Chen, "Three-dimensional speckle suppression in optical coherence tomography based on the curvelet transform," *Opt. Express* **18**, 1024–1032 (2010).

[82] D.L. Marks, T.S. Ralston, S.A. Boppart, “Speckle reduction by I-divergence regularization in optical coherence tomography,” *J. Opt. Soc. Am. A* **22**, 2366–2371 (2005).

[83] I. Csiszar, “Why least squares and maximum entropy? An axiomatic approach to inference for linear inverse problems,” *Ann. Stat.* **19**, 2032–2066 (1991).

[84] M. Pircher, E. Go¨tzinger, R. Leitgeb, A.F. Fercher, C.K. Hitzenberger, “Speckle reduction in optical coherence tomography by frequency compounding,” *J. Biomed. Opt.* **8**, 565–569 (2003).

[85] T. Storen, A. Royset, N.-H. Giskeodegard, H. M. Pedersen, and T. Lindmo, “Comparison of speckle reduction using polarization diversity and frequency compounding in optical coherence tomography,” in Proceedings of the SPIE, Coherence Domain Optical Methods and Optical Coherence Tomography in Biomedicine VIII (Bellingham, 2004), pp. 196–204.

[86] N. Iftimia, B.E. Bouma, G.J. Tearney, “Speckle reduction in optical coherence tomography by “path length encoded” angular compounding,” *J. Biomed. Opt.* **8**, 260–263 (2003).

[87] A.E. Desjardins, B.J. Vakoc, W.Y. Oh, S.M. Motaghiannezam, G.J. Tearney, B.E. Bouma, “Angle-resolved optical coherence tomography with sequential angular selectivity for speckle reduction,” *Opt. Express* **15**, 6200–6209 (2007).

[88] D.P. Popescu, M.D. Hewko, M.G. Sowa, “Speckle noise attenuation in optical coherence tomography by compounding images acquired at different positions of the sample,” *Opt. Commun.* **269**, 247–251 (2007) .

[89] B.F. Kennedy, T.R. Hillman, A. Curatolo, D.D. Sampson, “Speckle reduction in optical coherence tomography by strain compounding,” *Opt. Lett.* **35**, 2445–2447 (2010).

[90] B.F. Kennedy, A. Curatolo, T.R. Hillman, C.M. Saunders, D.D. Sampson, “Speckle reduction in optical coherence tomography images using tissue viscoelasticity,” *J. Biomed. Opt.* **16**, 020506 (2011).

[91] D. Alonso-Caneiro, S.A. Read, M.J. Collins, “Speckle reduction in optical coherence tomography imaging by affine-motion image registration,” *J. Biomed. Opt.* **16**, 116027 (2011).

Chapter 2 Theory of optical coherence tomography

2.1 Introduction

The background and development history of optical coherence tomography (OCT) have been described in Chapter 1. For a better understanding of OCT and factors influencing OCT performance, the theory of OCT and numerical analyses were presented in this chapter. The fundamental theory of interferometer with low-coherence light was explained at first. Then the basic characteristics of interferometer for imaging such as imaging range, lateral resolution, confocal gating, and lateral resolution were described in section 2.2. The fundamental law governing the axial resolution, which depends on the full width at half maximum (FWHM) of the interference signal and its shape, was shown to be inversely proportional to the spectral bandwidth of the used light source. The principles of time-domain (TD) OCT and Fourier-domain (FD) OCT were explained in section 2.3. The principle, axial resolution limitations, and detected sensitivity for spectral-domain (SD) OCT were explained in section 2.4. The speckle, an inherent property in OCT, which degrades the image contrast, was explained in section 2.5.

2.2 Michelson interferometer

2.2.1 Interferometer with coherent light

Figure 2.1 shows the schematic of the Michelson interferometer [1]. Firstly, to simplify the following analysis, a reflecting mirror was used as the sample, and a single wavelength narrow bandwidth laser source is directed onto a Michelson interferometer. The incoming light is divided into two interferometer arms using a beam splitter, identified as the reference and sample arms. Lights from the two arms are recombined through the beam splitter, and captured by the photodetector, which converts the measured power into an electrical current.

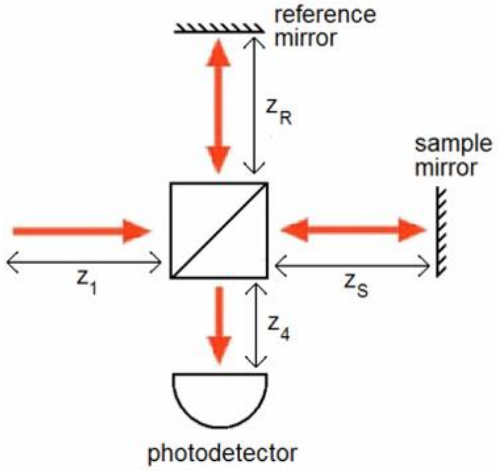

Fig. 2.1 Schematic of the Michelson interferometer [1].

The detected currents from the reference mirror and sample mirror can be expressed in electric filed form, given by

$$\tilde{E}_R = A_R \exp[i(kz_{total,R} + \varphi_0)]$$
$$\tilde{E}_S = A_S \exp[i(kz_{total,S} + \varphi_0)] \tag{2.1}$$

where A is the optical amplitude, z_{total} is the total path length for the light traveling through the interferometer, φ_0 is the initial phase of the electric field of light source before it enters the interferometer, and $k = 2\pi/\lambda$ for the light source of wavelength k. The detected photocurrent is given by

$$\begin{aligned} I_{Dector} &= \left|\tilde{E}_R + \tilde{E}_S\right|^2 \\ &= E_R{}^2 + E_S{}^2 + 2E_R E_S \cos[2k(z_R - z_S)] \\ &= I_R + I_S + 2\sqrt{I_R I_S}\cos[2k(z_R - z_S)] \\ &= I_{Dector}(k, z_R - z_S) \end{aligned} \tag{2.2}$$

where $I_R = E_R{}^2$ and $I_S = E_S{}^2$.The measured signal only depends on relative optical path differences between the two arms of the interferometer.

For the broadband light source, each wavelength component should be treated as a separate source that does not interfere with any wavelength other than its own. Define $I_R = R_R I_0 S(k)$ and $I_S = R_S I_0 S(k)$, where $S(k)$ is normalized spectral function of the light source, and P is the percentage of original light intensity I_0 reaching the detector for light traveling through the arm. Assuming a uniform efficiency of the detector across the spectra of the light source, the detector measures the sum of all contributions from the light source for all wavelengths k, represented by

$$\begin{aligned} I(z_R - z_S) &= \int_k I_{Dector}(k, z_R - z_S)dk \\ &= \int_k [(P_S I_0 + P_R I_0)S(k) + 2\sqrt{P_S P_R} I_0 S(k)\cos(2k(z_R - z_S))]dk \\ &= (P_S + P_R)I_0 + 2\sqrt{P_S P_R}\int_k S(k)\cos(2k(z_R - z_S))dk \end{aligned} \tag{2.3}$$

The function $\int_k S(k)\cos(2k(z_R - z_S))dk$ is an autocorrelation of the light source spectra that is defined as the Weiner-Khinchin theorem (Fourier transform of the magnitude of the electric field). The coherence function, which will be defined as $f_C(z)$ and is centered around $z = z_R - z_S$ is a function that determines the impact on the interference signal when reflections from the two arms of the interferometer have unequal path lengths.

Figure 2.2 shows the measured light intensity at output of the Michelson interferometer as a function of the difference of the optical path lengths between the two interferometer arms for both single-wavelength and broad-bandwidth light cases. The full-width half maximum (FWHM) of the maximum interference fringe is identified as the coherence length. The coherence length l_C is an important quantitative parameter that characterizes the system's capability to separate different interference reflections from each other.

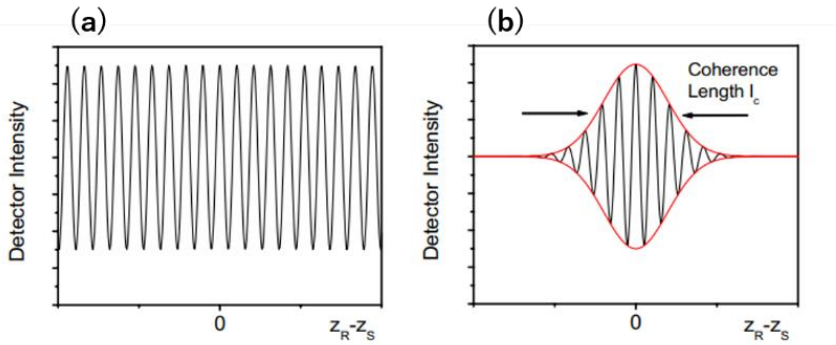

Fig. 2.2 Measured light intensity as a function of the path length difference for (a) single wavelength light and (b) broad bandwidth light [1].

Next, let's contemplate a scenario where a layered structure replaces the single reflector in the sample arm. In this case, the measured interference signal results from the convolution of the coherence function with the reflectivity profile of the sample. Figure 2.3 shows the ideal reflectivity profile and theoretical interference signal. The interference fringe signal emerges as the convolution of the reflection profile with the coherence function.

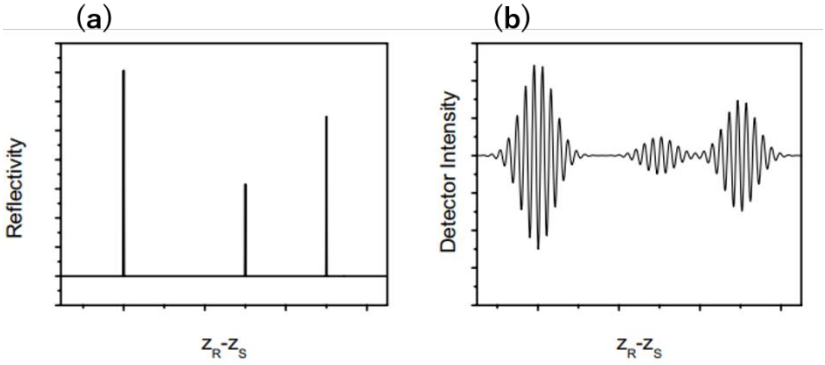

Fig. 2.3 (a) Ideal reflectivity profile and (b) theoretical interference signal [1].

2.2.2 Axial resolution

For detailed description of axial resolution, a sample comprising multiple layers is analyzed [1]. Figure 2.4 shows the exemplary model for the sample with a series of discrete reflectors. The sample is characterized by its depth-dependent electric field reflectivity profile along the sample beam axis $r_s(z_s)$, where z_s is the path length variable in the sample arm measured from the beam splitter. In general, $r_s(z_s)$ is continuous, arising from the continuously changing refractive index of biological tissues and other samples. It may also be complex, encoding both the phase and amplitude of each reflection. However, for an illustrative example, we assume a series of N discrete, real delta-function reflections of the form $r_S(z_S) = \sum_{n=1}^{N} r_{Sn}\delta(z_S - z_{Sn})$, with each reflection characterized by its electric field reflectivity r_{S1}, r_{S2} ... and path length from the beam splitter of z_{S1}, z_{S2}…. The power reflectivity of each reflector is given by the magnitude squared of the electric field

reflectivity, for example, $R_{S1} = |r_{S1}|^2$. The objective of low-coherence interferometry in OCT is to reconstruct the function $\sqrt{R_S z_S}$ from noninvasive interferometric measurements. The electric field passing through the beam splitter after returning from the sample arm is $E_S = \frac{E_i}{\sqrt{2}}[r_S(z_S) \otimes e^{i2kz_S}]$, where $\oplus$ represents convolution and the factor of 2 in the exponential kernel accounts for the round-trip path length to each sample reflection. Note that for most samples, such as biological tissues imaged with OCT, sample reflectivities R_{S1}, R_{S2} ... are typically very small (on the order of ~10^4 to 10^5). The returned reference field typically dominates the reflected sample field. Indeed, the selection of the appropriate reference reflectivity is an important criterion in OCT system design.

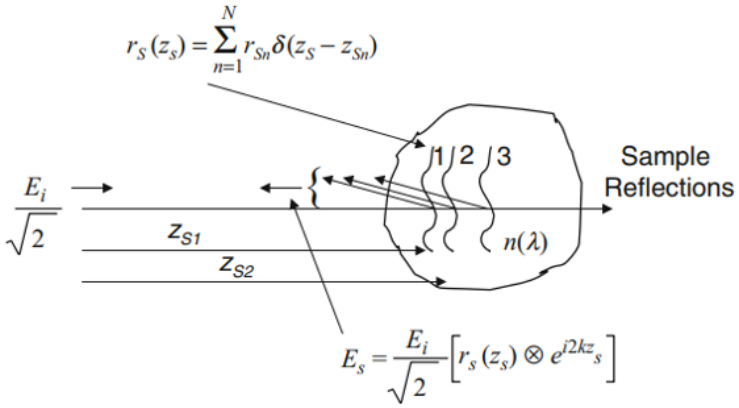

Fig. 2.4 Exemplary model for a sample comprising a series of discrete reflectors [1].

For the example of discrete reflectors, the fields incident on the beam splitter after returning from the reference and sample arms are given by $E_R = \frac{E_i}{\sqrt{2}} r_R e^{i2kz_R}$ and $E_{Sn} = \frac{E_i}{\sqrt{2}} r_{Sn} e^{i2kz_{Sn}}$, respectively. The returning fields have their power halved upon passing through the beam splitter again and interfere at the square-law detector. The detector generates a photocurrent proportional to the square of the sum of the fields incident upon it, expressed as $I_{Dector}(k,\omega) = \frac{\rho}{2}\left\langle |E_R + E_S|^2 \right\rangle = \frac{\rho}{2}\left\langle (E_R + E_S)(E_R + E_S)^* \right\rangle$. Here, ρ is the responsivity of the detector (units amperes/watt), the factor of 2 reflects the second pass of each field through the beam splitter, and the angular brackets denote integration over the response time of the detector. Arbitrarily setting $z=0$ at the surface of the beam splitter and expanding for the detector current give

$$I(k,\omega) = \frac{\rho}{2}\left\langle \left| \frac{s(k,\omega)}{\sqrt{2}} r_R e^{i(2kz_R - \omega t)} + \frac{s(k,\omega)}{\sqrt{2}} \sum_{n=1}^{N} r_{Sn} e^{i(2kz_{Sn} - \omega t)} \right| \right\rangle \tag{2.4}$$

Expanding the magnitude squared functions in Eq.(2.5) eliminates the terms dependent upon the temporal angular frequency $\omega = 2\pi\nu$, which is reasonable since ν oscillates much faster than the response time of any detector. This leaves the temporally invariant terms:

$$I_{Dector}(k) = \frac{\rho}{4}[S(k)(R_R + R_{S1} + R_{S2} + ...)]$$
$$+\frac{\rho}{4}[S(k)\sum_{n=1}^{N}\sqrt{R_R R_{Sn}}(e^{i2k(z_R - z_{Sn})} + e^{-i2k(z_R - z_{Sn})})] \quad (2.5)$$
$$+\frac{\rho}{4}[S(k)\sum_{n\neq m=1}^{N}\sqrt{R_R R_{Sn}}(e^{i2k(z_R - z_{Sm})} + e^{-i2k(z_R - z_{Sm})})]$$

Here, $S(k) = \left\langle |s(k,\omega)|^2 \right\rangle$ is substituted, which encodes the power spectral dependence of the light source. As an example for illustration, adopting a Gaussian-shaped light source spectrum proves convenient for modeling OCT, as it closely approximates the actual light source shape and possesses beneficial Fourier transform properties. The normalized Gaussian function *S(k)* and its inverse Fourier transform *γ(z)* are given by

$$\gamma(z) = e^{-z^2\Delta k^2} \leftrightarrow S(k) = \frac{1}{\Delta k\sqrt{\pi}} e^{-[\frac{(k-k_0)}{\Delta k}]^2} \quad (2.6)$$

and are illustrated in Fig.2.5. Here, k_0 represents the central wave number of the light source spectrum, and Δk represents its spectral bandwidth, corresponding to the half-width of the spectrum at 1/e of its maximum. As will be illustrated later, the inverse Fourier transform *γ(z)*, called the "coherence function," plays a significant role in determining the axial point spread function (PSF) in OCT imaging systems, especially in systems utilizing a low numerical aperture focusing objective. The PSF is often described by its full width at half the maximum (FWHM) value and defines the round-trip "coherence length" of the light source, denoted as l_c. The free-space coherence length is explicitly dependent on the light source bandwidth and is expressed in both wave number and wavelength terms as

$$l_C = \frac{2\sqrt{\ln(2)}}{\Delta k} = \frac{2\ln(2)}{\pi}\frac{\lambda_0^2}{\Delta\lambda} \quad (2.7)$$

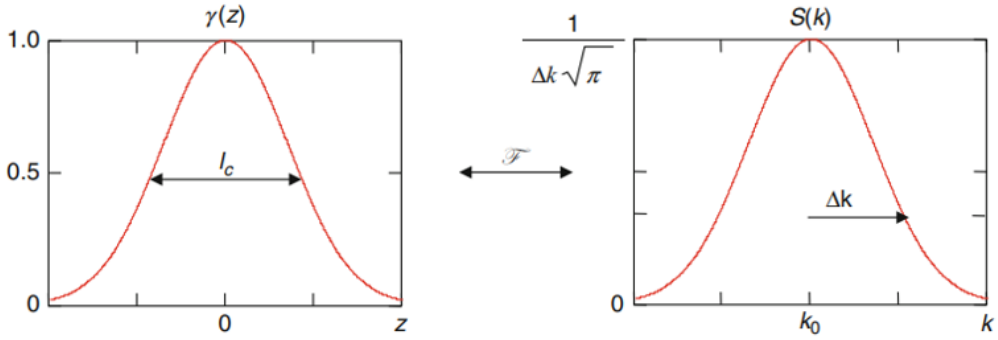

Fig. 2.5 Illustration of Fourier transform relationship between the Gaussian-shaped coherence function *γ(z)* (characterized by the coherence length l_c) and the light source spectrum *S(k)* (characterized by the central wave number k_0 and wave number bandwidth Δk) [1] .

Here, $\lambda_0 = \frac{2\pi}{k_0}$ is the center wavelength of the light source, and $\Delta\lambda$ is its wavelength bandwidth, defined as

the FWHM of its wavelength spectrum (so that $\Delta k = \frac{\pi}{\sqrt{\ln(2)}} \frac{\Delta\lambda}{\lambda_0^2}$). Note the inverse relationship between the coherence length and the light source bandwidth. Recognize the inverse correlation between the coherence length and the light source bandwidth. Simplifying Eq.(2.5) using Euler's rule yields a real result for the detector current as a function of wave number, commonly known as the "spectral interferogram":

$$I_{Dector}(k) = \frac{\rho}{4}[S(k)(R_R + R_{S1} + R_{S2} + ...)] + \frac{\rho}{2}[S(k)\sum_{n=1}^{N}\sqrt{R_R R_{Sn}}\cos[2k(z_R - z_{Sn})]] + \frac{\rho}{2}[S(k)\sum_{n=1}^{N}\sqrt{R_R R_{Sn}}\cos[2k(z_R - z_{Sn})]] \quad (2.8)$$

2.2.3 Confocal grating and lateral resolution

Figure 2.6 illustrates the spot size and focus depth of an assumed Gaussian profile sample arm beam in the region of the beam focus, which help us to analyze the lateral resolution and axial field of view of the OCT system [1,2]. This approach is a reasonable approximation and offers valuable insights into the trade-off between these parameters. Specifically, the spot size is proportional to the numerical aperture (*NA*) of the sample arm focusing optics, while the depth of focus is proportional to NA^2. Confocal microscopes have a slight advantage in lateral resolution compared to conventional bright-field microscopes and the capability to perform "optical sectioning" due to their peaked axial response. Unlike conventional bright-field microscopes, where out-of-focus light is blurred but not attenuated. Figure 2.6 also provides a summary of results characterizing these parameters in lateral and axial directions. The optical system is assumed to be cylindrically symmetric, so only one lateral dimension is displayed.

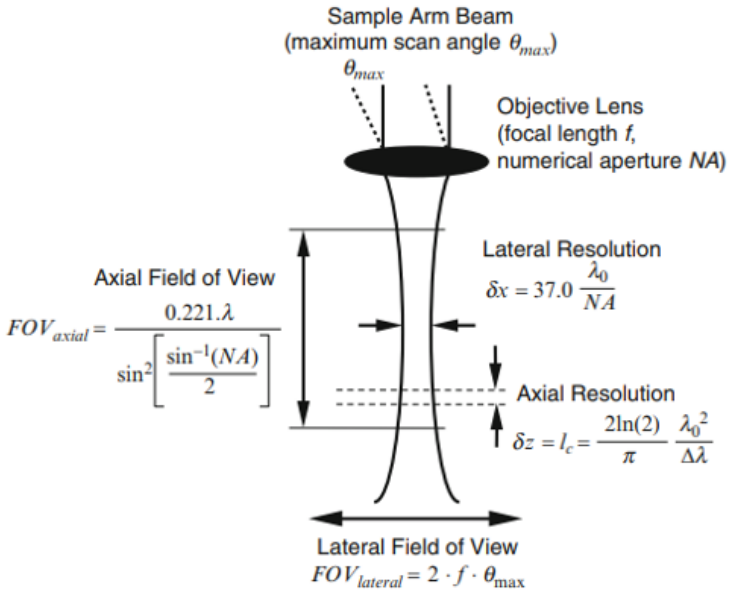

Fig. 2.6 (a) Schematic of generic OCT sample arm optics. Formulas are provided for axial field of view FOV_{axial} and lateral resolution δx (assuming these quantities are dominated by the confocal geometrical optics), axial resolution δz (assuming it is limited by the low-coherence interferometer), and for lateral field of view $FOV_{lateral}$ (assuming a simple f-theta scanning system) [1].

An expression describing the detected intensity from a point reflector positioned in the focal plane of an ideal reflective confocal microscope as a function of lateral position is given by

$$I(v) = \left(\frac{2 \cdot J_1(v)}{v}\right)^4 \tag{2.9}$$

where $J_1(v)$ is a first-order Bessel function of the first kind and v is the normalized lateral range parameter defined by $v = 2\pi \cdot x \cdot \sin(\alpha) / \lambda_0$. Here, x is the lateral distance from the optical axis, α is half the angular optical aperture subtended by the objective, and λ_0 is the center wavelength of the light source. Note that the numerical aperture of the objective is given by $NA = \sin(\alpha)$, assuming that it is properly filled. We interpret Eq. (2.9) as the lateral point spread function of an OCT system at the position of its focal plane and characterize it by defining the lateral resolution δx as its full width at half-maximum (FWHM) power, which is calculated as

$$\delta x = 0.37 \frac{\lambda_0}{\sin(\alpha)} = 0.37 \frac{\lambda_0}{NA} \tag{2.10}$$

The lateral field of view for an OCT system is highly dependent on the specifics of the lateral scanning system used. A relatively straightforward scanning system involves rotating the sample arm beam through the input aperture of the objective lens to a maximum one-sided scan angle θ_{max} in one or two lateral dimensions. In this case, the lateral field of view of the OCT system is simply given by $FOV_{lateral} = 2 f \theta_{\max}$.

We follow the convention in confocal microscopy and describe the axial response of the OCT sample arm optics as the confocal response to a planar rather than point reflector [4,5]. The detected intensity of an ideal confocal microscope from a planar reflector as a function of the reflector position along the optic axis is given by

$$I(u) = \left(\frac{\sin(u/2)}{(u/2)}\right)^2 \tag{2.11}$$

where u is the normalized axial range parameter defined by $u = 8\pi \cdot z \cdot \sin^2(\alpha/2) / \lambda_0$. The axially peaked response of a confocal microscope gives its well-known depth-sectioning capability. This is also the response expected by translating a mirror axially through the focus of an OCT sample arm. In most OCT applications designed for practical clinical and research applications, a relatively low numerical aperture objective is used so that the lateral resolution δx is approximately matched to the axial resolution δz defined by the low-coherence interferometer. Consequently, isotropic resolution imaging is achieved. Under this condition, the confocal gate length is much larger than the lateral resolution since it scales as the square of the numerical aperture. However, the confocal gate length still imposes limitations on the axial range over which the low-coherence interferometric depth scanning may effectively operate. We define the FWHM power of the confocal axial response function as the axial field of view FOV_{axial} of the OCT system, which calculates to

$$FOV_{lateral} = \frac{0.221 \cdot \lambda}{\sin^2[\frac{\sin^{-1}(NA)}{2}]} \tag{2.12}$$

2.3 Time-domain and Fourier-domain optical coherence tomography

Optical coherence tomography (OCT) is the method of imaging that maps the spatial distribution of the interference fringe envelopes based on Michelson interferometer configuration [1-3]. The core of OCT is the identification and measurement of interference fringes. There are two main groups of OCT available depending on the measurement method: time-domain (TD) OCT, Fourier-domain (FD) OCT.

2.3.1 Time-domain (TD) OCT

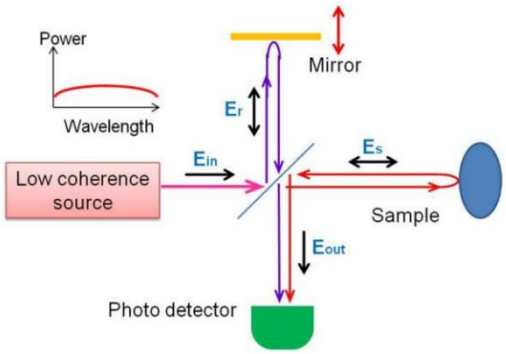

Fig. 2.7 Schematic of TD-OCT.

Figure 2.7 shows the schematic configuration for TD-OCT [1,2]. A wideband light source, namely low-coherent light, is used as the light source. When acquiring interference signals using low-coherent light, strong interference is obtained only when the optical path lengths on the sample side and reference side are approximately equal. Therefore, by moving the reference mirror and obtaining a strong interference signal, it indicates the presence of a reflecting surface at the depth corresponding to that mirror position on the sample. In TD-OCT, the interference light intensity with respect to depth is directly displayed with contrast, creating cross-sectional images. The reason it is called "time-domain" is because the position of the mirror is temporally varied.

In TD-OCT, the wave number-dependent detector current $I_{Detector}(k)$ in Eq. (2.8) is captured by a photo detector, while the reference delay z_r is scanned to reconstruct an approximation of the internal sample reflectivity profile $\sqrt{R_S(z_S)}$. The result is obtained by the integration of Eq. (2.8) over all wavelengths k:

$$\begin{aligned} I_{Detector}(z_R) &= \frac{\rho}{4}[S_0(R_R + R_{S1} + R_{S2} + ...)] \\ &+ \frac{\rho}{2}[S_0 \sum_{n=1}^{N} \sqrt{R_R R_{Sn}} e^{-(z_R - z_{Sn})^2 \Delta k^2} \cos[2k(z_R - z_{Sn})]] \end{aligned} \tag{2.13}$$

Here, $S_0 = \int_0^\infty S(k)dk$ is the spectrally integrated power emitted by the light source. The time-domain "A-

scan" resulting from such a measurement is illustrated in Fig. 2.8. It's worth noting that the sample reflectivity profile convolved with the source coherence function is again recapitulated in the result, along with a DC offset proportional to the sum of the reference and sample power reflectivities. Additionally, the convolved sample reflectivity profile undergoes modulation by a cosinusoidal carrier wave at a frequency determined by the source center wave number k_0 and the free-space difference between the reference and sample arm lengths (z_R- z_{Sn}). As the reference arm length (z_R) is typically varied over time in TD-OCT systems, this carrier wave offers a convenient modulation frequency for lock-in detection, ensuring high-sensitivity detection of the reflectivity envelope and the rejection of the DC offset.

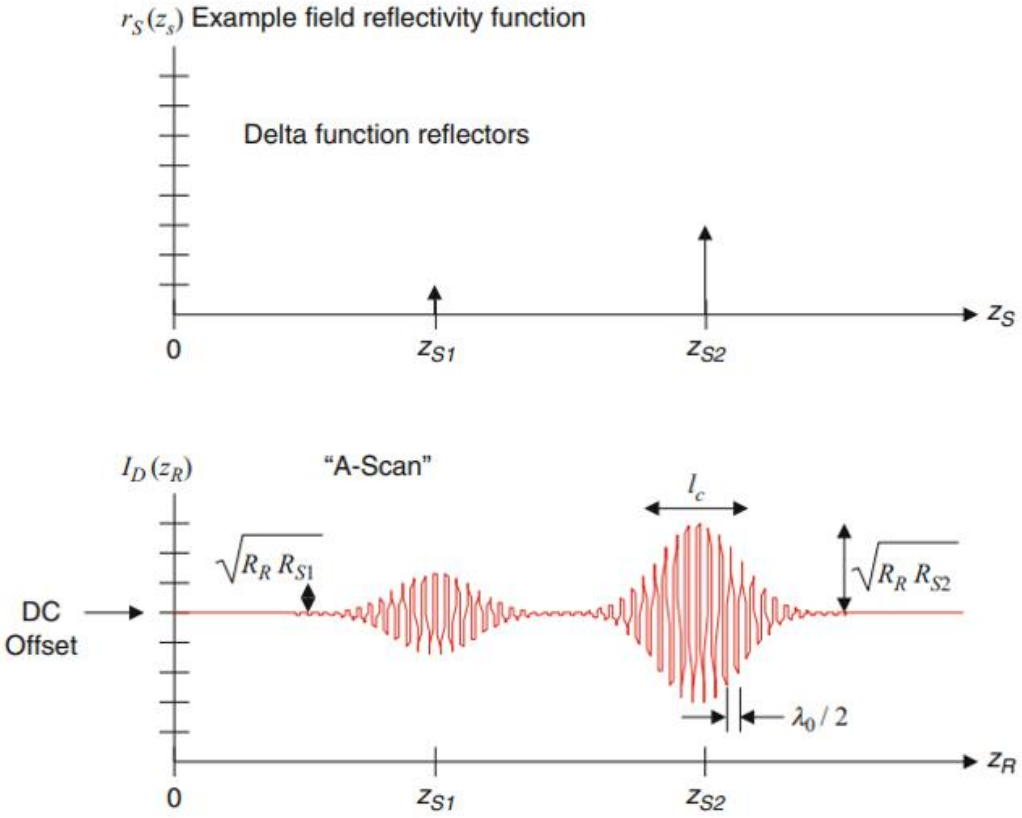

Fig. 2.8 Illustration of the example discrete-reflector sample field reflectivity function and A-scan resulting from time-domain low-coherence interferometry [1].

2.3.2 Fourier-domain (FD) OCT

Frequency-domain (FD) OCT uses the Fourier transform of the interference spectrum to obtain depth information, including spectral-domain OCT (SD-OCT) and swept-source OCT (SS-OCT) [1,2]. Figure 2.9 shows the schematic configuration for SS-OCT. SS-OCT employs a wavelength-swept light source, and the reference arm is fixed. The interference signal is detected as a function of time while rapidly sweeping the wavelength. By performing Fourier transformation, information about the reflective surfaces can be acquired.

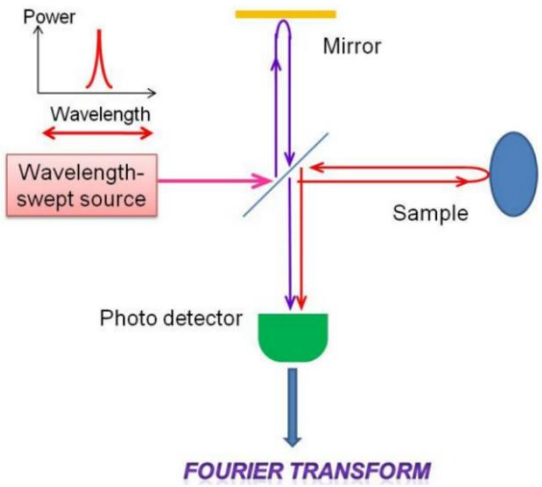

Fig. 2.9 Schematic of SS-OCT.

In FD-OCT, the wave number-dependent detector current $I_{Detector}(k)$ in Eq. (2.8) is captured and processed using Fourier analysis to reconstruct an approximation of the internal sample reflectivity profile $\sqrt{R_S(z_S)}$. The specific method of capturing $I_{Detector}(k)$ depends on the experimental details of the detection apparatus.

The sample reflectivity profile $r_S(z_S)$ is estimated from the inverse Fourier transform of $I_{Detector}(k)$. Making use of the Fourier transform pair $\frac{1}{2}(\delta(z+z_0)+\delta(z-z_0)) \overset{F}{\leftrightarrow} \cos kz_0$ and the convolution property of Fourier transforms $x(z) \otimes y(z) \overset{F}{\leftrightarrow} X(k)Y(k)$, the inverse Fourier transform of Eq. (2.8) may be calculated as

$$
\begin{aligned}
i_D(z) &= \frac{\rho}{8}[\gamma(z)(R_R + R_{S1} + R_{S2} + ...)] \\
&+ \frac{\rho}{4}[\gamma(z) \otimes \sum_{n=1}^{N} \sqrt{R_R R_{Sn}}\,\delta[z \pm 2(z_R - z_{Sn})]] \\
&+ \frac{\rho}{8}[\gamma(z) \otimes \sum_{n \neq m=1}^{N} \sqrt{R_{Sm} R_{Sn}}\,\delta[z \pm 2(z_{Sm} - z_{Sn})]]
\end{aligned}
\tag{2.14}
$$

Note that the desired sample field reflectivity profile $\sqrt{R_S z_S} = \sum_{n=1}^{N} \sqrt{R_{Sn}}\,\delta[z_S - z_{Sn}]$ is indeed embedded within the cross-correlation terms of Eq. (2.14), although it is surrounded by several confounding factors. Carrying out the convolutions by taking advantage of the sifting property of the delta function, we derive the outcome of the interferometric measurement, commonly referred to as the "A-scan":

$$
\begin{aligned}
i_D(z) &= \frac{\rho}{8}[\gamma(z)(R_R + R_{S1} + R_{S2} + ...)] \\
&+ \frac{\rho}{4}\sum_{n=1}^{N}\sqrt{R_R R_{Sn}}[\gamma[2(z_R - z_{Sn})] + \gamma[-2(z_R - z_{Sn})]] \\
&+ \frac{\rho}{8}\sum_{n\neq m=1}^{N}\sqrt{R_{Sm} R_{Sn}}[\gamma[2(z_{Sm} - z_{Sn})] + \gamma[-2(z_{Sm} - z_{Sn})]]
\end{aligned}
\tag{2.15}
$$

The results in Eqs. (2.14) and (2.15) for the example of discrete sample reflectors and a Gaussian-shaped source spectrum are plotted in Fig.2.10. As can be seen in the figure, the sample field reflectivity profile $\sqrt{R_S z_S} = \sum_{n=1}^{N}\sqrt{R_S z_{Sn}}\delta(z_S - z_{Sn})$ is reproduced in the cross-correlation terms, with the following modifications: Firstly, the sample reflectivity profile is presented as a function of the reference coordinate z_R, instead of the sample coordinate z_S. Secondly, each sample reflector's apparent displacement from the reference position is doubled, considering that the interferometer measures the round-trip distance to each reflector. We accommodate this by defining a new single-pass depth variable $\tilde{z} = 2z$. Thirdly, each reflector is broadened or blurred to a width of approximately a coherence length by convolution with the function $\gamma(z)$. This aligns with the definition of a point spread function (PSF) in an imaging system. Given the inverse relationship of the coherence length to the light source bandwidth, enhancing the fidelity of the estimate of $\sqrt{R_S z_S}$ involves using light sources as broad-bandwidth as possible. Finally, the magnitude of the detected sample reflectivity, which can be very small, is amplified by the large homodyne gain factor represented by the strong reference reflectivity $\sqrt{R_R}$.

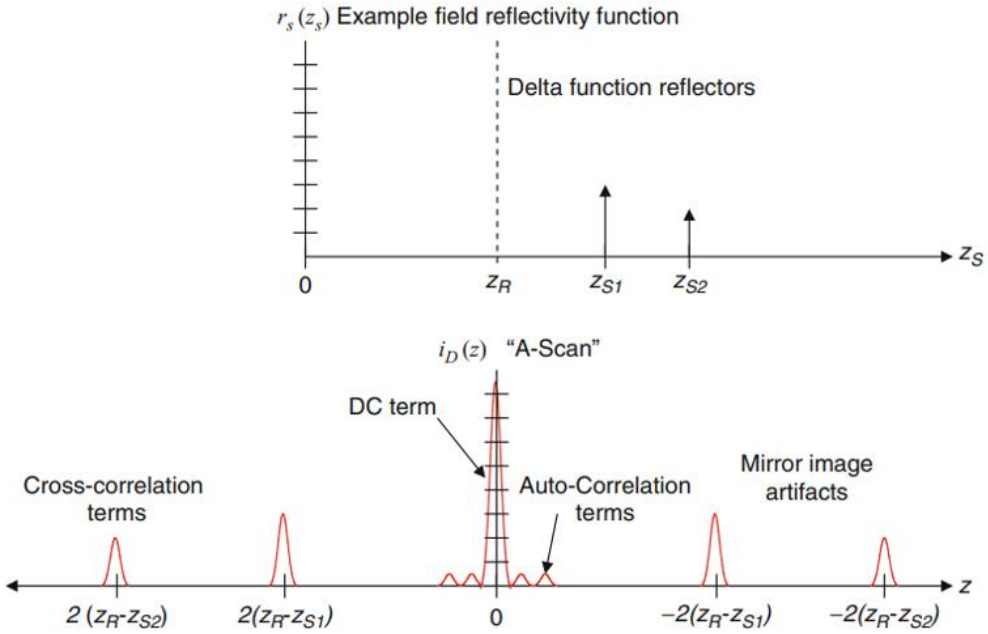

Fig. 2.10 Illustration of the example discrete-reflector sample field reflectivity function and the A-scan resulting from Fourier-domain low-coherence interferometry [1].

2.4 Spectral domain (SD) optical coherence tomography

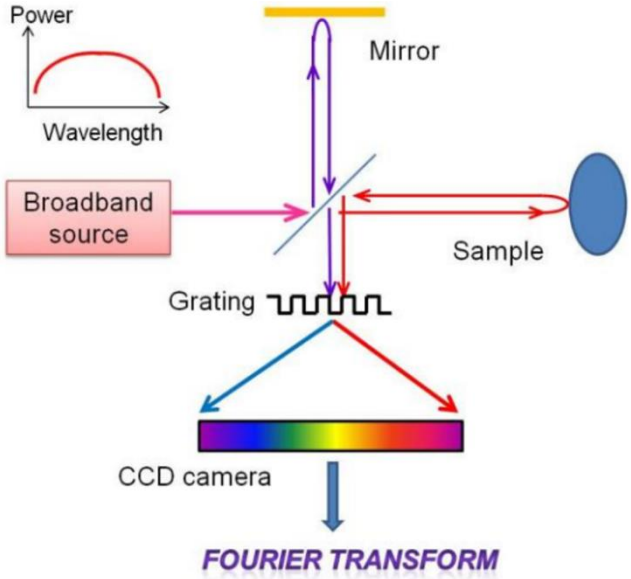

Fig. 2.11 Schematic of SD-OCT.

Figure 2.11 shows the schematic configuration for SD-OCT [1,2]. The light source in SD-OCT utilized broadband light, is similar to the source of TD-OCT. However, instead of moving the reference mirror, the interferograms is captured through a CCD array. In this way, the interfered light can be acquired in the frequency domain. By applying a Fourier transform to the obtained signal, it is possible to obtain reflected tomographic information as TD-OCT. The absence of mirror movement results in a faster imaging process compared to TD-OCT, with superior sensitivity.

2.4.1 Axial resolution limits for OCT

For high axial resolution, the limitations such as spectral shape, chromatic aberration, polarization, optical components, detection system, and mechanical components are described [1].

Light sources for high-resolution and ultrahigh-resolution OCT need not only high spatial coherence, ultrabroad bandwidth emission with enough output power and low noise, but also an optimal spectral shape. The coherence length, defined as the full width at half maximum of the field autocorrelation measured by the OCT interferometer, is influenced by the spectral shape of the light source and the transfer function of the OCT system. The transfer function is primarily determined by the optical properties of the interferometer, as described in detail later. The ideal spectrum for OCT would exhibit a Gaussian spectral shape, yielding a Gaussian coherence function without side lobes. Large spectral modulations would reduce sensitivity and resolution, due to the presence of side lobes in the fringe pattern that appear symmetrically to the coherence-function maximum.

Chromatic aberration of the optics poses another limitation to achieving ultrahigh resolution. Traditional lenses exhibit a wavelength-dependent focal length, causing ultrabroad bandwidth light to focus at different planes. This variation in focal position across wavelengths disrupts the local effective bandwidth,

consequently degrading resolution. Specially corrected achromatic optics counteract this by introducing wavelength-independent attenuation for different imaging distances, preserving spectral shape, optical bandwidth, and axial resolution. Thus, the use of appropriate achromatic objectives is essential to maintain the ultrabroad bandwidth of light for achieving ultrahigh resolution. Reflective objectives, such as catadioptrics with parabolic mirrors, offer an alternative as they are free from chromatic aberration and do not introduce dispersion like transmissive elements. In ophthalmic OCT, the chromatic aberration of the eye itself becomes a limiting factor for axial resolution in ultrahigh-resolution retinal OCT imaging if not properly compensated.

Axial resolution in OCT systems also faces limitations due to polarization mismatch between interferometer arms and polarization dispersion, which introduces a phase difference. These factors contribute to changes in the shape of the coherence function and axial resolution, respectively. Although polarization changes in the static system can be compensated, the loss of a single polarization state and sample birefringence result in improper overlapping of the reference and sample light, leading to severe modulations of the interference spectrum. Therefore, high-resolution OCT demands meticulous polarization control, and the polarization dependence of light sources becomes a crucial parameter.

The axial resolution and sensitivity of an OCT system are significantly influenced by the optical transmittance, coating, and wavelength-dependent losses of various components such as bulk or fiber optics, delivery system optics, and even the human eye in the context of ultrahigh-resolution ophthalmic OCT. To ensure light propagation without interference within and between fibers, it essential to use single-mode and sometimes polarization-maintaining fibers with appropriate cutoff wavelengths. Conventional fiber couplers, designed for a narrow wavelength range, may lead to unequal beam-splitting, reducing resolution when delivering broad bandwidth laser light. Therefore, specialized broad bandwidth and wavelength-flattened fiber or bulk optic beam splitters are necessary for maintaining high axial resolution. Optical circulators are commonly employed in OCT systems to create more power-efficient and sensitive interferometers. Nonreciprocal elements in circulators help reduce power delivery losses from the source to the sample and signal losses from the sample to the detector. However, due to the large optical bandwidths involved (e.g., 200 nm bandwidth at 800 nm), it is essential to use extremely broad-band components to avoid wavelength-dependent losses.

The detection system, encompassing electronics, digitization, and acquisition of the interference signal, plays a crucial role in maintaining axial OCT resolution, depending on the interference signal acquisition method. In time-domain and tunable laser-driven FD-OCT systems, the transimpedance amplifier and electronic bandpass filtering need careful design to accommodate the ultrabroad optical bandwidth. The electronic bandwidth of the bandpass filter must strike a balance, avoiding excessive narrowness that could reduce axial resolution and excessive breadth that might compromise sensitivity through noise introduction. Real-time adaptive filtering can be employed to optimize sensitivity while preserving axial resolution. In TD-OCT, hardware demodulation should be tailored to scanning speed and optical bandwidth to prevent broadening caused by electronic time response, which could lead to a larger coherence length of the envelope compared to the full interference fringe signal. Precise temporal digitization is crucial, requiring at least five to ten times oversampling concerning the central wavelength, Doppler shift, and scanning speed to preserve the achieved axial resolution. For tunable lasers, adjusting the linearity of the scan or utilizing k-trigger can discretely sample the scan in k-space. While most tunable laser technology is limited to standard bandwidths and may not achieve ultrahigh resolution, sophisticated post-processing techniques can compensate for camera technology-related nonlinearities and sampling issues when using broadband light sources in the

frequency domain.

Lastly, the mechanical performance of scanners employed for transverse and/or depth scanning must be meticulously chosen and effectively controlled. Mechanical jitter or displacement between adjacent depth scans, along with noisy control signals of the scanner, can lead to distorted and consequently degraded resolution in high-resolution OCT tomograms.

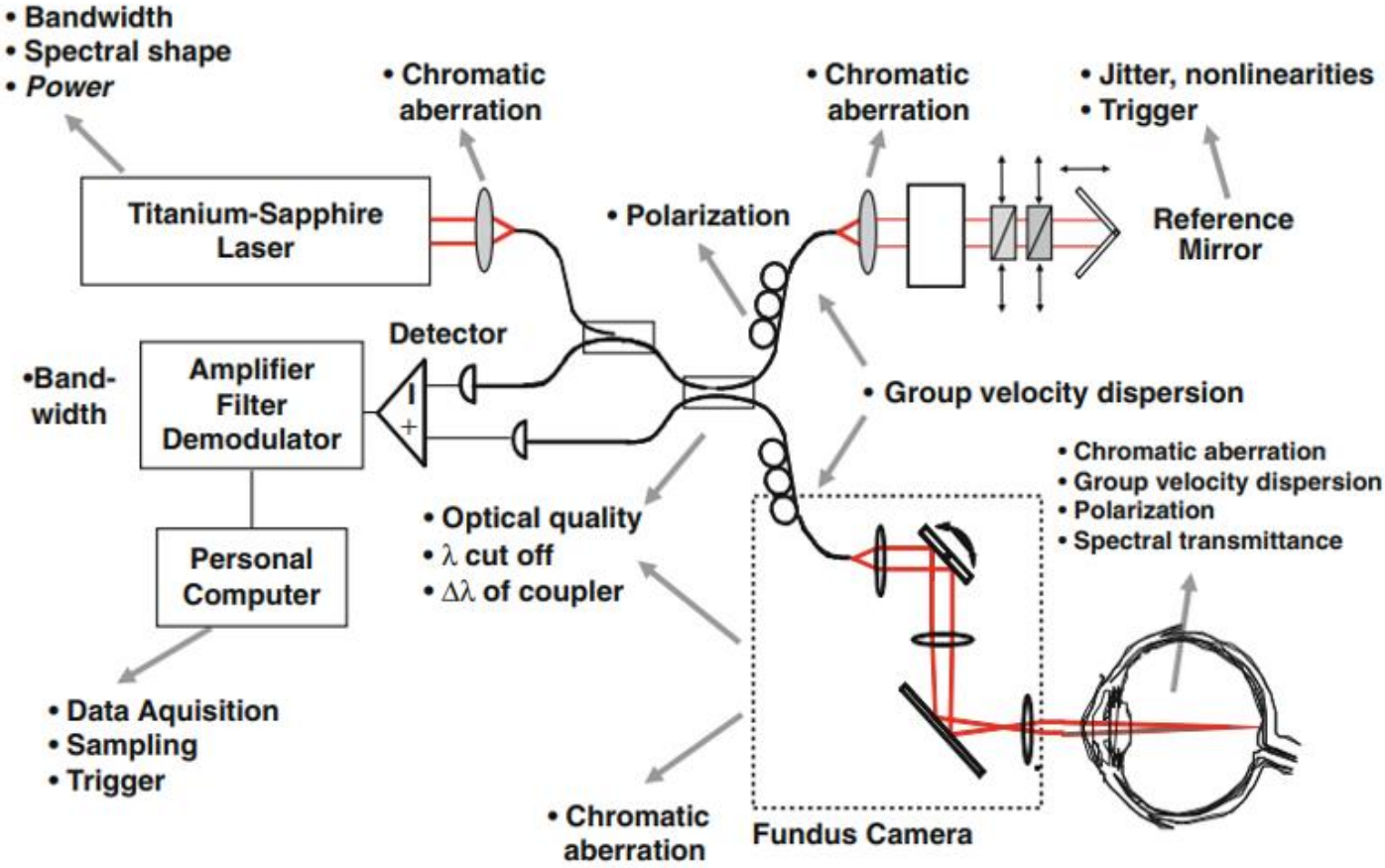

Fig.2.12 Axial resolution limits in ultrahigh-resolution OCT. Summary of all limitations for a time-domain OCT based system for ophthalmic imaging: light source, spectral transmittance of OCT system, delivery system, spectral properties of sample (in this case the human eye), as well as detection and data acquisition specifications [1].

2.4.2 Sensitivity and dynamic range in OCT

The signal-to-noise ratio (SNR) for any system is defined as the signal power divided by the noise process variance. SNR analysis in SD-OCT followed directly from its predecessor technique of optical low-coherence domain reflectometry [1,2]. To simplify the analysis, we focus on a single sample reflector at position z_S and neglect autocorrelation terms. The sampled version of the spectral interferogram in FD-OCT systems is

$$I_d[k] = \frac{\rho}{2} S_{SDOCT}[k_m][R_R + R_S + 2\sqrt{R_R R_S}\cos[2k_m(z_R - z_S)]] \tag{2.16}$$

Here, $S_{SDOCT}[k_m] = \frac{s(k)_{k=k_m}}{2}$ is that portion of the instantaneous power incident on the sample that corresponds to spectral channel *m* of the detection system in SD-OCT. In the discrete case, the inverse Fourier transform operation is implemented as an inverse discrete Fourier transform:

$$i_D[z_m] = \sum_{m=1}^{M} I_D[k_m] e^{ik_m z_m / M} \tag{2.17}$$

For the case of a single sample reflector located at depth $z_R = z_S$, the peak value of the interferometric term is given by

$$i_D[z_m = (z_R = z_S)] = \frac{\rho}{2}\sqrt{R_R R_S}\sum_{m=1}^{M} S_{SDOCT}[k_m] = \frac{\rho}{2}\sqrt{R_R R_S}\, S_{SDOCT}[k_m]\cdot M \tag{2.18}$$

the latter expression being under the assumption that each spectral channel has equal power in it (for a rectangular-shaped source spectrum). For a more realistic Gaussian-shaped source spectrum centered at pixel *M/2* and clipped at its *1/e* ^{2} points, that is, $S_{SDOCT}[k_m] = S_{SDOCT}[k_{M/2}]\exp[-2\cdot(k_m - k_{M/2})^2/(k_{M/2})^2]$, then the last factor is $SNR_{SDOCT} = \frac{\langle i_D \rangle^2_{SDOCT}}{\sigma^2_{SDOCT}} = \frac{\rho S_{SDOCT}[k_m] R_S}{4eB_{SDOCT}}\cdot M \sum_{m=1}^{M} S_{SDOCT}[k_{M/2}] = S_{SDOCT}[k_{M/2}]\cdot M \cdot 0.598$. The cosinusoidal spectral interference pattern in each separate detection channel originating from a single reflector combines coherently, resulting in a peak signal power significantly higher than the signal power in each channel independently. In SD-OCT, each detection channel captures interference over an extended coherence length compared to the single detection channel in TD-OCT, thanks to its limited spectral range. This coherent addition of signal power in SD-OCT is not isolated to the trivial choice of $z_m = (z_R - z_S) = 0$; any other choice of $z_m = (z_R - z_S)$ would give rise to phase factors in the Fourier kernel, which would still coherently sum to an equivalent combined signal peak. The mean-square peak signal power in SD-OCT is thus $\langle i_D \rangle^2_{SDOCT} = \frac{\rho^2 S_{SDOCT}{}^2[k_m]}{4}[R_R R_S]\cdot M^2$.

To finalize the calculation of the SNR of SD-OCT, we need to consider how noise transitions from the k-domain to the z-domain. $I_D[k_m]$ can be can be extended to incorporate an additive, uncorrelated Gaussian white noise term $\alpha[k_m]$. $\alpha[k_m]$ has a mean of zero, a standard deviation $\sigma[k_m]$, and a lower limit set by shot noise. Assuming $R_R >> R_S$, in the shot noise limit, the noise in each spectral channel is uncorrelated; thus, the noise variances add incoherently in the inverse discrete Fourier summation to give $\sigma^2_{SDOCT}[z_m] = \sum_{m=1}^{M}\sigma^2_{SDOCT}[k_m] = e\rho S_{SDOCT}[k_M] R_R B_{SDOCT}\cdot M$. Therefore, the SNR of SD-OCT in general is given by

$$SNR_{SDOCT} = \frac{\langle i_D \rangle^2_{SDOCT}}{\sigma^2_{SDOCT}} = \frac{\rho S_{SDOCT}[k_m] R_S}{4e\rho B_{SDOCT}}\cdot M \tag{2.19}$$

2.5 Speckle origins in OCT

Figure 2.13 is a schematic diagram showing the origin of speckles in OCT. The principle of OCT is based on low-coherence measurements that visualize the tomographic structure from scattered and reflected light-intensity information from a sample, which contains a large number of scatterers [5-7]. When the light illuminates the sample, multiple backward-scattering with random direction occurs due to the presence of scatterers in the sample volume. The light returned from one volume in the sample is the superposition of these random scattered light. The result of the superposition may be large or small, depending on the relative phases of the various components, as shown in Fig.2.14. This phenomenon is well known as“random walk”.

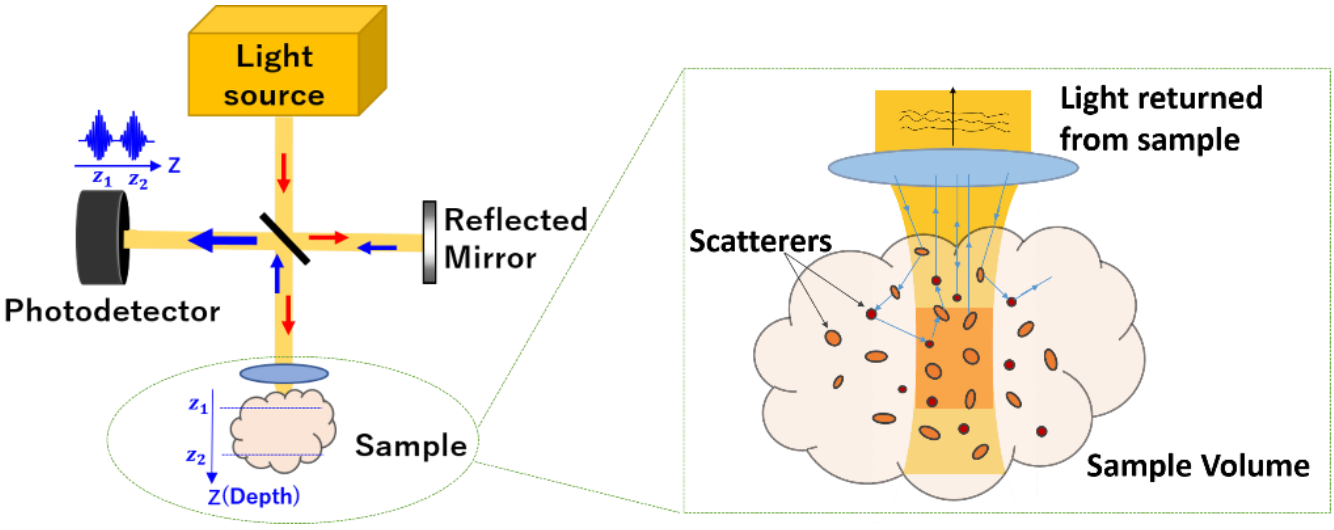

Fig. 2.13 Schematic diagram showing origin of speckle in OCT.

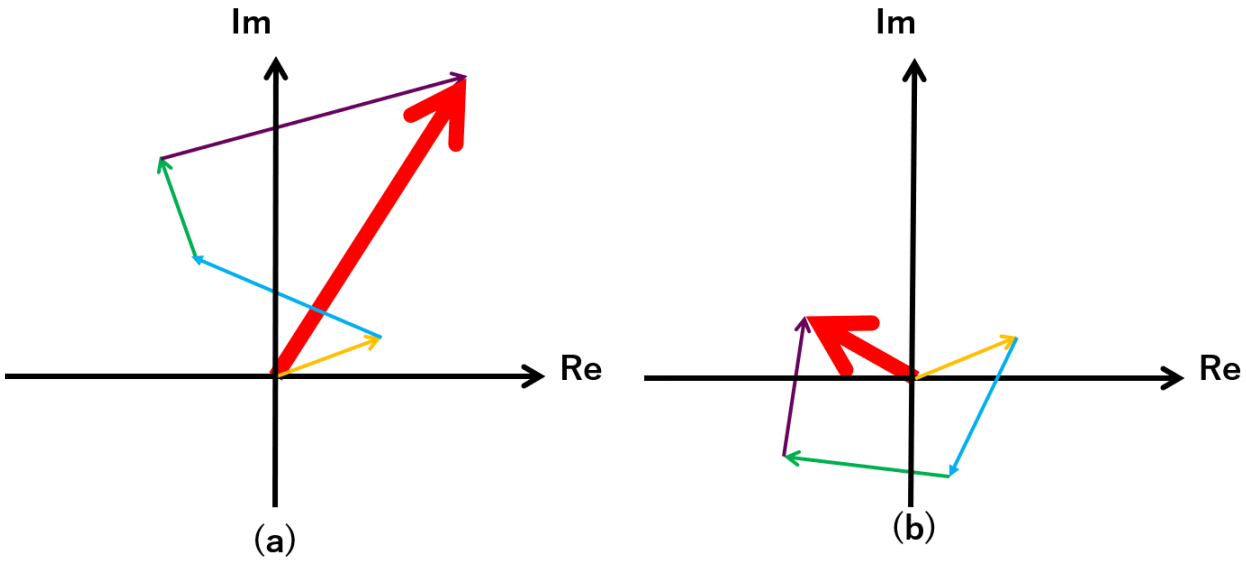

Fig. 2.14 Random walk showing (a)large resultant and (b) small resultant.

The detected currents from sample arm can be expressed from Eq. (2.1), given by

$$\tilde{E}_S = A_S \exp[i(kz_{total,S} + \varphi_0 + \Delta\varphi)] \tag{2.20}$$

where A is the optical amplitude, z_{total} is the light path length for the light has traveled through the interferometer, φ_0 is the phase of electric field of light source before it enters the interferometer, $\Delta\varphi$ is the random phase caused by random walk and $k = 2\pi/\lambda$ for the light source of wavelength k. The detected photocurrent is given by

$$\begin{aligned} I_{Dector} &= \left|\tilde{E}_R + \tilde{E}_S\right|^2 \\ &= I_R + I_S + 2\sqrt{I_R I_S}\cos[2k(z_R - z_S) + \Delta\varphi] \\ &= I_{Dector}(k, z_R - z_S, \Delta\varphi) \end{aligned} \tag{2.21}$$

From Eq. (2.21), we found that the detected photocurrent is sensitive to the random phase, resulting a fluctuation of detected intensity. This is the cause of speckle. From the image, it appears as a collection of bright or dark spots patterns.

The speckle is related to the scatterers' distribution and does not vary with time. For speckle suppression, the hardware-based methods, well known as compound average approaches described in Chapter 1, obtain multiple uncorrelated scatter patterns by using hardware insertion of experimental variables, and then speckle reduction is achieved by compound averaging, such as frequency compounding, which uses different detection wavelengths to capture uncorrelated scattering patterns, and angle compounding, in which the angle of incident light is changed to realize speckle decorrelation.

2.6 Summary

In this chapter, the theory of OCT based on the Michelson interferometer and numerical analyses of OCT signals have been presented. To realize the properties of OCT in terms of high spatial resolution, high sensitivity, high contrast and large penetration depth, there are many corresponding elements such as optical devices, electrical devices, and the system design. In order to obtain high resolution, including axial and lateral resolution, the effects of light source characteristics such as center wavelength, bandwidth, and spectral shape on resolution were discussed. In order to obtain high speed and high sensitivity, different coherent signal detection modes of time-domain OCT and frequency-domain OCT were described, as well as the superiority of SD-OCT in terms of imaging speed and sensitivity. In order to obtain OCT image with high contrast, the origins and ways for speckle reduction, an inherent noise in OCT imaging, were presented.

Reference for Chapter 2

[1] W. Drexler and J. G. Fujimoto, "Optical Coherence Tomography: Technology and Applications," Ed2, Springer Reference, Chapter 2 (2015).

[2] A. F. Fercher, W. Drexler, C. K. Hitzenberger, and T. Lasser, "Optical coherence tomography—principles and applications," *Rep. Prog. Phys.* **66**, 239–303 (2003).

[3] W. Drexler, U. Morgner, R. K. Ghanta, F. X. Kartner, J. S. Schuman, and J. G. Fujimoto, "Ultrahigh-resolution ophthalmic optical coherence tomography," *Nat. Med.* **7**(4), 502–507 (2001).

[4] T. Wilson, "Confocal microscopy," (Academic Press, London, 1990).

[5] J. W. Goodman, Speckle phenomena in optics (W. H. Freeman, 2010).

[6] J. M. Schmitt, S. H. Xiang, and K. M. Yung, "Speckle in optical coherence tomography," *J. Biomed. Opt.* **4**(1), 95-105(1999).

[7] M. Bashkansky, and J. Reintjes, "Statistics and reduction of speckle in optical coherence tomography," *Opt. Lett.* **25**(8), 545-547(2000).

Chapter 3 Supercontinuum and quasi-supercontinuum sources for OCT

3.1 Introduction

As described in Chapter 1 and Chapter 2, the characteristics of light sources influence the OCT performance greatly. Generally, there are five primary considerations for evaluating optical sources for OCT imaging, (1) central wavelength, (2) bandwidth and spectral shape, (3) averaged power, (4) noise, and (5) stability. Considering all these factors, the supercontinuum (SC) source proves to be a valuable light source for high-resolution deep tissue imaging, compared with SLDs and solid-state lasers.

In this chapter, SC and quasi-SC generation for OCT were described. An electrical wavelength-tuning technique of the soliton pulse was also presented. In addition, the optical nonlinear effects in fiber were introduced for understanding of SC and quasi- SC generation.

3.2 Supercontinuum (SC) generation

Nonlinear propagation of laser pulses with moderate energies, measured in a few nJ, within micro-structured fibers, can generate spectra much broader than a single optical octave. Photonic crystal fibers facilitate the development of a new category of light sources that emit light with low time coherence and high space coherence. The unique geometry of these fibers results in an unusually small cross-section of the fundamental mode, enhancing peak power and, consequently, nonlinearity. Simultaneously, engineering the fiber dispersion can prevent rapid temporal spreading. Therefore, photonic crystals present numerous exceptional features, including straightforward dispersion management, single-mode behavior across various wavelengths, and valuable nonlinear properties. They can be easily customized to meet diverse requirements, offering spectra at different wavelengths spanning multiple octaves. Direct access to these spectral widths from a laser oscillator is unattainable since they surpass the fluorescence bandwidth of active ions. To circumvent excessively strong spectral modulation inherent in the spectral broadening process, nonlinear fiber propagation should only induce moderated spectral broadening. This implies that the initial bandwidth of pulses emerging from the oscillator should be as broad as possible. The exploration of photonic crystals in the research field was prompted by the anticipation of a photonic bandgap analogous to electronic bandgaps in semiconductors. Initially, the photonic bandgap was the sole guiding mechanism considered for this innovative class of optical fibers. Presently, devices can be fabricated through micro-structuring and the incorporation of air holes into the fiber, employing the principle of total internal reflection.

The ultrabroad bandwidth spectrum of a supercontinuum plays a pivotal role in achieving high resolution in OCT. A critical factor in the generation of this supercontinuum is the precise confinement of the mode. By confining the mode to a small area, the strength of nonlinear processes responsible for supercontinuum generation is significantly enhanced. In terms of fabrication, mechanically robust micro-structured fibers (MFs) with an exceptionally small core size, even down to 1 μm, can be created. The mechanisms governing supercontinuum generation depend on various parameters of the input pulses [1]:

- Pulse duration
- Peak power
- Center wavelength

And the parameters of the micro-structured fiber (MF):

- Dispersion profile
- Effective modal area
- Birefringence

These mechanisms are included:

- Self-phase modulation (SPM)
- Cross-phase modulation (XPM)
- Four-wave mixing (FWM)
- Stimulated Raman scattering (SRS)

The exploration of fiber broadening in highly nonlinear microstructure fiber, resulting in the generation of an extremely broad bandwidth supercontinuum spanning from the visible to the near-infrared using femtosecond pulses, has been well-documented. This can be attributed, in part, to the waveguide dispersion characteristics of the fibers, which shift the zero-dispersion wavelength towards shorter wavelengths. Additionally, the small core diameters play a role in providing tight mode confinement. The swift advancements in the design and fabrication of various micro-structured fibers over the last few years have further facilitated the generation of broad bandwidth light from nonlinear optical fibers. Consequently, this method has gained considerable interest as an effective approach for achieving high-resolution and ultrahigh-resolution OCT.

3.3 Quasi-supercontinuum (SC) generation

3.3.1 Wavelength-tunable ultrashort pulse generation

The wavelength of the Raman soliton pulse depends on the fiber length and the input laser power. Therefore, by varying them, we can generate the wavelength-tunable soliton pulse. Figure 3.1 shows the observed Raman soliton spectra for different power injections of the laser pulse, when the fiber laser pulse which generates the 100-fs pulse at the wavelength of 1.56 μm, is launched into the diameter-reduced polarization-maintaining (PM) fiber. The nonlinear coefficient of the PM fiber is $\gamma = 4.8\text{W}^{-1}\ \text{km}^{-1}$ and the magnitude of dispersion is $D = +11$ ps/km/nm at the wavelength of 1.55 μm. As the fiber-injected power is increased, the wavelength is continuously shifted toward the longer-wavelength side. When the fiber length was 220 m, the wavelength of the soliton pulse was shifted up to 2.03 μm [4].

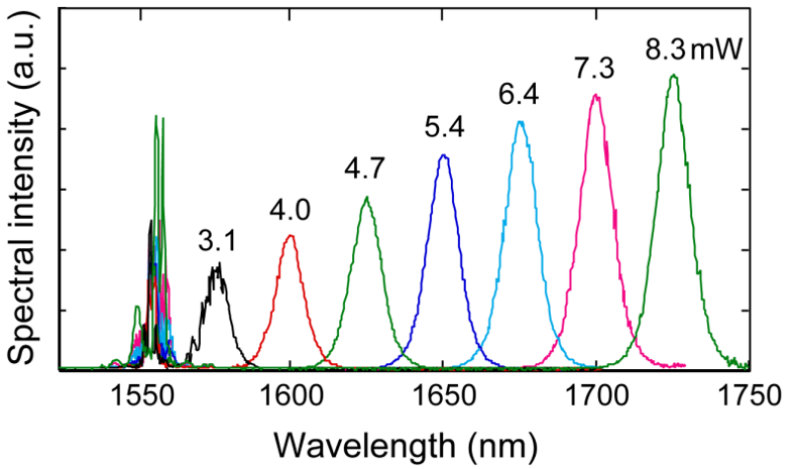

Fig. 3.1 Observed optical spectra at the fiber end when a 100-fs fiber laser pulse is launched into a diameter-reduced PMF. Inset values are the corresponding optical input power. The fiber length is 220 m.

3.3.2 Quasi-SC generation

This generation system of the wavelength-tunable soliton pulse is very simple and does not require troublesome operation in the wavelength-tuning. By introducing an intensity modulator, an electronically controllable, high-speed wavelength-tuning can be realized. Figure 3.2 shows the electric control system. The laser power injected into the fiber is modulated through an acousto-optic modulator (AOM). The wavelength of the soliton pulse can be tuned simply by controlling the input voltage into the AOM. An optical filter is used to remove the pump pulse at 1.56 μm coming together with the soliton pulse.

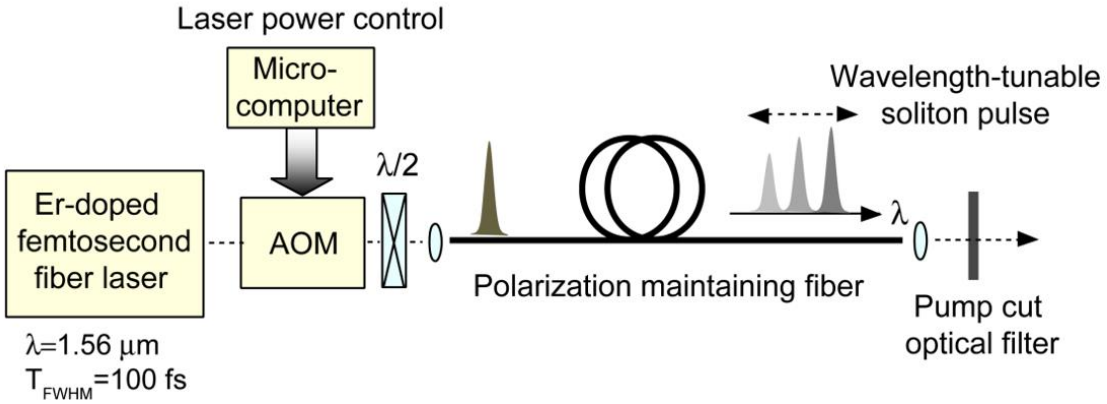

Fig. 3.2 Setup of the electronically controlled high-speed wavelength-tunable Raman soliton pulse generator: AOM, acousto-optic modulator.

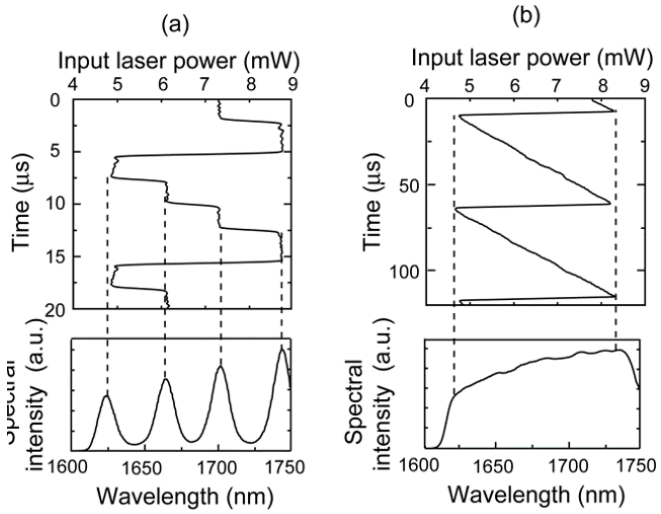

Fig. 3.3 (a) Time-division wavelength multiplexing and (b) wavelength-scanning operations of the Raman soliton pulses when step-like or sawtooth modulations are given to the fiber-injected laser power. Optical spectra were observed with the optical spectrum analyzer.

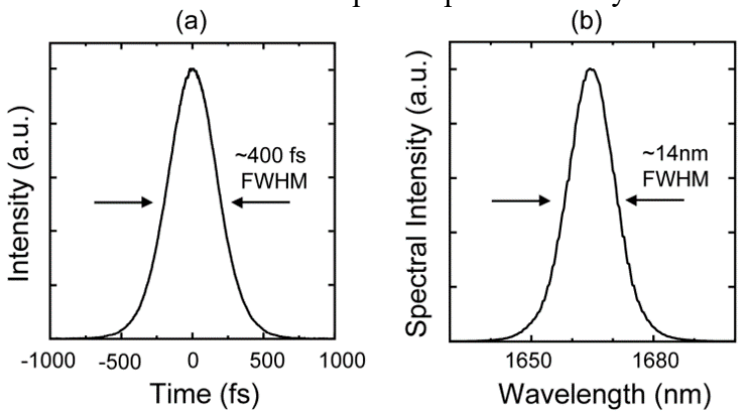

Fig. 3.4 (a) Measured autocorrelation trace and (b) optical spectrum of the Raman soliton pulse at the wavelength of 1.67 μm when a 220-m-long PMF was used.

Figure 3.3 shows the wavelength variation of the soliton pulse when we give step-like and sawtooth changes to the fiber-injected laser power. Since the soliton wavelength accurately changes in response to the laser power, the time-division wavelength multiplexing and wavelength scanning operations can be executed. In these experiments, the wavelength tuning as fast as 2.5-μs intervals has been demonstrated. Furthermore, by detecting a part of the fiber-output power which corresponds to the soliton wavelength, we can also realize the wavelength stabilization for a long time using the feedback control. Figure 3.4 shows the observed autocorrelation trace and optical spectrum of the Raman soliton pulse at the wavelength of 1.67 μm when a 220-m-long PM fiber was used. The pedestal-free good traces were observed, and these corresponded to sech^2 pulse. The temporal width of the autocorrelation trace was 400-fs FWHM, and the actual width of the soliton pulse was estimated to be 260 fs. The temporal width of the soliton pulse was almost constant even if the soliton wavelength was changed. The spectral width was about 14 nm FWHM. The time-bandwidth product is 0.367, and this value is almost in agreement with that of the Fourier transform-limited sech^2 pulse, which

is 0.315. This wavelength-tunable soliton pulse generator has no mechanical part and is very useful for practical applications. Actually, we will use it as base of quasi-SC generation in Chapter 4.

3.4 Pulse propagation in fibers

For an understanding of the nonlinear phenomena in optical fibers, it is necessary to consider the theory of pulse propagation in dispersive nonlinear media. In this chapter, various phenomena induced in the optical fiber are presented. Section 3.4.1 introduces the fiber loss. Sequentially, in Section 3.4.2, we consider the chromatic dispersion of the fiber which causes the pulse broadening in the condition that the nonlinear effect is neglected. Various nonlinear effects, such as self-phase modulation, four-wave mixing, and stimulated Raman, are presented in Section 3.4.3. In Section 3.4.4, we discuss the Raman soliton pulse generation, which is the most interesting and important phenomenon.

3.4.1 Fiber loss

One of the standout features of the optical fiber is low loss. The presence of low-loss fibers has not only sparked a revolution in the field of optical fiber communications but has also ushered in the era of nonlinear fiber optics. Loss is generally given by a ratio of the launched optical power P_i and the transmitted power P_t:

$$\alpha = -\frac{10}{L} log(\frac{P_t}{P_i}) \tag{3.1}$$

where L is the fiber length, and α is typically expressed in units of dB/km. The fiber loss depends on the wavelength of light.

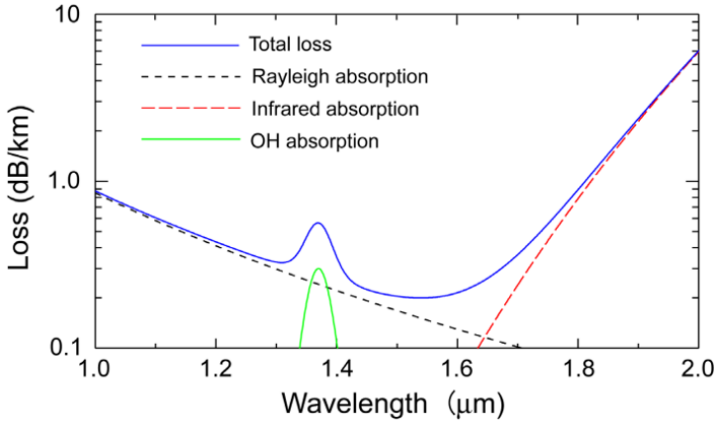

Fig. 3.5 Loss spectrum of a single-mode silica fiber.

Figure 3.5 shows the loss spectrum of a single-mode silica fiber. Currently, the fiber exhibits a minimum loss as low as about 0.2 dB/km at the wavelength of 1.55 μm. Loss increases at shorter and higher wavelengths, reaching a level of a few-tens dB/km. However, even 10 dB/km loss is an incredibly low value compared to that of most other materials. The main factors contributing to the loss are material absorption and Rayleigh scattering. Silica glass has electronic resonances in the ultraviolet region and vibrational resonances in the far-infrared region beyond 2 μm. The most important impurity affecting the loss is the OH ion, which has a fundamental vibrational absorption peak at ~2.73 μm. The overtones of this OH-absorption appear in the wavelength of ~1.4 μm as shown in Fig. 3.5. Rayleigh scattering is a fundamental loss arising from density

fluctuations frozen into the fused silica during manufacture. The Rayleigh-scattering loss varies as λ^{-4} (where λ is the optical wavelength) and is dominant at the short wavelength. This loss is intrinsic and limits the minimum loss of the fiber. As other losses, there are the bending loss and the splice loss which yields when two fibers are connected. The bending loss is now negligibly small, as long as the tight bending is not given to the fiber. By the advance of fusion-splicing technique, the splice loss is now reduced to about 0.01 dB in the splicing between the same kinds of fibers. In the case of heterogeneous fiber splicing, the loss increases to 0.1−0.5 dB due to the difference of the mode-field diameter of fibers.

3.4.2 Chromatic dispersion

Dielectric media have a refractive index of $n(\omega)$ depending on the optical frequency (wavelength). This property is referred to as chromatic dispersion and plays a critical role in the propagation of short optical pulses. Since different spectral components of the pulse travel at different speeds given by $c / n(\omega)$ (where, c is the speed of light in vacuum), the pulse propagating in the dispersive medium suffers the temporal distortion. The effects of the fiber dispersion are accounted for by expanding the propagation constant β in a Taylor series about the carrier angular frequency ω_0 [1]:

$$\beta(\omega) = \beta_0 + \beta_1(\omega-\omega_0) + \frac{1}{2}\beta_2(\omega-\omega_0)^2 + \frac{1}{3!}\beta_3(\omega-\omega_0)^3 + ..., \tag{3.2}$$

where

$$\beta_m = \left(\frac{d^m\beta}{d\omega^m}\right)_{\omega=\omega_0} \tag{3.3}$$

The parameter β_1 is equal to the inverse of the group velocity v_g of the pulse, $\beta_1 = 1/v_g$, which is related to the group delay. Physically speaking, the envelope of an optical pulse moves at the group velocity. The parameter β_2 represents the dispersion of the group velocity and is responsible for pulse broadening. This effect is called "group-velocity dispersion (GVD)". Figure 3.6 shows the temporal and spectral changes caused by the GVD effect for the propagation of a hyperbolic-secant pulse ($I(t) = \mathrm{sech}^2(T/T_0)$, where T_0 is the pulse duration). The curves are plotted in the propagating distance of $z = 2L_D$ and $z = 4\,L_D$. The parameter L_D is referred to as the dispersion length and is given as

$$L_D = \frac{T_0^{\,2}}{|\beta_2|} \tag{3.4}$$

The dispersion length L_D provides the length scale over which the *GVD* effect becomes important for pulse evolution. As the propagation distance increases, we can see that the pulse broadens its temporal width gradually. The *GVD* effect produces no change in the spectral intensity shape but gives the quadratic spectral phase. In the case of $\beta_2 > 0$, the spectrum has the concave downward phase, which is called "up chirp" or "positive chirp". In contrast, $\beta_2 < 0$ gives the convex upward spectral phase ("down chirp" or "negative chirp").

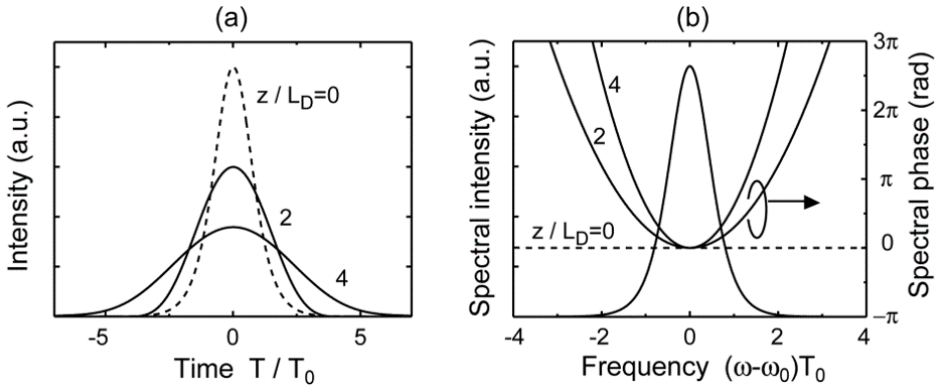

Fig. 3.6 (a) Dispersion-induced temporal broadening and (b) spectral phase variation for the sech^2-shaped pulse propagating in the fiber with $\beta_2 > 0$ at $z = 2L_D$ and $z = 4\ L_D$.

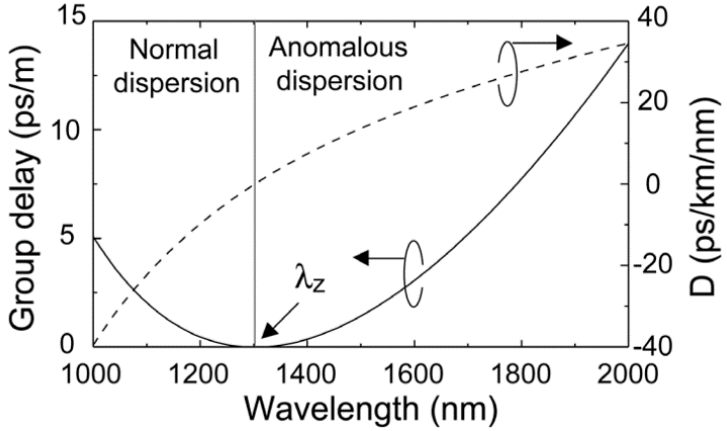

Fig. 3.7 Variation of the group delay and the dispersion parameter D with wavelength for a standard single-mode fiber.

Dispersion parameter D commonly used in the fiber-optics literature is related to β_2 by the relation

$$D = \frac{d\beta_1}{d\lambda} = -\frac{2\pi c}{\lambda^2}\beta_2 \tag{3.5}$$

D is often expressed in units of ps/km/nm. Figure 3.7 shows how the group delay and dispersion parameters of the standard single-mode fiber vary with wavelength. We can see that, at a wavelength of about 1.3 μm, D is zero and the group delay has the minimum value. This wavelength is referred to as the zero-dispersion wavelength λ_z. Nonlinear effects in optical fibers can manifest qualitatively different behaviors, depending on the sign of the dispersion parameter. For wavelengths $\lambda < \lambda_z$, the fiber is said to exhibit normal dispersion as $D < 0$ ($\beta_2 > 0$). In the normal-dispersion region, the short-wavelength components of the optical pulse travel slower than long-wavelength ones. By contrast, the opposite phenomenon occurs in the anomalous dispersion region in which $D > 0$ ($\beta_2 < 0$). The anomalous-dispersion region is of considerable interest because it supports the formation of optical soliton through a balance between dispersion and nonlinear effects. At the zero-dispersion wavelength, the pulse can propagate without pulse broadening in the optical fiber. In the optical telecommunication system, the dispersion-shifted fiber (DSF), whose zero-dispersion wavelength is shifted to 1.55 μm, is introduced in order to suppress the pulse distortion.

The slope of the curve of the dispersion parameter D, which is referred to as the dispersion slope, is related to the third-order dispersion (TOD) parameter β_3. TOD causes the pulse distortion but its effect is small compared with that of β_2. However, when the pulse propagates near the zero-dispersion wavelength, the TOD effect becomes dominant in pulse propagation. In SC generation, the TOD limits the spectral broadening induced by nonlinear effects owing to the pulse distortion.

3.4.3 Nonlinear effects

The dielectric medium such as a silica optical fiber has the nonlinear response for intense electro-magnetic fields. The polarization $\boldsymbol{P}$ induced by electric dipoles is not linear in the electric field $\boldsymbol{E}$, and it is expressed with a more general relation:

$$P = \varepsilon_0(\chi^{(1)} \cdot E + \chi^{(2)} \cdot EE + \chi^{(3)} \cdot EEE + ...) \tag{3.6}$$

where ε_0 is the vacuum permittivity and $\chi^{(j)}$ is the j-th-order susceptibility. The linear susceptibility $\chi^{(1)}$ represents the dominant contribution, and its effects are included through the refractive index n and the attenuation coefficient α. The second-order susceptibility $\chi^{(2)}$ is responsible for such nonlinear effects as second-harmonic generation and sum-frequency generation. However, optical fibers do not normally exhibit these effects because of the symmetric molecular configuration of S_iO_2. The third-order susceptibility $\chi^{(3)}$ induces the effects such as nonlinear refraction, third-harmonic generation, and four-wave mixing (FWM). The nonlinear phenomena in optical fibers are mainly caused by this third-order nonlinearity.

As other important nonlinear effects in optical fibers, there are stimulated inelastic scatterings caused by the interaction between the phonons of silica and light (photons). These phenomena are known as the stimulated Raman scattering (SRS) and the stimulated Brillouin scattering (SBS). The difference between them is that optical phonons contribute in SRS while acoustic phonons contribute in SBS. The light is mainly scattered forward in SRS and is only scattered backward in SBS. In the propagation of the picosecond or femtosecond pulse, the SRS plays important roles. In this section, we describe the nonlinear refraction effect which induces the self-phase modulation and the cross-phase modulation. Then, the FWM and the SRS in the optical fiber are mentioned.

The nonlinear refraction caused by third-order nonlinearity is the most important nonlinear phenomenon in optical fibers. When the intense optical pulse propagates into a dielectric medium, the refractive index n of the medium changes depending on the optical intensity $|E|^2$:

$$n = n_0 + n_2 |E|^2 \tag{3.7}$$

where n_0 is the inherent refractive index of silica glass and n_2 is the nonlinear-index coefficient. The value of $n_2 = 3.18 \times 10^{-20} m^2 / W$ is estimated in silica fibers, and its value changes depending on the material doped into the fiber core. The nonlinear refraction is also called “optical Kerr effect”. For the propagation of the ultrashort pulse, this effect leads to the spectral broadening. The optical pulse suffers the nonlinear phase shift by the intensity dependence of the refractive index, and consequently, the temporal frequency change is caused:

$$\omega(T) = \omega_0 - \frac{\omega_0 n_2}{c} z \frac{\partial |E(T)|^2}{\partial T} \tag{3.8}$$

Equation (3.8) shows that the instantaneous frequency of the pulse depends on the temporal shape $|E(T)|^2$. The frequency at the leading part of the pulse becomes lower than the carrier frequency, and in contrast, the opposite frequency shift occurs at the trailing part of the pulse as shown in Fig.3.4. This phenomenon is called "self-phase modulation (SPM)" because of the origin that the inter-pulse phase changes depending on its own intensity profile. Figure 3.5 shows the temporal and spectral variations caused by the SPM effect. The curves are plotted for the sech^2-shaped pulse propagation at $z = 5\ L_{\text{LN}}$ and $z = 10\ L_{\text{LN}}$ when GVD effect is neglected. If GVD effect does not exist, the pulse exhibits no temporal change and the spectrum keeps broadening during the propagation. The parameter L_{LN}, which is referred to as the nonlinear length, provides the length scale over which the nonlinear effect becomes important for pulse evolution and is given as

$$L_{LN} = \frac{1}{\gamma P_0} \tag{3.9}$$

where γ is the nonlinear coefficient and P_0 is the peak power of the pulse. γ is related to the nonlinear-index coefficient n_2 and the effective core area A_{eff} as follows:

$$\gamma = \frac{n_2 \omega_0}{c A_{\text{eff}}} \tag{3.10}$$

A_{eff} depends on the fiber parameters such as the core radius and the core-cladding index difference, and is given with the mode-field diameter (MFD) of the fiber $2w$ as $A_{\text{eff}} = \pi w^2$. Typically, the MFD is ~10 μm and A_{eff} is ~80 μm^2 at the wavelength of 1.55 μm. The nonlinear coefficient γ takes a value of ~2$W^{-1}km^{-1}$ in the standard single-mode fiber. In highly nonlinear fibers and micro-structured photonic crystal fibers, the value of >10 $W^{-1}km^{-1}$ is now realized by reducing the effective area and by doping with other materials with high n_2 [2, 3]. In SC generation, SPM effect plays the most important role and it causes dramatic spectral broadening and soliton formation in the anomalous GVD region of the fiber.

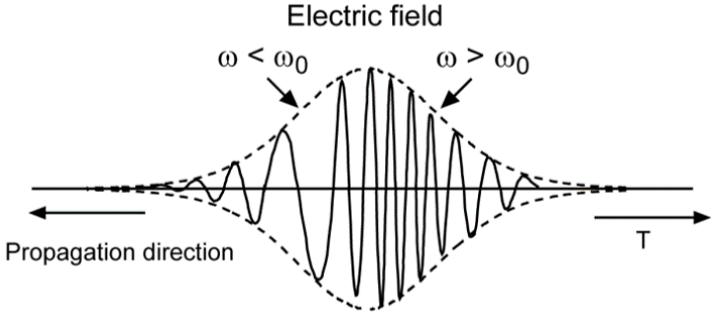

Fig. 3.8 Schematic diagram of the nonlinear frequency chirp by self-phase modulation.

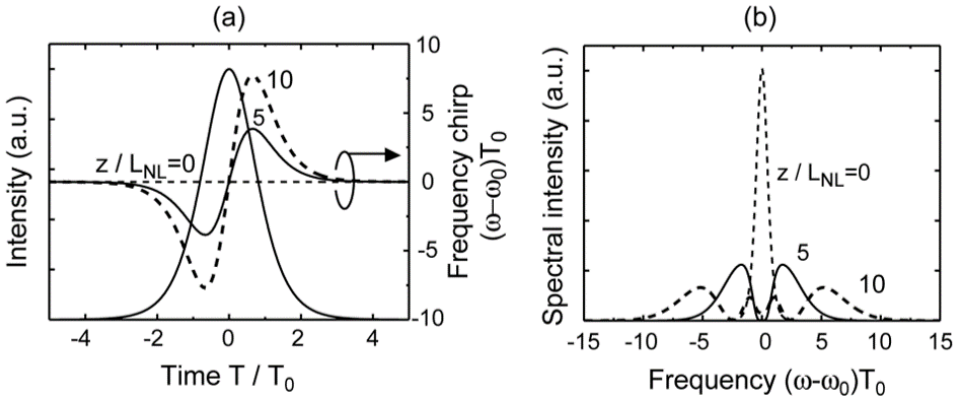

Fig. 3.9 (a) Temporal variations of the SPM-induced frequency chirp and (b) broadened spectra for the sech2-shaped pulse propagation at $z = 5\ L_{LN}$ and $z = 10\ L_{LN}$. The effect of GVD is neglected.

The intensity-dependent phase shift also occurs when the multiple optical fields temporally superpose during the propagation. The behavior of a pulse in a nonlinear medium is influenced not only by its own intensity but also by the intensity of other copropagating pulses. This phenomenon is known as "cross-phase modulation (XPM)". XPM can give phase and spectrum changes to the weak pulse by use of other intense pulse field. This effect is now used for optical switching and pulse compression.

Four-wave mixing is the nonlinear interaction among four optical waves through the third-order susceptibility $\chi^{(3)}$ in Eq. (3.6). FWM can generate the new waves with different frequencies (wavelengths) from the pump waves. In quantum-mechanical terms, FWM is the phenomenon in which one or more photons are annihilated and new photons are created at different frequencies such that the net energy and momentum are conserved during the interaction. This phenomenon requires the matching of the frequencies as well as that of the wave vectors (phases). When two pump photons at frequencies ω_1 and ω_2 are annihilated and simultaneously two photons at frequencies ω_3 and ω_4 are created as shown in Fig. 3.6, the matching conditions are given as follows:

$$\omega_3 + \omega_4 = \omega_1 + \omega_2 \tag{3.11}$$

$$\begin{aligned} \Delta\phi &= \Delta\phi_L \Delta\phi_{LN} \\ &= [\beta(\omega_3) + \beta(\omega_4) - \beta(\omega_1) - \beta(\omega_2)]z + \gamma(P_1 + P_2)z \\ &= 0 \end{aligned} \tag{3.12}$$

where $\Delta\phi_L$ is the linear phase difference and $\Delta\phi_{LN}$ is the nonlinear phase induced by the pump waves with the power $P_{1,2}$. The generated waves with low and high frequencies are often referred to as the Stokes and the anti-Stokes, respectively. In optical fibers, it is relatively easy to satisfy $\Delta\phi = 0$ in the partially degenerated case $\omega_1 = \omega_2$. A strong pump wave at ω_1 creates two sidebands located symmetrically at frequencies ω_3 and ω_4. When the pump wave is injected near zero-dispersion wavelength of the fiber, it is comparatively easy to achieve the phase matching. In anomalous GVD regions, the SPM-induced nonlinear phase by pump wave $\Delta\phi_{LN}$ can cancel the linear phase mismatch $\Delta\phi_L$.

Both SPM-induced spectral broadening and generation of the new spectral components by FWM are nonlinear phenomena through the third-order nonlinear interaction between the electron and the electric field in the medium. However, FWM only occurs when the pump wave and generated waves are temporally

superposed. In contrast, SPM generates new spectral components at leading and trailing parts of the pulse and these are temporally separated. Therefore, the relation between the sideband waves generated in FWM process can be distinguished from that between the long-wavelength and short-wavelength components generated in SPM-induced spectral broadening.

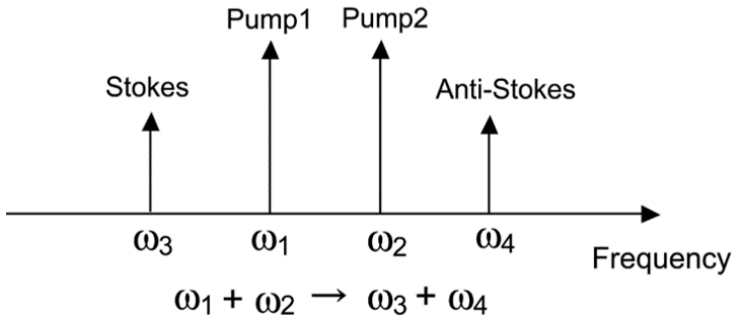

Fig. 3.10 Schematic diagram of four-wave mixing process that two photons at frequency ω_1 and ω_2 are annihilated and simultaneously two photons at frequencies ω_3 and ω_4 are created.

Stimulated Raman scattering is a nonlinear phenomenon where the energy from a pump wave transfers to a Stokes wave as the pump wave propagates through the optical fiber. In the simple quantum-mechanical picture, this phenomenon can be explained as that a photon of the pump is annihilated and a photon with a lower frequency and a phonon with the right energy and momentum are created to conserve the energy and the momentum. SRS occurs only when the pump power surpasses a specific threshold level. Figure 3.7 shows the Raman-gain spectrum for fused silica. It is evident that the Raman gain spans a considerable frequency range, reaching up to 40 THz, with a broad peak concentrated around 13 THz. In most molecular media, the Raman gain occurs at specific well-defined frequencies. However, the silica fiber extends continuously over a broad range. The origin of the broadband spectrum is due to its non-crystalline nature. If the pump beam at the frequency ω_p propagates with the probe beam at ω_s in the optical fiber, the probe beam is amplified because of the Raman gain, as long as the frequency difference $\Delta\omega = \omega_p - \omega_s$ lies within the bandwidth of the Raman-gain spectrum. For the ultrashort pulse with high power, SRS transfers the energy of the short-wavelength component to the long-wavelength one inside one pulse. This phenomenon is referred to as the inter-pulse Raman scattering. In the anomalous GVD region of the optical fiber, under suitable conditions, almost all of the pump-pulse energy can be transferred to a red-shifted Raman pulse and it propagates as a fundamental soliton pulse.

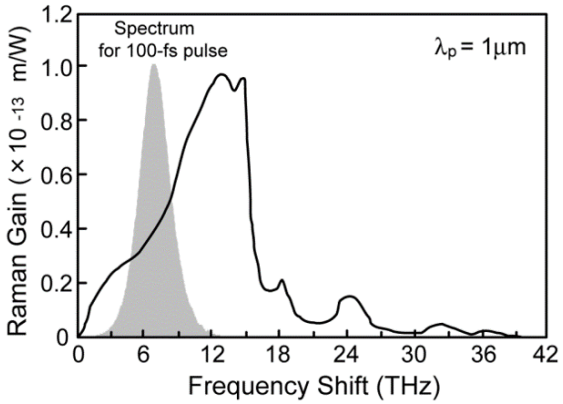

Fig. 3.11 Raman-gain spectrum for fused silica at a pump wavelength of λ_p = 1 μm. The optical

spectrum for a 100-fs duration pulse is also shown.

3.4.4 Soliton effect

In the anomalous GVD region of the optical fiber, the optical soliton can be formed as a result of the interplay between the GVD and nonlinear effects. The word “soliton” refers to special kinds of wave packets that can propagate without distortion over long distances and it originates from “solitary wave”.

We now assume that the optical pulse with the SPM-induced frequency chirp propagates in the optical fiber. This pulse has a lower frequency compared with the carrier frequency at the leading part of the pulse and in contrast, has a higher frequency at the trailing part. If such pulse propagates in the normal GVD region of the fiber, the pulse is dispersed away because low-frequency components in the optical pulse travel fast and high-frequency components travel slow compared with the center part of the pulse. By contrast, in the case of the anomalous GVD region, the pulse suffers the pulse compression effect because of the opposite property for the propagating speed. If this nonlinear pulse compression and the pulse broadening by the GVD effect are balanced, the pulse can propagate without distortion in the fiber. In the viewpoint of the chirp, the undistorted pulse can be formed when the positive chirp induced by the SPM effect matches the negative chirp induced by the GVD effect [1]. Such an optical pulse is referred to as the optical soliton (fundamental soliton), and this phenomenon is also referred to as the soliton effect. The mathematical expression of the fundamental soliton pulse in a frame of reference moving with the pulse at the group velocity is given as

$$A(z,T) = \sqrt{P_0}\exp(i\frac{|\beta_2|}{2T_0}z)\operatorname{sech}\left(\frac{T}{T_0}\right) \tag{3.13}$$

where A is the complex electric field envelope of the pulse. We can see that the soliton pulse has a hyperbolic-secant profile and it propagates without change in shape for arbitrarily long distances. The peak power P_0 of the fundamental soliton pulse should satisfy the next equation:

$$P_0 = \frac{|\beta_2|}{\gamma T_0} \approx \frac{3.11|\beta_2|}{\gamma T_{FWHM}^2} \tag{3.14}$$

where T_{FWHM} is the pulse duration in the full width at half maximum (FWHM) and there is the relation $T_{\mathrm{FWHM}} \approx 1.763T_0$.

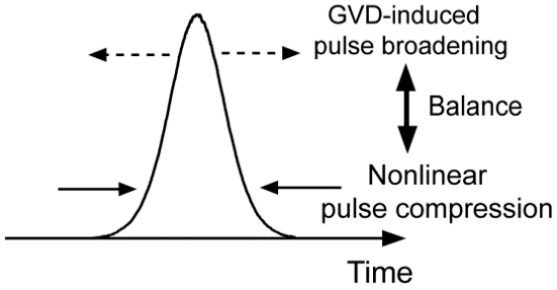

Fig. 3.12 Principle of fundamental soliton formation in the optical fiber.

If the pulse with the peak power exceeding the fundamental power shown in Eq. (3.14) is injected into fiber, it can propagate as the higher-order soliton pulse. In this case, the temporal shape and spectrum of the pulse

vary periodically during the propagation. The soliton number N which indicates the degree of the higher-order soliton pulse is given by

$$N^2 = \frac{L_D}{L_{LN}} = \frac{\gamma P_0 T_0^{\ 2}}{|\beta_2|} \tag{3.15}$$

Figure 3.13 shows the propagation evolution of the second-order soliton (N = 2). The evolution of the higher-order soliton pulse is periodic with propagation period z_0, which is given as

$$z_0 = \frac{\pi}{2} L_D = \frac{\pi}{2} \frac{T_0^{\ 2}}{\beta_2} \tag{3.16}$$

As the pulse propagates along the fiber, it first contracts to a fraction of its initial width and then recovers the original shape again at the end of the soliton period at $z_0 = z$. This evolution results from an interplay between the SPM and GVD effects. The SPM effect dominates initially but the GVD effect soon catches up and leads to pulse contraction. This effect is known as the higher-order soliton compression and is used to compress the optical pulse.

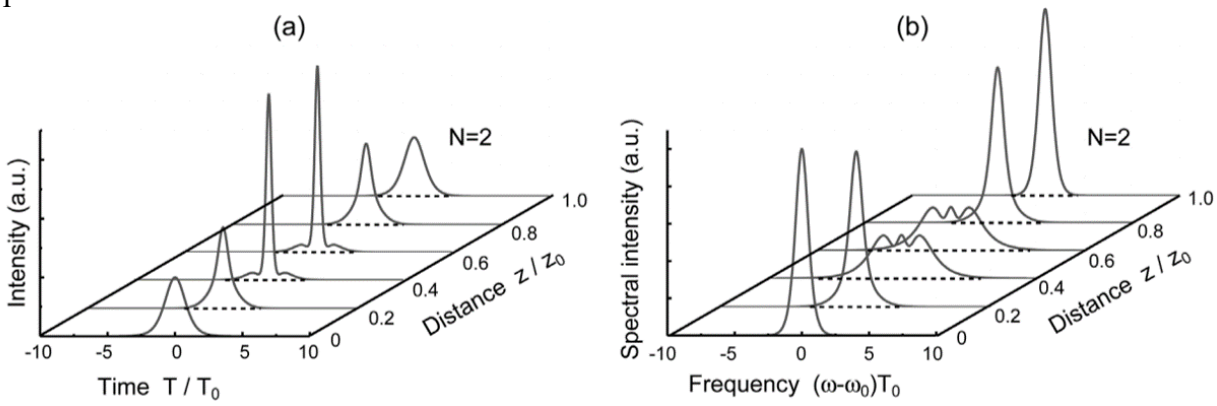

Fig. 3.13 (a) Temporal and (b) spectral evolution over one soliton period for the second-order soliton pulse (N = 2).

When the ultrashort pulse with a high-peak power propagates in the optical fiber with the anomalous dispersion, the Raman soliton pulse whose wavelength is shifted toward the longer-wavelength side is generated by the combination of the soliton effect and the stimulated Raman scattering. The wavelength of the soliton pulse can continuously shift with keeping its sech^2 shape during the propagation. Figure 3.14 shows how the ultrashort pulse evolves to the Raman soliton in the optical fiber. When (a) the ultrashort pulse is injected into fiber with the anomalous dispersion, (b) the spectrum of the pulse is first broadened by the effect of higher-order soliton compression. If the peak power of the pulse exceeds the Raman threshold level, (c) inter-pulse SRS occurs and the long-wavelength components in the broadened spectrum are amplified. (d) The amplified Raman components suffer the soliton effect, and a fundamental soliton pulse is gradually formed. In the temporal domain, the pulse breaks up and the soliton pulse delays from the input pulse due to the group-velocity difference between these pulses with different wavelengths. Inter-pulse SRS also occurs in the generated Raman soliton pulse. The energy of the shorter-wavelength components in the Raman soliton pulse is transferred to the longer-wavelength components in the same pulse. Consequently, (e) the center wavelength of the pulse is shifted toward the longer wavelength side. Since the pulse also suffers the soliton

effect, the $sech^2$ shape is kept during the propagation. The phenomenon that the wavelength shift of the soliton pulse is called “soliton self-frequency shift”.

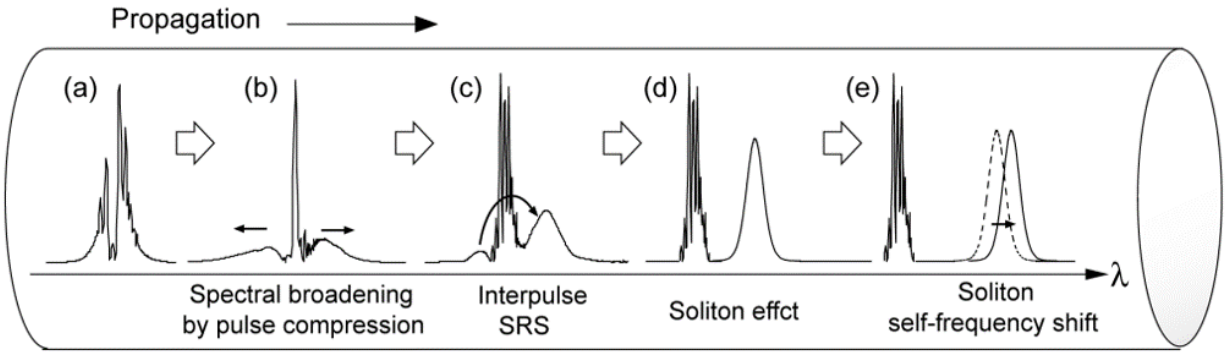

Fig. 3.14 Schematic spectral evolution in Raman soliton pulse generation.

3.5 Summary

In this chapter, SC and quasi-SC generation have been presented. On the other hand, the theory of the pulse propagation and various phenomena induced in the optical fiber have been presented. In optical fibers, the chromatic dispersion distorts the temporal pulse shape and the nonlinear effects cause the spectral variation. The interplay between the GVD and nonlinear effects forms the optical soliton pulse. Furthermore, the contribution of the stimulated Raman scattering leads to the soliton self-frequency shift. We presented the wavelength-tunable Raman soliton pulse generation. The ideal $sech^2$-shaped soliton pulse was generated only by passing the femtosecond pulse into the optical fiber. We have demonstrated an electronically controllable, high-speed, wavelength-tuning of the Raman soliton pulse.

Reference for Chapter 3

[1] W. Drexler and J. G. Fujimoto, “Optical Coherence Tomography: Technology and Applications,” 2rd ed. Springer Reference, Chapter 17 (2015).

[2] G. P. Agrawal, “Nonlinear Fiber Optics,” 3rd ed. (Academic, San Diego, 2001).

[3] P. Petropoulos, H. Ebendorff-Heidepriem, V. Finazzi, R. C. Moore, K. Frampton, D. J. Richardson, and T. M. Monro, “Highly nonlinear and anomalously dispersive lead silicate glass holey fibers,” *Opt. Express* **11**, 3568 (2003).

[4] N. Nishizawa and T. Goto, “Compact system of wavelength-tunable femtosecond soliton pulse generation using optical fibers,**”** *IEEE Photon. Technol. Lett.* **11**, 325 (1999).

Chapter 4 Development of tunable quasi-supercontinuum laser source

4.1 Introduction

As mentioned in Chapter 2, the performance of optical coherence tomography (OCT) is determined by the specifications of the light source. The axial resolution is inversely proportional to the bandwidth of the light source, given by equation (2.7). Figure 4.1 shows the axial resolution in biological imaging varied with the bandwidth of the light source. Biological tissues have a refractive index of 1.38 for light. The light source spectrum is assumed to be Gaussian-shape with central wavelengths of 0.8, 1.1, 1.3, and 1.7 μm respectively. The ultra-broadband spectral light source with a bandwidth of hundreds of nanometers enables ultrahigh axial resolution of less than 10 μm [1-5]. The ultrahigh resolution OCT is a helpful tool for detailed imaging of human retinal layer structure and cells or organelles in biological tissues [1,6]. Thus, the development of broadband light sources for OCT imaging is necessary.

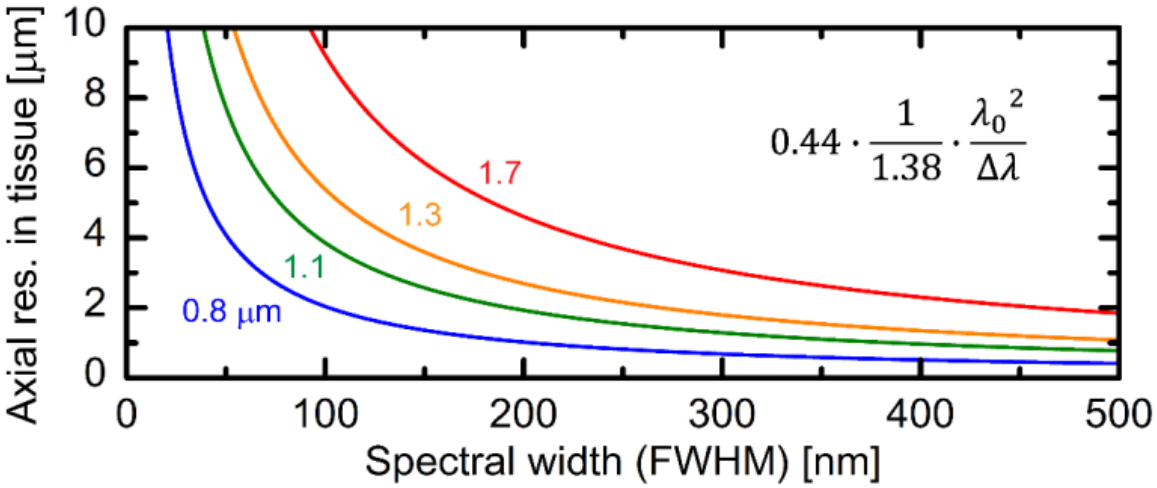

Fig. 4.1 Axial resolution in terms of light bandwidth.

In addition, the operation wavelength has a crucial impact on the penetration depth for biological tissue imaging. Compared to visible spectral band (0.4–0.8 μm), near-infrared wavelength range (wavelength >0.8 μm), which has fewer light-absorbing substances and is less affected by scattering, is often chosen for deep tissue imaging [7-10]. However, the imaging depth is still limited for highly scattering tissues such as the brain and skin, typically in the range of several hundred micrometers to around 1 mm [11-16]. The primary limiting factors include light scattering and water absorption. Figure 4.2 shows the schematic of light attenuation due to water absorption and scattering in biological tissues [17-19]. Figure 4.3 shows the wavelength dependence of light attenuation caused by water absorption and light scattering at different optical windows for biological tissue imaging. The third window from 1600 nm to 1900 nm, also called as 1.7 μm spectral band, which has a local minimum water absorption and decreased scattering, absorbs lots of interest in the field of bio-imaging [20].

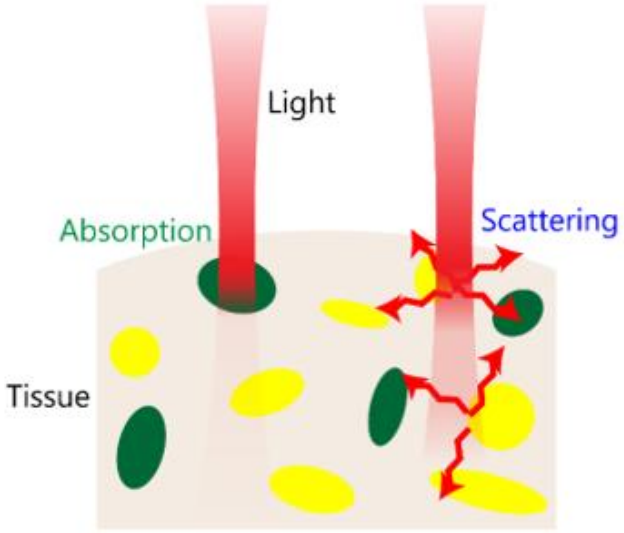

Fig. 4.2 Schematic of quasi-SC generation

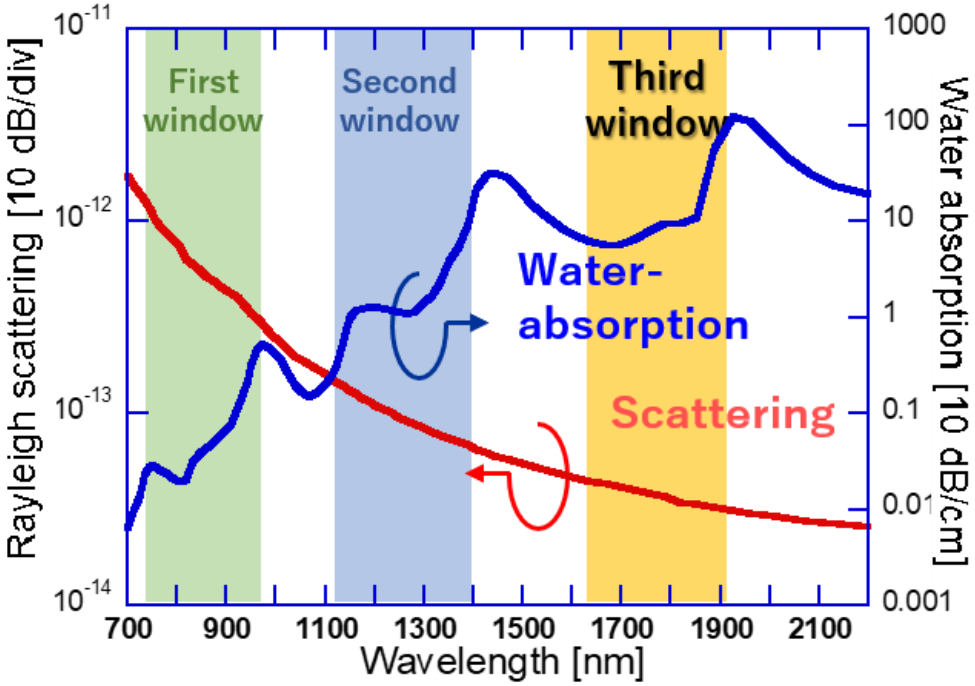

Fig. 4.3 Light attenuation at different optical windows for biological tissue imaging.

As described in Chapter 1, the SLDs, solid-state lasers, and SC sources have been developed for OCT imaging. The bandwidth and the operation wavelength of SLD and ultra-short pulse solid-state lasers are determined by the gain medium, making it difficult to control. In contrast, the central wavelength of SC can be adjusted arbitrarily by controlling the central wavelength of the ultra-short pulse light serving as a seed source, and a flexible tuning range (0.8–2.0 μm) in the near-infrared region is able to be obtained. Additionally,

since the spectral width of SC light can be extended by nonlinear effects, ultra-broadband spectra in excess of 300 nm can be generated without being limited by the bandwidth of the gain medium, enabling OCT imaging with high transmission depth. The 1.7 μm SC with ultra-broadband spectrum facilitates OCT imaging with both high-depth penetration and high resolution [1,2,4,6,21-24]. It is reported that a maximum imaging depth of 1.7 mm with an axial resolution of 3.6 μm in mouse brain imaging has been achieved by 1.7 μm SC source [24]. Especially, the high-power coherent SC generation improves imaging capabilities with the benefits of high-sensitivity and larger penetration depth because of low spectral intensity noise [24.26].

However, the spectral shape and wavelength range are also limited by the fiber devices used and the characteristics of the seed pulse source, and generally, it is difficult to control the spectral shape of the generated SC [27-29]. In 2008, Sumimura *et al.* developed a new broadband light source—a quasi-supercontinuum (SC) source, whose spectrum looks like a SC and is controllable [30]. They continued their work and demonstrated 1.3 μm quasi-SC generation for time domain (TD) OCT imaging in 2010. A high axial resolution of 3.7 μm in tissue was obtained. A maximum sensitivity of 100 dB was achieved, and ultrahigh-resolution images of a hamster cheek pouch were observed [31]. It is expected that a 1.7 μm broadband quasi-SC can be developed for high resolution deep tissue imaging.

In this chapter, we demonstrated the development of a tunable quasi-supercontinuum generation at 1.7 μm spectral band based on wavelength-tunable soliton pulse generation and fast intensity modulation. In Section 4.2, we explained the principle of quasi-SC generation using the nonlinear dispersive fiber. In Section 4.3, we presented the details about experimental development of tunable Gaussian-shaped quasi-SC generation, including seed pulse generation, wavelength-tunable soliton pulse generation, and fast intensity modulation. In Section 4.4, the noise properties for quasi-SC was examined. And we compared the output properties between quasi-SC and a conventional SC. Finally, a summary was given about the development of 1.7 μm broadband quasi-SC.

4.2 Principle of quasi-supercontinuum generation

Figure 4.4 illustrates the schematic of quasi-SC generation. The underlying principle of quasi-SC involves a combination of wavelength-tunable Raman soliton pulse generation and fast intensity control [32,33]. As described in Chapter 3, when an ultrashort pulse with high peak power propagates through the nonlinear dispersive fiber (NLDF), a Raman soliton pulse gradually forms during fiber transmission through the following process: As the ultrashort pulse is coupled into an anomalous-dispersion fiber, the pulse spectrum undergoes initial broadening because of the higher-order soliton compression effect. Subsequently, intra-pulse stimulated Raman scattering (SRS) enhances the longer-wavelength components in the broadened spectrum. This leads to pulse breakup, generating an ultrashort pulse on the longer wavelength side. The generated pulse experiences the soliton effect, gradually forming a sech^2-shaped soliton pulse. Intra-pulse SRS further causes the energy of the shorter-wavelength components in the Raman soliton pulse to transfer to the longer-wavelength components within the same pulse. This results in the central wavelength of the Raman soliton shifting toward the longer-wavelength side. With an increase in fiber length and input power, the central wavelength of the Raman soliton shifts more toward the longer wavelength side. By modulating the input soliton intensity using a fast modulator, the shifted Raman solitons appear to be generated simultaneously, producing a detected spectrum that appears super-continuous—termed quasi-supercontinuum (quasi-SC).

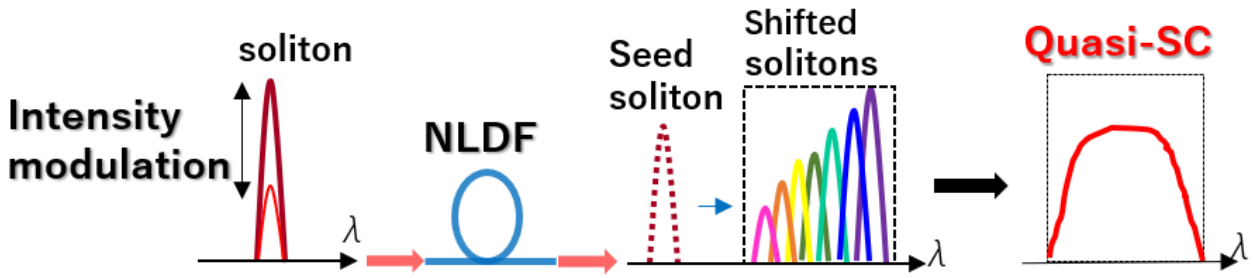

Fig. 4.4 Schematic of quasi-SC generation

In this quasi-SC generation, the central wavelength, bandwidth, and spectral shape are tunable. This characteristic not only enables the realization of high resolution and large penetration depth through the use of a broadband quasi-SC, but also facilitates the acquisition of uncorrelated speckle patterns by employing multiple quasi-SC outputs within a tunable wavelength region.

4.3 Experimental setup for quasi-supercontinuum laser source

The experimental setup for quasi-SC generation is shown in Fig 4.5. The quasi-SC source consists of four parts: (1) the seed pulse source, (2) the seed pulse intensity amplifier, (3) the nonlinear fiber, and (4) the fast intensity modulator. We utilized an Er-doped ultrashort-pulse fiber laser using a single-wall carbon nanotube (SWNT) polyimide film as the saturable absorber, and the ultrashort pulse was amplified by an Er-doped fiber amplifier (EDFA) to obtain a wider wavelength-tunable spectral band. After a polarization-maintaining (PM) fiber, a new Raman soliton pulse is formed. The wavelength of the Raman soliton shifted more toward the longer wavelength side with the increase of PM fiber input power. Then, we inserted an electro-optical (EO) intensity modulator (Thorlabs LN81S-FC) between the seed pulse and EDFA to change the power of the amplified pulse. A long pass filter was used after the PM fiber to remove the seed pulse. The cut-off wavelength was 1.6 μm. Two combinations composed of a half-wave plate and a quarter-wave plate were also introduced to match the polarization direction of the pulse beam with the birefringent axis of the fiber. The first combination after the seed pulse source helped to obtain the highest amplified power, whereas the second one before the PM fiber caused the Raman soliton to be shifted to the longest wavelength. In the following subsections, we will give the detailed information about the above four components.

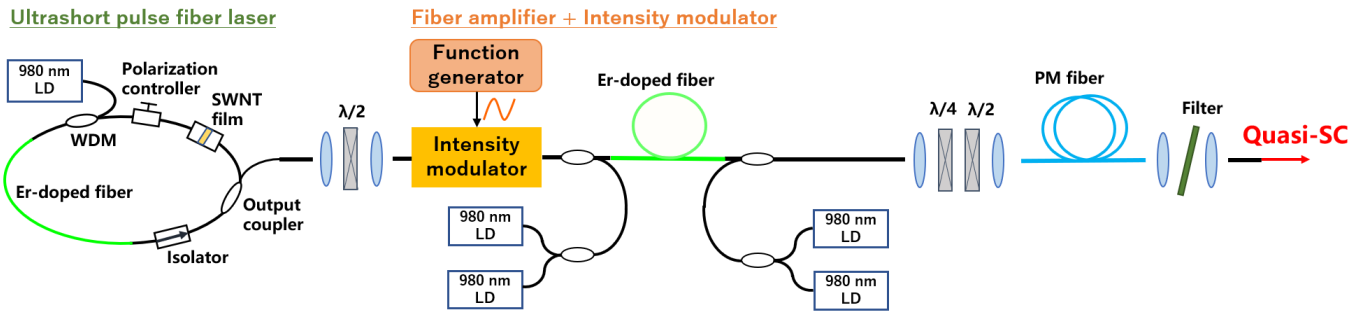

Fig. 4.5 Experimental setup for quasi-SC generation

4.3.1 Ultrashort pulse fiber laser using a single-wall carbon nanotube (SWNT) polyimide film

Passively mode-locked ultrashort pulse fiber lasers offer advantages in nonlinear optical processes due to their ultrashort pulse duration, stability, reliability, and so on [34-37]. In passively mode-locked pulse lasers, the single-wall carbon nano-tube (SWNT), which has saturable absorption properties in the near-infrared region with ultrafast saturation recovery times of ~1 ps has been widely used for mode locking that generate repetitive ultrashort pulse trains [38-44]. In particular, film-type SWNT is easier to be installed between the fiber connector due to its flexibility. Furthermore, in the case of polarization-maintaining (PM) fibers, the incorporation of film-type SWNT aids in the automatic alignment of the birefringent axes of PM fibers at the fiber connector. This facilitates passive mode-locking within a straightforward all-fiber ring cavity configuration, eliminating the need for additional polarization devices. [39,40].

In this work, we utilized a passively mode-locked Er-doped ultrashort-pulse fiber laser using a single-wall carbon nanotube (SWNT) polyimide film as the seed pulse source [45]. Figure 4.6 shows the configuration of the ultrashort-pulse fiber laser. A high-power laser diode (LD) operating at a wavelength of 980 nm served as the pump laser for the experiment. The pump beam was directed into a 1.2 m long polarization-maintaining (PM) erbium-doped fiber (EDF) via a polarization-maintaining wavelength division multiplexed (PM-WDM) coupler. The PM-EDF exhibited a peak absorption of 55 dB at a wavelength of 1550 nm. To construct an all-polarization-maintaining fiber ring laser, the PM-EDF was fusion-spliced with a PM isolator and a 1:1 PM coupler. The connection between the PM isolator and the fiber coupler involved mechanical coupling using an angled polished FC/APC fiber connector. The total length of the cavity was approximately 5 m. As a mode-locker, a freestanding SWNT-polyimide nanocomposite film was employed. The film had a thickness of 17 μm and exhibited a broad absorption spectrum, with an absorbance of about 0.3 at a wavelength of 1.55 μm. The refractive index of the polyimide film was approximately 1.58. A small section of the film measuring 2 mm × 2 mm was utilized as the saturable absorber in the setup.

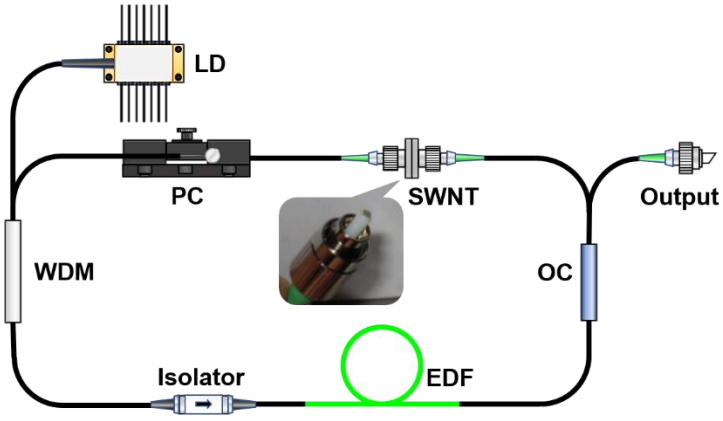

Fig. 4.6 Configuration of ultrashort-pulse, Er-doped fiber laser using SWNT.
OC: output coupler; PC: polarization controller.

Figure 4.7 shows the spectrum from 1.55 μm ultrashort pulse Er-doped fiber laser using SWNT. The ultrashort pulse had an ideal $sech^2$-shape with a spectral width of 5.3 nm full-width at half-maximum (FWHM) and a central wavelength of 1556 nm. The average output power was about 23 mW. Figure 4.8 (a)shows the pulse train observed by a fast pin photodiode (EOT ET-5000) and a digital oscilloscope (Yokogawa DL9040L). A consistently clean pulse train was observed, with a temporal separation of 10.4 ns between each pulse.

Figure 4.8 (b) shows the RF spectra captured using a fast pin photodiode and an RF spectrum analyzer (Anritsu MS2830A). The RF spectra exhibited equal-frequency-spanning characteristics with nearly constant amplitude, extending up to a few GHz range, confirming the stability of passive mode-locking. An enlarged view of the RF spectra, specifically focusing on the fundamental frequency, is also presented in Figure 4.8 (c). The repetition frequency measured 95.5 MHz, and the SNR reached approximately 78 dB. This indicates that the noise level of the output pulse train was sufficiently low for subsequent applications. The characteristics of the generated ultrashort pulse are summarized in Table 4.1.

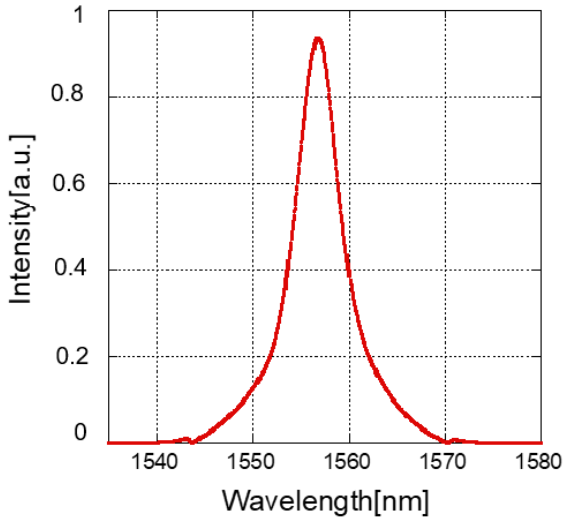

Fig. 4.7 Spectra of ultrashort-pulse, Er-doped fiber laser using SWNT.

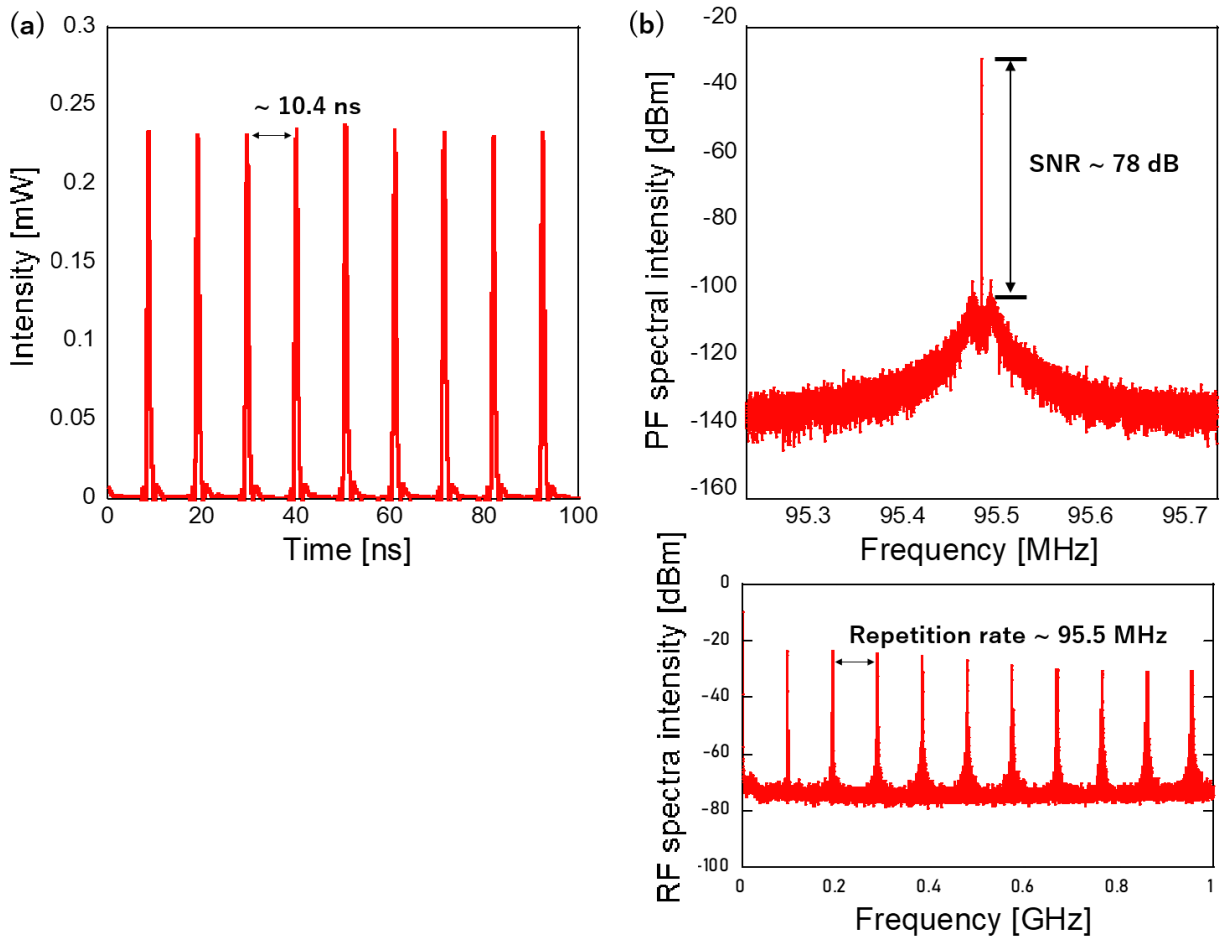

Fig. 4.8 (a) Pulse train and RF spectra of fundamental frequency and wide range.

Table 4.1 Main characteristics for ultrashort seed pulse for quasi-SC generation.

Averaged power	23 mW
Spectral width	5.3 nm
Center wavelength	1556nm
Repetition frequency	95.5 MHz

4.3.2 Wavelength-tunable ultrashort pulse generation using polarization-maintaining (PM) fiber

In order to obtain widely wavelength-tunable range at 1600 -1900 nm spectral band, the averaged power of ultrashort seed pulse has to be increased by a pulse-energy amplifier. We used an Er-doped fiber amplifier (EDFA) for high-power soliton pulse generation. Generally, optical fibers have anomalous-dispersion characteristics in the wavelength region around 1.55 μm. This anomalous dispersion causes excessive nonlinear effects such as induced Raman scattering and high-order soliton compression in dealing with the

high-power ultrashort pulse. In this work, we used the normally-dispersive Er-doped fiber (EDF) to avoid the uncontrollable nonlinear effects and to amplify the pulse energy effectively.

For wavelength-tunable pulse generation, we used polarization-maintaining (PM) fiber as a soliton pulse wavelength-shifting device. When an ultrashort pulse is coupled into a PM fiber, the pulse spectrum is initially broadened by the higher-order soliton compression effect, as described in Chapter 3. Then the longer-wavelength components in the broadened spectrum are enhanced through intra-pulse stimulated Raman scattering (SRS). As a result, pulse breakup occurs, and an ultrashort pulse is generated at the longer wavelength side. The generated pulse experiences the soliton effect, and a $sech^2$-shaped soliton pulse is gradually generated. Intra-pulse SRS also causes the energy of the shorter-wavelength components in the Raman soliton pulse to be transferred to the longer-wavelength components in the same pulse, resulting in the central wavelength of the Raman soliton shifting toward the longer-wavelength side. It is found that by varying merely the PM fiber-input power, the wavelength of the soliton pulse is shifted almost linearly in the wide region of 1.6–2.0 μm, and the wavelength shift is also positively correlated with fiber length. In addition, the use of PM fiber makes the generated wavelength-shifted solitons stable in both central wavelength and output power, and insensitive to environmental fluctuations.

The experiment setup for wavelength-tunable soliton pulse generation using EDFA and PM fiber is shown in Fig.4.9. The Er-doped ultrashort-pulse fiber laser using a single-wall carbon nanotube (SWNT) polyimide film worked as the seed pulse source, mentioned in sub-Section 4.3.1. The central wavelength and the averaged power were 1556 nm and 23 mW, respectively. First, the seed pulse was transmitted and chirped in a 1 m single-mode fiber (SMF). After power adjustment using a half-wave plate and a polarization beam splitter (PBS), the pulse was amplified in the normally-dispersive EDF. Four LDs operating at 980 nm were used for excitation, and the total maximum pump power was 1.2 W. The maximum power of the amplified soliton pulse was about 360 mW. Figure 4.10 shows the observed spectrum of the EDFA output. The spectrum of the ultrashort pulse was widened after amplification. Then, a PM fiber was used for soliton wavelength shift and ideal $sech^2$-shaped pulse generation. In PM fiber, a new Raman soliton pulse is formed gradually. Figure 4.11 shows the spectra of the PM fiber output, when the PM fiber input power was at the maximum amplified power. The seed pulse and the newly generated Raman soliton were both clearly observed at 1564 nm and 1635 nm, respectively. The spectrum of the generated soliton pulse is the ideal $sech^2$ shape. A long pass filter was used after the PM fiber to remove the seed pulse.

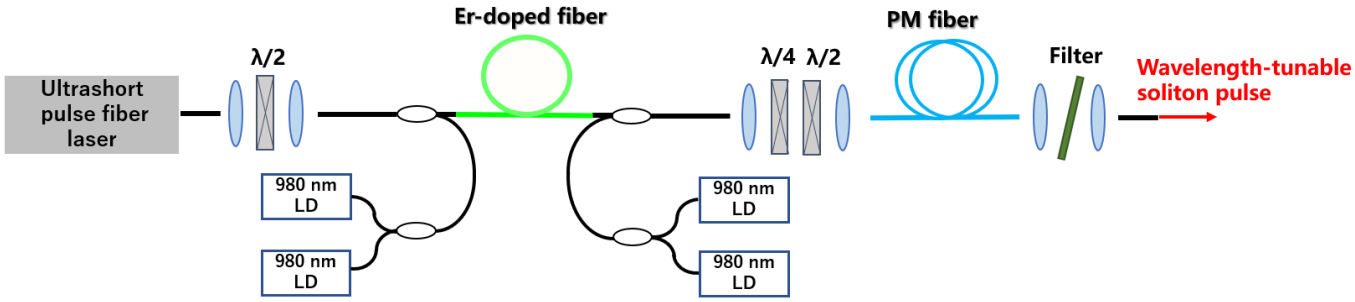

Fig. 4.9 Experiment setup for wavelength-tunable soliton pulse generation.

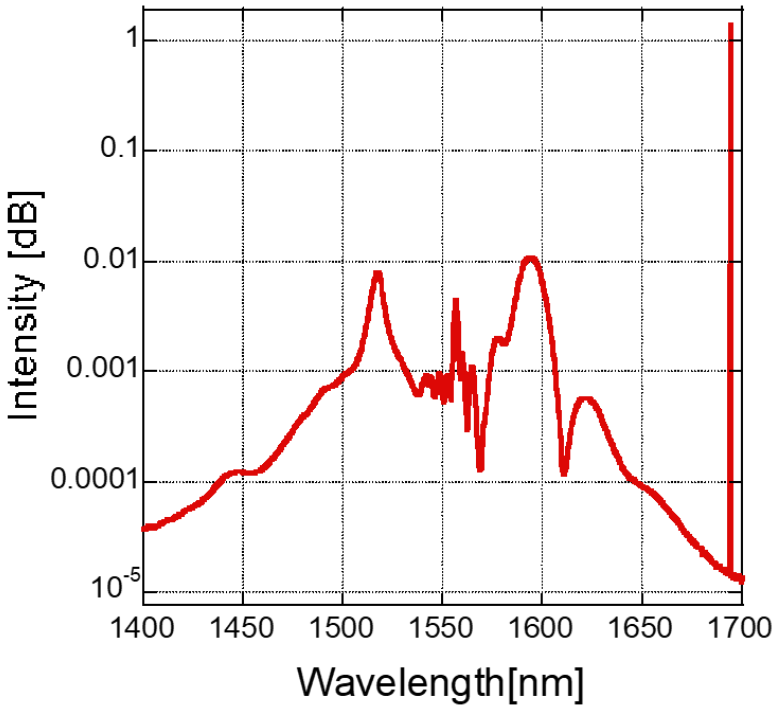

Fig. 4.10 Spectrum of EDFA output at the maximum of injection pump power.

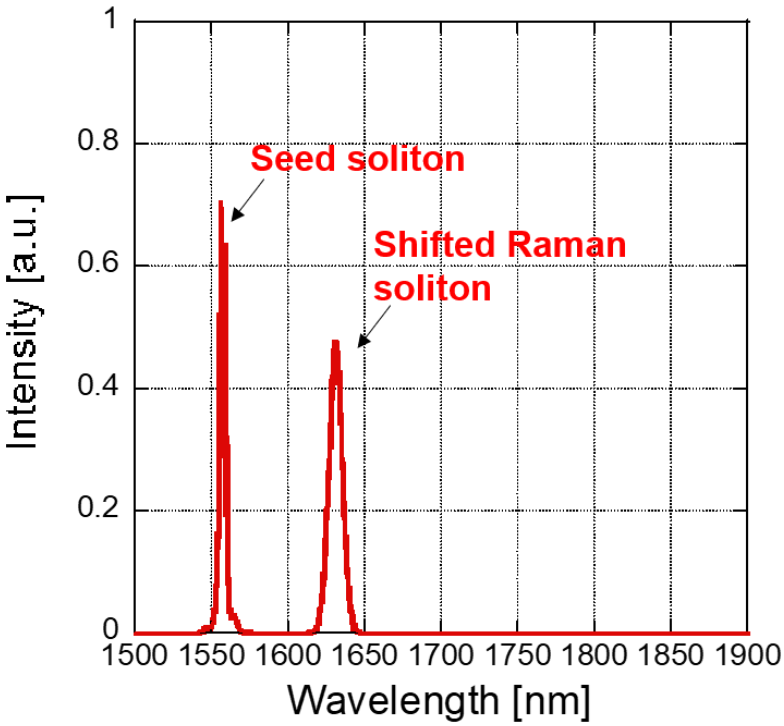

Fig. 4.11 Spectra of PM fiber output.

We varied the injection current of the Er-doped fiber amplifier (EDFA) to change the PM fiber input power to simulate intensity modulation. The wavelength-tunable soliton pulse generation was demonstrated. Figures 4.12(a) and 4.12(b) show the wavelength shift and output power of the Raman soliton as a function of the fiber-input power for fiber lengths of 100 and 300 m. As the fiber-input power was increased, the wavelength shift and output power increased almost linearly. These experimental results were close to the theoretical results and previously reported experimental results [32,33,45]. The 300 m fiber produced a longer wavelength shift than the 100 m fiber, but a reduced output power compared to the 100 m fiber. When the fiber length was 100 m, the maximum wavelength shift was 1835 nm with an output power of 97.5 mW. When the fiber length was 300 m, the maximum wavelength shift was increased up to 1930 nm, but it was accompanied by a second soliton pulse generation. For the subsequent quasi-SC generation, we had to adjust the polarization direction of the fiber input pulse to maintain single soliton generation. In this situation, the maximum wavelength shift was 1895 nm with an output power of 76.5 mW when the fiber length was 300 m.

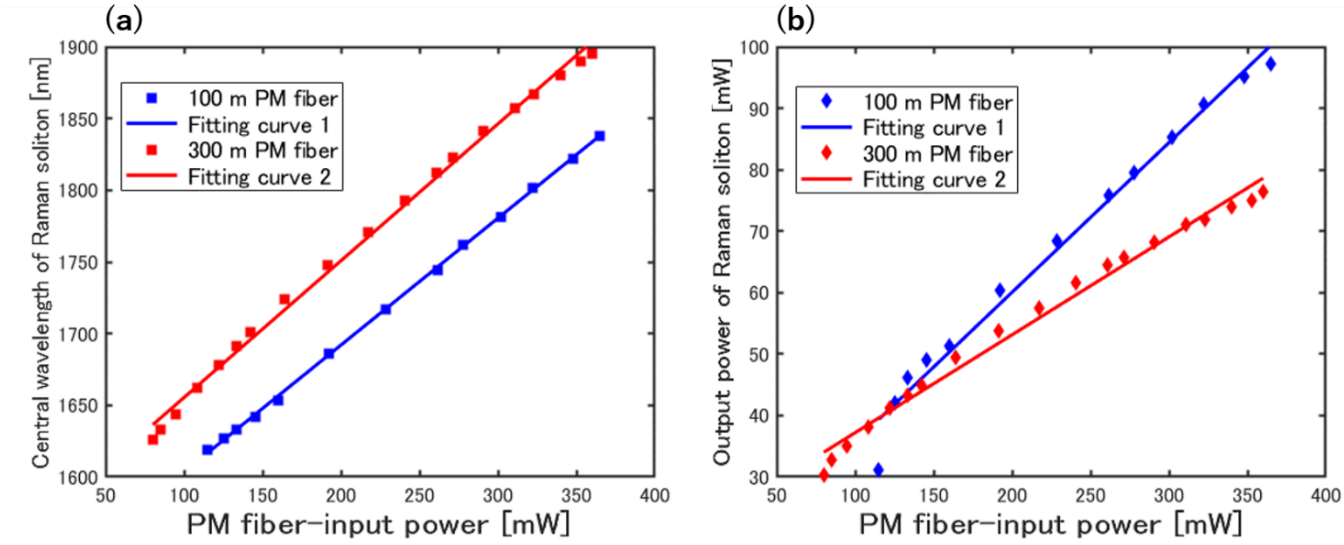

Fig. 4.12. (a) Wavelength shift and (b) output power of Raman soliton in terms of the fiber-input power for 100 m and 300 m fibers.

From the above examined results, the 300 m PM fiber is more suitable for subsequent quasi-SC generation because it allows a wider wavelength tuning range from 1600 nm to 1900 nm, although its averaged output power is lower than that of the 100 m fiber. In this study, we chose a 300 m PM fiber (SM15-PR-U24A-H) as the wavelength shift device.

4.3.3 Tunable Gaussian-like quasi-supercontinuum (SC) generation by fast intensity modulation

For the quasi-SC generation, we installed a fast intensity modulator between the seed pulse source and EDFA, replacing the manual adjustment of injection current described in Subsection 4.3.2 to achieve wavelength-tunable soliton generation. Figure 4.13 shows the experiment setup for Gaussian-shape quasi-SC generation. An electro-optical (EO) intensity modulator (Thorlabs LN81S-FC) and a programmable multifunction generator (NF WF1968) were used.

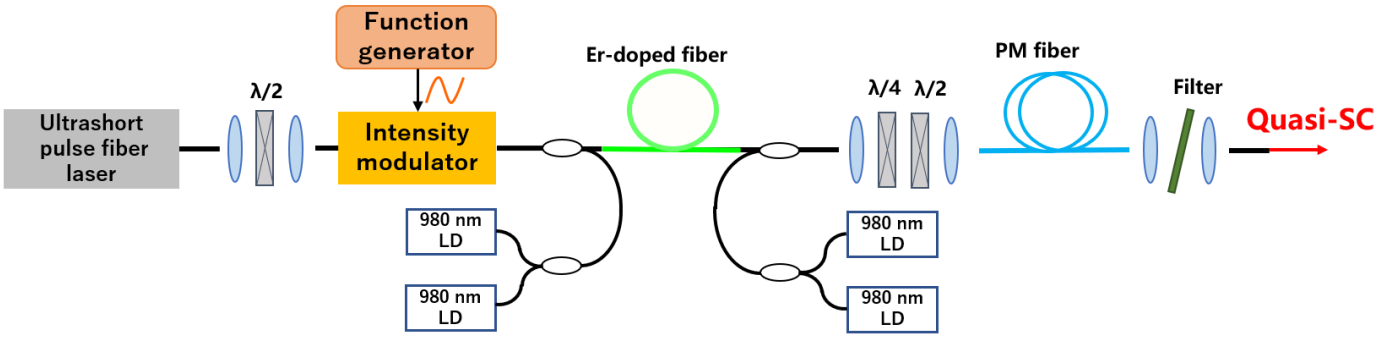

Fig. 4.13 Experiment setup for Gaussian-shape quasi-SC generation.

Figures 4.14 show the observed spectra with a simple linear intensity modulation at different modulation speeds. In the case of low-frequency modulation, shifted Raman solitons are generated one by one and the wavelength shift is linearly related to the modulation intensity in the wavelength range from 1600 nm to 1900 nm, as shown in Fig.4.14 (a). The pulse spectra kept the $sech^2$ shapes. The modulation frequency was 1 Hz. When the modulation frequency was higher than the sampling frequency of the detection system, the wavelength of the Raman soliton shifted continuously within one detection period, and the detected spectra was the superposition of these solitons and looked like a supercontinuum. For instance, when we increased the modulation frequency to 300 kHz beyond the 20 kHz detection rate of the spectrum analyzer (Yokogawa AQ6375), the shifted Raman solitons seemed to be generated at the same time, resulting in a detected spectrum that appeared to be super-continuous, as shown in Fig.4.14 (b), that is to say, a quasi-SC.

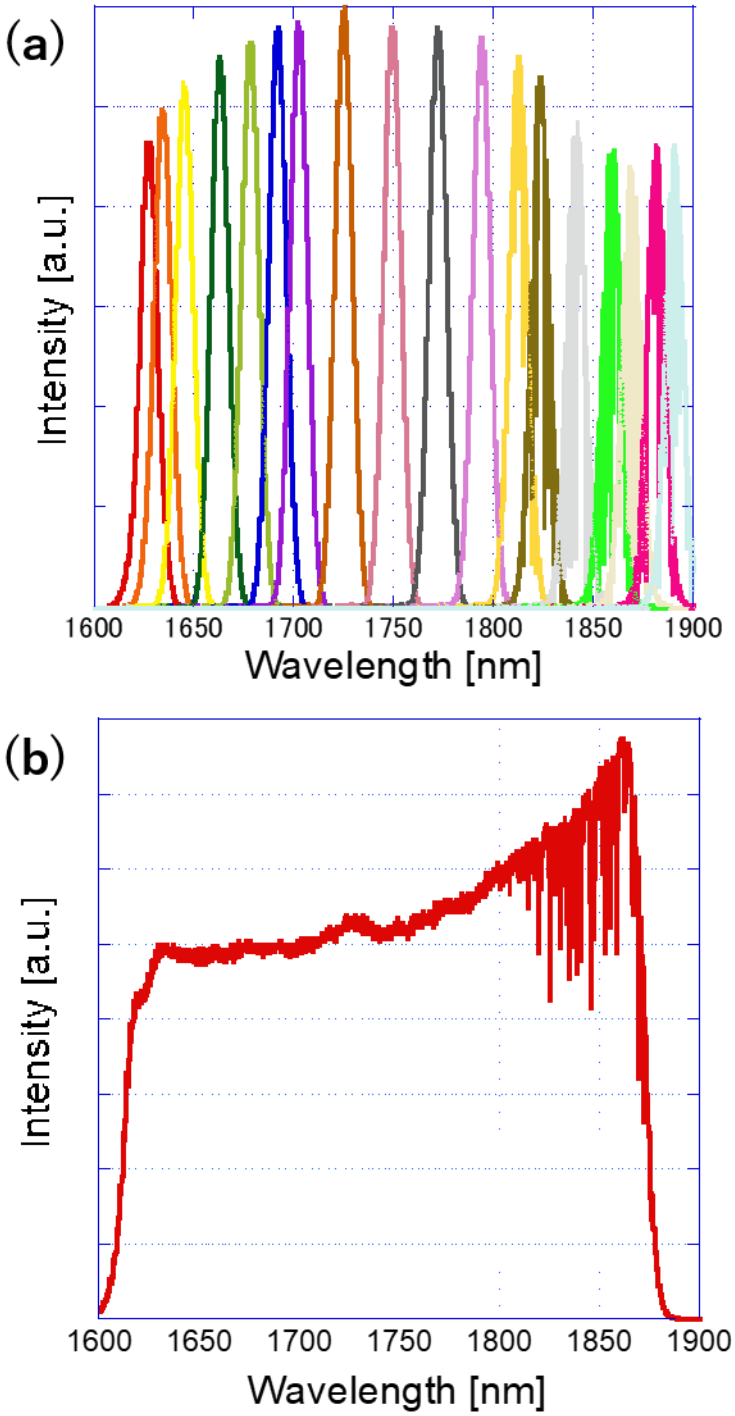

Fig. 4.14 Observed spectra using linear intensity modulation at (a) modulation frequency was 1 Hz and (a) modulation frequency was 300 KHz.

As mentioned in Chapter 2, the resolution of OCT is influenced by the spectral shape of the light source, and the desired spectrum for OCT would ideally manifest as a Gaussian spectral shape, resulting in a Gaussian

coherence function devoid of side lobes. In order to obtain a Gaussian-shaped spectrum, the design of the modulation function is important. The modulation function determines the shape of the quasi-SC by changing the wavelength tuning speed of the shifted Raman soliton pulse. By the model calculations, we designed the modulation function as shown in Fig.4.15 (a). The slope of the modulation function was set as gentle around the center wavelength, the larger number of Raman solitons were generated, and the integrated power of solitons was greater. On the other hand, at the shorter and longer wavelength ranges, the slope of the modulation function was set as steep, and the integrated power of solitons was smaller. We used the programable function in a multifunction generator (NF WF1968). The modulation amplitude and offset affected the central wavelength and bandwidth. By adjusting the amplitude and offset of the modulation function manually, a Gaussian-shaped quasi-SC spectrum with a bandwidth of 138 nm was generated at 1600-1900 nm spectral range, as shown in Fig. 4.15 (b).

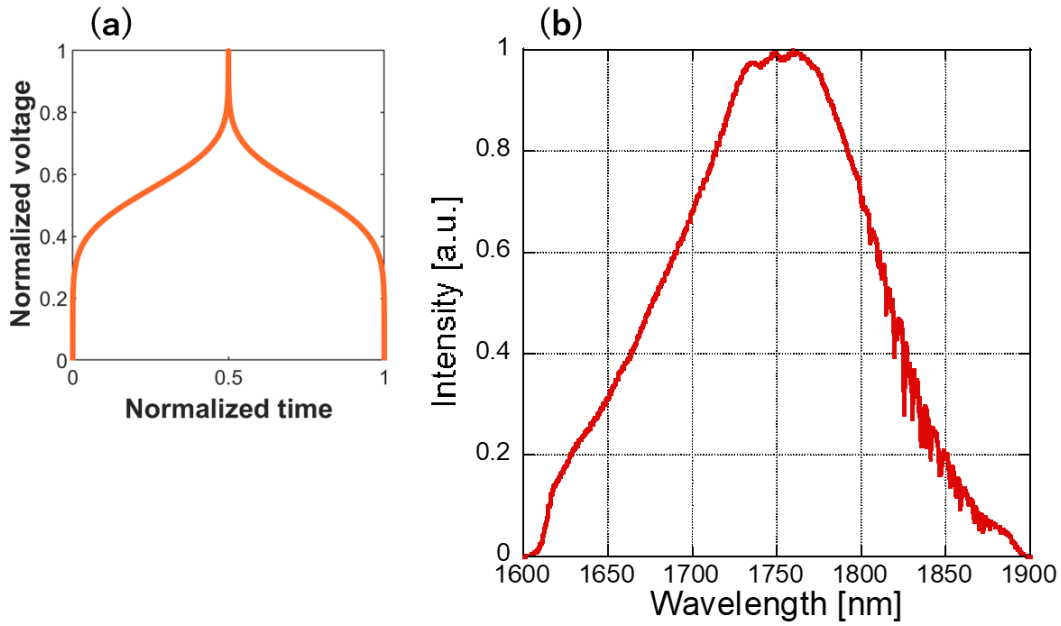

Fig. 4.15 (a) Intensity modulation function for Gaussian-shaped quasi-SC generation. (b) Spectra of broadband Gaussian-shaped quasi-SC output (λc = 1743 nm, $\Delta\lambda$ = 138 nm, output power = 51.2 mW, modulation frequency was about 300 kHz.).

4.4 Results

We investigated the characteristics of the quasi-SC from the developed laser. Figure 4.16 (a) shows the intensity-modulated Raman soliton pulse train forming quasi-SC observed by a fast pin photodiode (EOT ET-5000) and a digital oscilloscope (Yokogawa DL9040L). The soliton intensity modulation frequency was about 300 kHz, corresponding to 3.3 μs in the time domain. Figure 4.16 (b) shows the RF spectrum observed using the fast pin photodiode and an RF spectrum analyzer (Anritsu MS2830A). Equal-frequency-spanning RF spectra were observed, extending up to the 1 GHz range. The repetition rate measured approximately 95.5 MHz, corresponding to that of the seed fiber laser source. Figures 4.16(c) and 4.16(d) show the enlarged RF spectra of the fundamental frequency with 10 MHz and 500 kHz spectral range, respectively. We compared the RF spectra between the one of quasi-SC with modulation and the one of 1750 nm Raman soliton without

modulation. In quasi-SC generation, the fundamental soliton pulse was modulated with 300 kHz of frequency, as shown in Fig. 4.16(c). The noise level does not increase compared to Raman soliton generation, but there were some small modulation noise peaks, as shown in Fig. 4.16(d). It was considered that these spectral peaks were generated by intensity and phase modulation in the modulator.

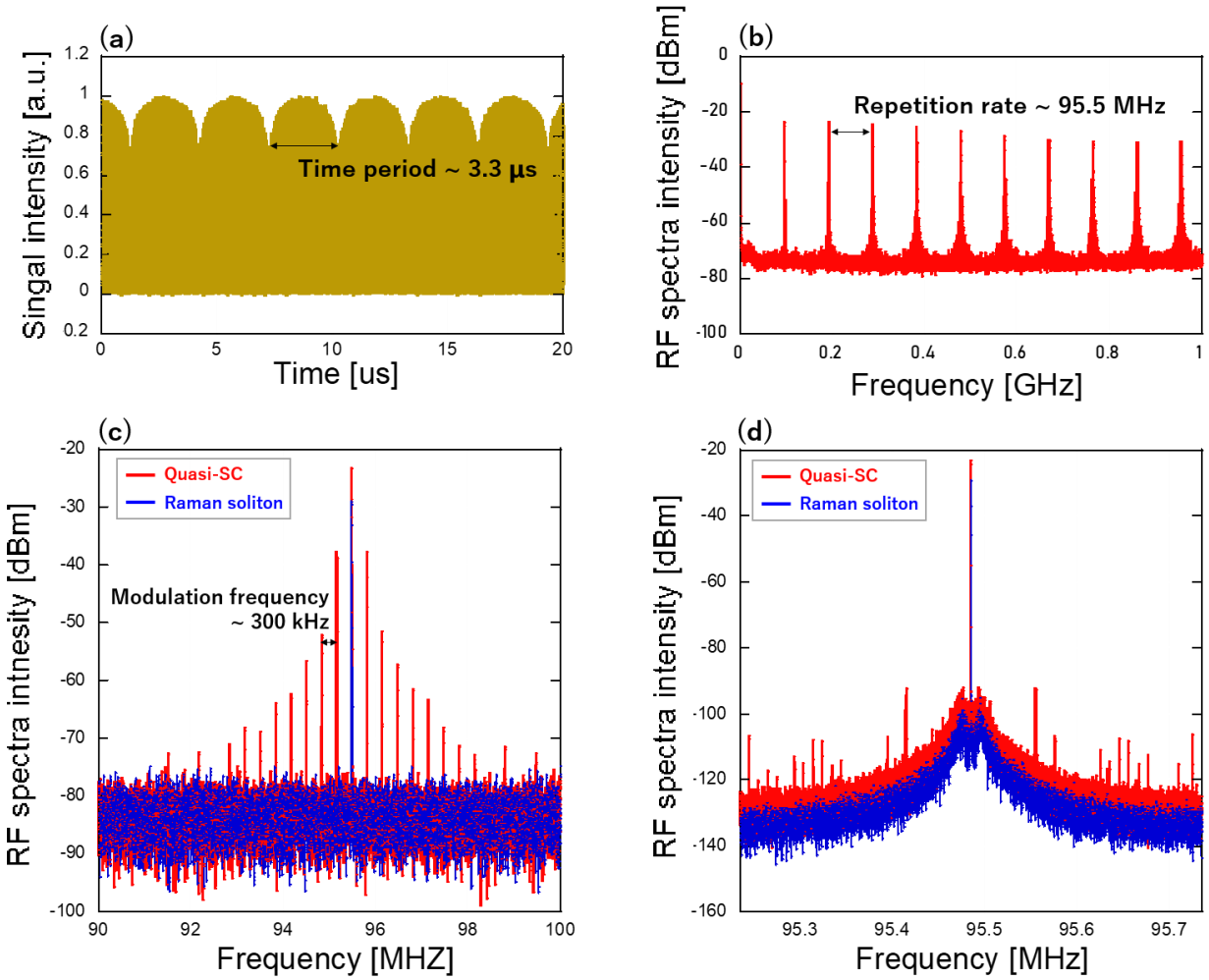

Fig. 4.16 (a) Intensity modulated Raman soliton pulse train forming quasi-SC, (b) RF spectra with 1GHz range, (c) enlarged RF spectra of the fundamental frequency with 10 MHz, (d) enlarged RF spectra of the fundamental frequency with 500 kHz.

We compared the results of quasi-SC with a 1700 nm conventional SC [46]. Figure 4.17 (a) shows the experiment setup for the 1700 nm conventional SC generation. The seed pulse was generated by a similar 1.5 µm ultrashort pulse fiber laser using SWNT, and amplified by EDFA. The use of PM fiber is to produce the $sech^2$-shaped soliton pulses with a central wavelength of 1700 nm. In this configuration, the soliton pulse was coupled into a highly nonlinear fiber (HNLF) for spectral broadening to obtain a SC. Figure 4.17 (b) shows the 1700 nm SC spectrum. The bandwidth and central wavelength were 1682 nm and 142 nm, respectively. The output power of conventional SC was 52.5 mW. Table 4.2 summarized the specifications for both quasi-SC source and SC source.

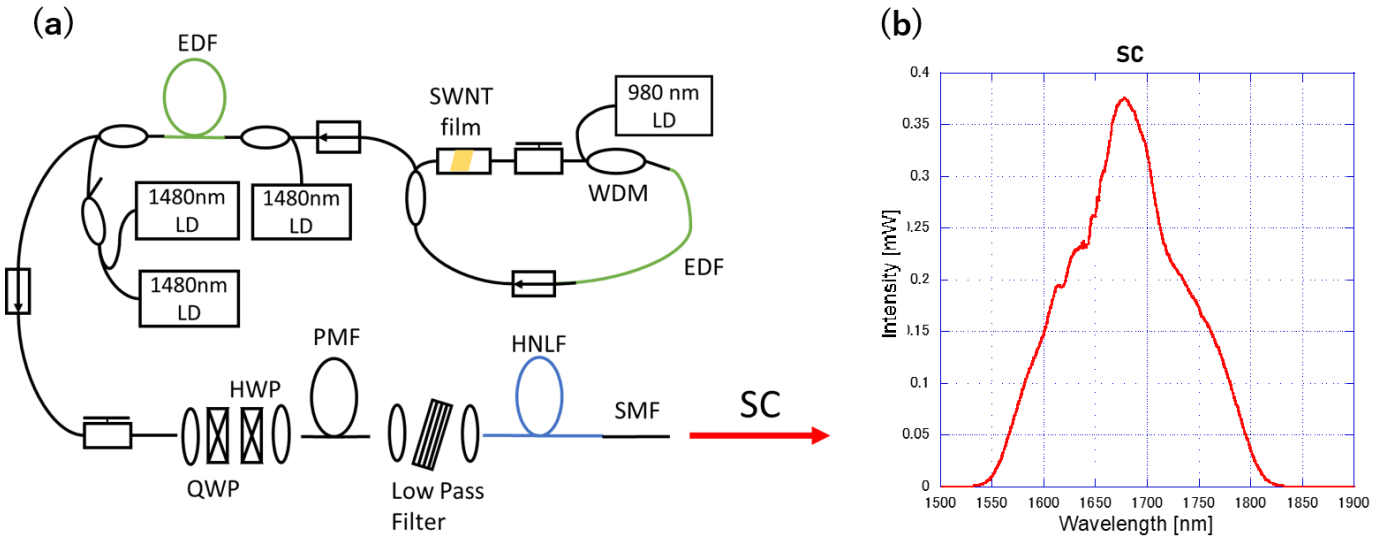

Fig. 4.17 (a) Experimental setup for 1700 nm conventional SC generation, (b) Spectra of SC output (λc = 1682 nm, $\Delta\lambda$ = 142 nm, output power = 52.5 mW.).

Table 4.2 Comparison of specifications for quasi-SC and SC.

	λc [nm]	$\Delta\lambda$ [nm]	Output power [mW]
Quasi-SC	1743	138	51.2
SC	1682	142	52.5

Figure 4.18 shows the RF spectra of the generated quasi-SC, Raman soliton, and the 1700 nm conventional SC developed by our group. We compared the spectra of the quasi-SC (with modulation), the 1750 nm Raman soliton (without modulation), and the 1700 nm conventional SC. In the quasi-SC generation, the fundamental soliton pulse was modulated with a frequency of 1.1 MHz. The noise level did not increase compared to Raman soliton generation and SC source below 100 kHz, but there were some small modulation noise peaks above that caused by intensity modulation.

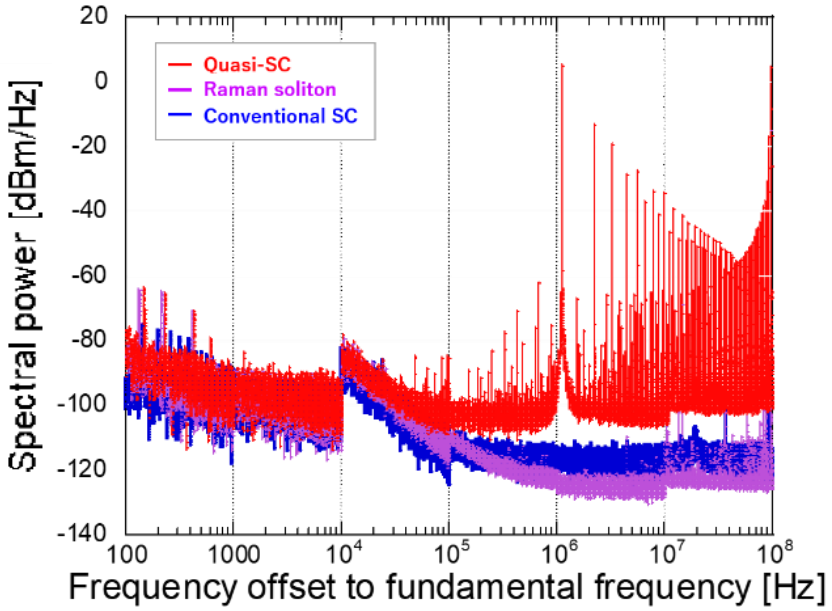

Fig. 4.18 RF noise spectra of quasi-SC, Raman soliton, and conventional SC.

4.5 Summary

In this chapter, the principle and development of a tunable quasi-supercontinuum generation at 1.7 μm spectral band have been demonstrated based on wavelength-tunable soliton pulse generation and fast intensity modulation. First, a 1.55 μm Er-doped ultrashort-pulse fiber laser using a SWNT polyimide film was used for seed pulse generation. The ultrashort pulse intensity was amplified to 360 mW of the maximum power by an EDFA to obtain a wider wavelength-tunable range from 1600 to 1900 nm. A fast intensity modulator has been inserted between the seed pulse source and EDFA to change PM fiber-input power continuously and rapidly. After a 300 m PM fiber, many newly shifted Raman solitons have been generated at almost the same time. The observed spectra seemed to be super-continuous. A quasi-SC with the bandwidths of 138 nm and the central wavelength of 1743 nm was obtained. We evaluated and compared the noise properties of quasi-SC, 1750 nm Raman soliton and 1700 nm conventional SC. The generated quasi-SC exhibited similar noise characteristics compared to 1750 nm Raman soliton and 1700 nm SC below 100 kHz.

Reference for Chapter 4

[1] W. Drexler, U. Morgner, F. X. Kartner, C. Pitris, S. A. Boppart, X. D. Li, E. P. Ippen, and J. G. Fujimoto, "In vivo ultrahigh-resolution optical coherence tomography," *Opt. Lett.* **24**(17), 1221–1223 (1999).

[2] I. Hartl, X. D. Li, C. Chudoba, R. K. Ghanta, T. H. Ko, J. G. Fujimoto, J. K. Ranka and R. S. Windeler, "Ultrahigh-resolution optical coherence tomography using continuum generation in an air–silica microstructure optical fiber," *Opt. Lett.* **26**(9), 608–610 (2001).

[3] W. Drexler, U. Morgner, R. K. Ghanta, F. X. Kartner, J. S. Schuman, and J. G. Fujimoto, "Ultrahigh-resolution ophthalmic optical coherence tomography," *Nat. Med.* **7**(4), 502–507 (2001).

[4] B. Povazay, K. Bizheva, A. Unterhuber, B. Hermann, H. Sattmann, A. F. Fercher, W. Drexler, A. Apolonski, W. J. Wadsworth, J. C. Knight, P. St. J. Russell, M. Vetterlein and E. Scherzer, "Submicrometer axial resolution optical coherence tomography," *Opt. Lett. 27*(20), 1800–1802 (2002).

[5] MT Tsai, JJ Hung, and MC Chan, "Ultrahigh-Resolution Optical Coherence Tomography with LED-Phosphor-Based Broadband Light Source," *Appl. Phys. Express* **6**, 122502 (2013).

[6] M. Nishiura, T. Kobayashi, M. Adachi, J. Nakanishi, T. Ueno, Y. Ito, and N. Nishizawa, "In vivo Ultrahigh-Resolution Ophthalmic Optical Coherence Tomography Using GaussianShaped Supercontinuum," *Jpn. J. Appl. Phys.* **49**, 012701 (2010).

[7] R. Weissleder, "A clearer vision for in vivo imaging," *Nat. Biotechnol.* **19**, 316–317 (2001).

[8] V. J. Pansare, S. Hejazi, W. J. Faenza, and R. K. Prudhomme, "Review of LongWavelength Optical and NIR Imaging Materials: Contrast Agents, Fluorophores, and Multifunctional Nano Carriers," *Chem. Mater.* **24**, 812–827 (2012).

[9] T. Jin, "Non-Invasice Near-Infrared Fluorescence Imaging in the Second Optical Window," *JJSLSM* **36**(2), 194.200 (2015).

[10] K. K. Tsia, "Essential Basics of Light-Matter Interaction in Biophotonics," Chap. 2 in Understanding Biophotonics, Fundamentals, Advances, and Applications, L. L. Tsia, Ed., 4.7–198, Pan Stanford (2015).

[11] R. R. Anderson and J. A. Parrish, "The Optics of Human Skin," *J. Invest. Dermatol.* **77**, 13–19 (1981).

[12] A. Abdo and M. Sahin, "NIR Light Penetration Depth in the Rat Peripheral Nerve and Brain Cortex," Proc. 29th Annual International Conference of the IEEE EMBS, 1723–1725 (2007).

[13] N. Chen, CH Wong, and C. J. R. Sheppard, "Focal modulation microscopy," *Opt. Express* **16**(23), 18764–18769 (2008).

[14] G. M. Palmer, K. Vishwanath, and M. W. Dewhirst, "Application of Optical Imaging and Spectroscopy to Radiation Biology," *Radiat. Res.* **177**(4), 364.375 (2012).

[15] M. Mehrmohammadi, S. J. Yoon, D. Yeager, and S. Y. Emelianov, "Photoacoustic Imaging for Cancer Detection and Staging," *Curr. Mol. Imaging* **2**(1), 89–105 (2013).

[16] L. A. Sordillo, Y. Pu, S. Pratavieira, Y. Budansky, and R. R. Alfano, "Deep optical imaging of tissue using the second and third near-infrared spectral windows," *J. Biomed. Opt.* **19**(5), 04.6004 (2014).

[17] V. V. Tuchin, "Tissue Optics and Photonics: Light-Tissue Interaction," J. *Biomed. Photonics Eng.* **1**(2), 98–134 (2015). 38

[18] S. L Jacques, “Optical properties of biological tissues: a review,” *Phys. Med. Biol.* **4.8**, R37–R61 (2013).

[19] M. H. Niemz, Laser-Tissue Interactions, Fundamentals and Applications, Springer (2003).

[20] L. Shi, L. A. Sordillo, A. Rodríguez-Contreras, and R. Alfano, “Transmission in near-infrared optical windows for deep brain imaging,”*Journal of biophotonics*, ***9***(1-2), 38-43 (2016).

[21] Y. Wang, Y. Zhao, J. S. Nelson, Z. Chen, and R. S.Windeler, "Ultrahigh-resolution optical coherence tomography by broadband continuum generation from a photonic crystal fiber" *Opt. Lett.* **28**(3), 182-184 (2003).

[22] A. Unterhuber, B. Považay, K. Bizheva, B. Hermann, H. Sattmann, A. Stingl, and W. Drexler, "Advances in broad bandwidth light sources for ultrahigh resolution optical coherence tomography," *Phys. Med. Biol.*, **49**(7), 1235(2004).

[23] N. Nishizawa, Y. Chen, P. Hsiung, E. P. Ippen, and J. G. Fujimoto, "Real-time, ultrahigh-resolution, optical coherence tomography with an all-fiber, femtosecond fiber laser continuum at 1.5 μm," *Opt. Lett.* **29**(24), 2846-2848 (2004).

[24] H. Kawagoe, S. Ishida, M. Aramaki, Y. Sakakibara, E. Omoda, H. Kataura, and N. Nishizawa, "Development of a high-power supercontinuum source in the 1.7 μm wavelength region for highly penetrative ultrahigh-resolution optical coherence tomography, " *Biomed Opt. Express* **5**(3), 932-943 (2014).

[25] T. Hori, J. Takayanagi, N. Nishizawa, and T. Goto, "Flatly broadened, wideband and low noise supercontinuum generation in highly nonlinear hybrid fiber," *Opt. Express* **12**(2), 317-324 (2004).

[26] N. Nishizawa, and J. Takayanagi, "Octave spanning high-quality supercontinuum generation in all-fiber system," *J. Opt. Soc. Am.* B **24**(8), 1786-1792 (2007).

[27] S. Bourquin, A. D. Aguirre, I. Hartl, P. Hsiung, T. H. Ko, J. G. Fujimoto, and D. Kopf, "Ultrahigh resolution real time OCT imaging using a compact femtosecond Nd: Glass laser and nonlinear fiber," *Opt. Express* 11(24), 3290-3297 (2003).

[28] B. E. Bouma, G. J. Tearney, I. P. Bilinsky, B. Golubovic, and J. G. Fujimoto, "Self-phase-modulated Kerr-lens mode-locked Cr: forsterite laser source for optical coherence tomography," *Opt. Lett.* **21**(22) ,1839-1841 (1996).

[29] Y. Wang, Y. Zhao, J. S. Nelson, Z. Chen, and R. S. Windeler, "Ultrahigh-resolution OCT using broadband continuum generation from a photonic crystal fiber," *Opt. Lett.* **28**(3), 182-184 (2003).

[30] K. Sumimura, T. Ohta, and N. Nishizawa, "Quasi-super-continuum generation using ultrahigh-speed wavelength-tunable soliton pulses," *Opt. Lett.* **33**(24), 2892-2894 (2008).

[31] K. Sumimura, T. Ohta, and N. Nishizawa, "Quasi-supercontinuum generation using 1.06 μm ultrashort-pulse laser system for ultrahigh-resolution optical-coherence tomography," *Opt. Lett.* **35**(21), 3631-3633 (2010).

[32] N. Nishizawa, and T. Goto, "Compact system of wavelength-tunable femtosecond soliton pulse generation using optical fibers," *IEEE Photon. Technol.* **11**(3), 324.327 (1999).

[33] N. Nishizawa, R. Okamura, and T. Goto, "Analysis of widely wavelength tunable femtosecond soliton pulse generation using optical fibers," *Jpn. J. Appl. Phys.* **38** (8R), 4768(1999).

[34] D. J. Richardson, R. I. Laming, D. N. Payne, M. W. Phillips, and V. J. Matsas, “320 fs soliton generation with passively mode-locked erbium fiber laser,” *Electron. Lett.*, **27**(9), 730–732, (1991).

[35] M. Nakazawa, E. Yoshida, and Y. Kimura, “Generation of 98 fs optical pulses directly from an erbium-doped fiber ring laser at 1.4.7 um,” *Electron. Lett.*, **29**(1), 63–65, (1993).

[36] K. Tamura, E. P. Ippen, H. A. Haus, and L. E. Nelson, “77 fs pulse generation from a stretched-pulse mode-locked all-fiber ring laser,” *Opt. Lett.*, **18**(13), 1080–1082, (1993).

[37] W. H. Loh, D. Atkinson, P. R. Morkel, M. Hopkinson, A. Rivers, A. J. Seeds, and D. N. Payne, “All-solid-state subpicosecond passively modelocked erbium-doped fiber laser,” *Appl. Phys. Lett.*, **63**(1), 4–6, (1993).

[38] S. Yamashita, Y. Inoue, S. Maruyama, Y. Murakami, H. Yaguchi, M. Jablonski, and S. Y. Set, “Saturable absorbers incorporating carbon nanotubes directly synthesized onto substrates and fibers and their application to mode-locked fiber lasers,” *Opt. Lett.* **29** (14)**,** 14.81-14.83 (2004).

[39] A. G. Rozhin, Y. Sakakibara, S. Namiki, M. Tokumoto, H. Kataura, and Y. Achiba, “Sub-200-fs pulsed erbium-doped fiber laser using a carbon nanotube-polyvinylalcohol mode locker,” *Appl. Phys. Lett.* **88** (5), 04.1118 (2006).

[40] M. Nakazawa, S. Nakahara, T. Hirooka, M. Yoshida, T. Kaino, and K. Komatsu, “Polymer saturable absorber materials in the 1.5 um band using poly-methyl-methacrylate and polystyrene with single-wall carbon nanotubes and their application to a femtosecond laser,” *Opt. Lett.* **31** (7), 915-917 (2006).

[41] Y. W. Song, S. Yamashita, C. S. Goh, and S. Y. Set, “Carbon nanotube mode lockers with enhanced nonlinearity via evanescent field interaction in D-shaped fibers,” *Opt. Lett.* **32** (2), 148-150 (2007).

[42] J. W. Nicholson, R. S. Windeler, and D. J. DiGiovanni, “Optically driven deposition of single-wall carbonnanotube saturable absorbers on optical fiber end-faces,” *Opt. Express* **15** (15), 9176-9183 (2007).

[43] K. Kieu and M. Mansuripur, “Femtosecond laser pulse generation with a fiber taper embedded in carbon nanotube/polymer composite,” *Opt. Lett.* **32**(15), 2242-2244 (2007).

[44] Y. W. Song, S. Yamashita, and S. Maruyama, “Single-walled carbon nanotubes for high-energy optical pulse formation,” *Appl. Phys. Lett.* **92**(2), 021115 (2008).

[45] N. Nishizawa, Y. Seno, K. Sumimura, Y. Sakakibara, E. Itoga, H. Kataura, and K. Itoh, "All-polarization-maintaining Er-doped ultrashort-pulse fiber laser using carbon nanotube saturable absorber," *Opt. Express* **16**(13), 9429-9435 (2008).

[46] H. Kawagoe, M. Yamanaka, S. Makita, Y. Yasuno, and N. Nishizawa, "Full-range ultrahigh-resolution spectral-domain optical coherence tomography in 1.7 μm wavelength region for deep-penetration and high-resolution imaging of turbid tissues," *Appl. Phys. Express* **9**(12), 127002 (2016).

Chapter 5 High resolution and larger penetration depth imaging using 1.7 μm broadband quasi-supercontinuum (SC)

5.1 Introduction

In Chapter 4, the tunable quasi-supercontinuum laser source at 1.7 μm spectral band has been developed based on wavelength-tunable soliton pulse generation and fast intensity modulation. As described in sub-Section 4.3, the generated quasi-SC has the tunability in terms of spectral shape, wavelength range and bandwidth. This property makes it possible for high-resolution OCT imaging with large penetration depth, and its adjustable wavelength and bandwidth provide the potential for the optimization of OCT imaging performance. Therefore, it is worth to investigate the OCT imaging using the developed tunable quasi-supercontinuum laser source.

As mentioned in Chapter 2, there are three common OCT systems: SS-OCT, TD-OCT, and SD-OCT. They are widely used for biomedical imaging. SS-OCT requires a spectrally tunable laser light source, which is capable of rapid scanning across the spectral range. The developed quasi-supercontinuum laser source, whose output spectra look like SC, is not suitable for SS-OCT.

Studies on SD-OCT have demonstrated the achievement of a maximum imaging depth of 1.7 mm with an impressive axial resolution of 3.6 μm in mouse brain imaging using the 1.7 μm SC source [1]. The report on the generation of high-power coherent SC contributes TD-OCT imaging with improved imaging capabilities, offering an enhanced imaging depth of 1.9 mm in the biological sample of pig thyroid gland with an axial resolution of 3.2 μm [2].

Theoretically, SC sources are often better suited for SD-OCT over TD-OCT, because of their simultaneous provision of a broad spectrum, high repetition rate, and capacity for wavelength tuning. In SD-OCT, which relies on a single interferogram for depth information, SC sources offer advantages in terms of imaging speed, improved depth resolution, and enhanced signal-to-noise ratio [3,4]. Quasi-SC has similar spectral properties to SC, so it is desirable to investigate whether SD-OCT using quasi-SC can achieve the same imaging performance.

In addition, Sumimura *et al.* have reported 1.3 μm quasi-SC generation for TD-OCT imaging [5]. They have investigated the performance of TD-OCT imaging with the tunability of quasi-SC. To our knowledge, there have been no reports on SD-OCT imaging using quasi-SC source. It is necessary to investigate the performance of SD-OCT imaging with the tunability of quasi-SC.

In this Chapter, we demonstrated highly sensitive, high-resolution SD-OCT imaging with large penetration depth using the developed quasi-SC source. In Section 5.2, a 1.7 μm Gaussain-shaped broadband quasi-SC was generated, and the experimental setup of SD-OCT was described. In Section 5.3, the characteristics of imaging using quasi-SC were evaluated, including the sensitivity, spatial resolution, and imaging depth. In Section 5.4, we successfully obtained high-resolution deep tissue cross-sectional images of tape stack, pig thyroid, human fingertip, and human teeth samples. We also compared the imaging results obtained by the developed quasi-SC and the conventional SC source. In Section 5.5, we briefly discussed the reasons for the slight difference in imaging characteristic parameters between quasi-SC and conventional SC. Finally, a summary was given about the SD-OCT imaging using a 1.7 um broadband quasi-SC.

5.2 Broadband quasi-supercontinuum (SC) generation and experimental setup for SD-OCT

In Chapter 4.2, the experimental setup for Gaussian-shaped quasi-SC generation at 1.7 μm spectral band has been developed. The generated quasi-SC has the tunability because of adjustable intensity modulation. The modulation amplitude and offset affect the central wavelength and bandwidth. For high-resolution deep tissue imaging, a 1.7 μm Gaussian-shaped quasi-SC spectrum with a broad bandwidth of 138 nm was generated by adjusting the amplitude and offset of the modulation function manually, as shown in Fig.5.1. It was centered at 1743 nm with an output power of 51.2 mW.

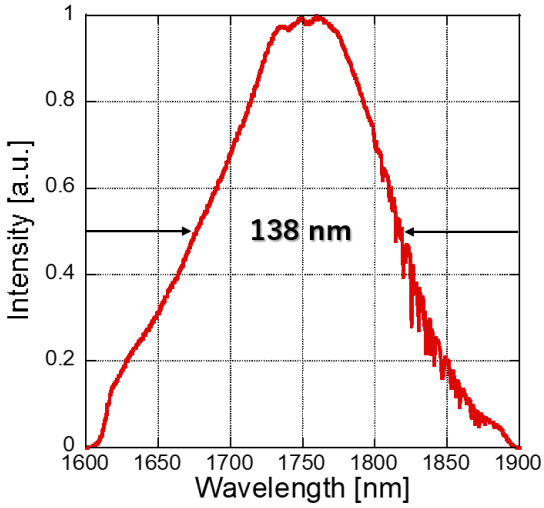

Fig. 5.1 Spectra of broadened Gaussian-shaped quasi-SC output (λc = 1743 nm, Δλ = 138 nm, output power = 51.2 mW, modulation frequency was about 300 kHz.).

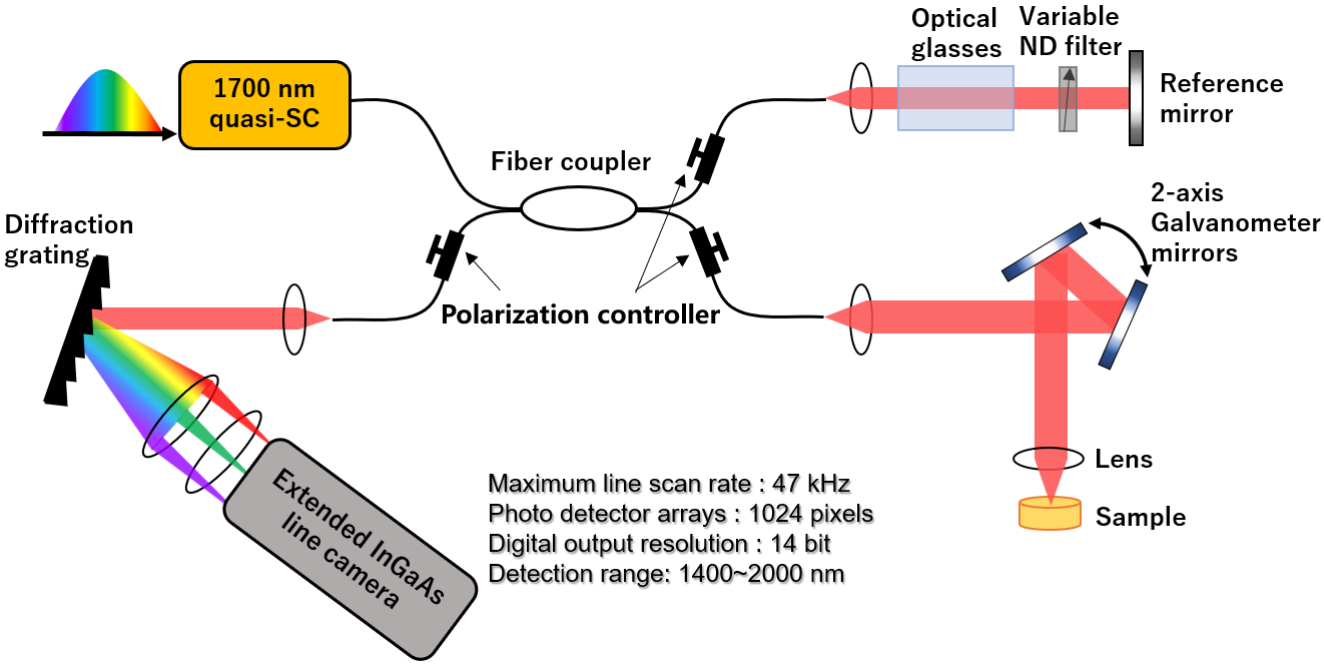

Fig. 5.2 Experimental setup for SD-OCT using 1.7 μm quasi-SC laser source.

We applied the above 1.7 μm broadband quasi-SC to SD-OCT. Figure 5.2 shows the experiment setup of SD-OCT. The whole system included the light source, reference arm, sample arm, and detection part, was connected by a 50/50 fiber coupler [1]. The sample arm consisted of XY-axis galvanometer scanners to obtain a cross-sectional or volumetric image, and a focusing lens with a focal length of 30 mm. In the reference arm, dispersion-compensating glass plates were incorporated to align the dispersions of the two arms. Additionally, a variable neutral density (ND) filter was introduced to control the reference beam power to avoid the saturation of line camera and optimize the measurement sensitivity. Polarization controllers were also introduced to remove polarization mismatches. In the 50/50 fiber coupler, the output light from the quasi-SC source was divided into the reference arm and sample arm, and the reflected light from the sample and reference mirror interfered with each other. To detect the interference signal, we used a custom-built spectrometer composed of a 150 lines/mm blazed diffraction grating (Shimadzu 015-200), two focusing achromatic lenses and a 47k lines/s InGaAs line scan camera (Goodrich SU1024LDH-2.2RT-0250/LC). The camera has an extended detection wavelength range from 1400 nm to 2000 nm. The pixel number and digital output resolution were 1024 pixels and 14 bits, respectively.

5.3 Characteristics of SD-OCT imaging

To evaluate the performance and quality of SD-OCT imaging using 1.7 μm broadband quasi-SC, we have examined the characteristics in terms of the imaging sensitivity, axial resolution, lateral resolution, and imaging depth. For reference and comparison, we also examined the characteristics of OCT imaging using 1.7 μm conventional SC light source, which has similar output spectra to the quasi-SC. The experiment setup and specifications for 1.7 μm SC generation have been described in Subsection 4.4. The bandwidth and central wavelength of SC were 1682 nm and 142 nm, respectively. The output power was 52.5 mW.

5.3.1 Imaging sensitivity and axial resolution

We examined the system sensitivity and axial resolution using a reflective mirror as a sample. The incident power of the OCT system from quasi-SC was 45.8 mW, and the incident power on the sample was 7.6 mW. Figure 5.3 (a) shows the cross-sectional image for the sample of a reflective mirror, and the interference signal is shown in Fig.5.3 (b). The total system sensitivity was 98 dB, including 59 dB signal power and a 39 dB round-trip attenuation. The maximum axial resolution was the path length difference width at 6 dB attenuation of signal power. The examined value was 14.8 μm in air, corresponding to 10.7 μm in biological tissues. The calculation of theoretical values has been given by Eq. (2.7) as described in Chapter 2. The theoretical values were 13.4 μm in air and 9.7 μm in tissue, respectively. They were close to the theoretical values of 13.4 μm in air and 9.7 μm in tissue, respectively. The experimental values are close to theoretical values.

We also examined the imaging sensitivity and axial resolution by 1.7 μm SC source in the same way. The incident power from SC source was 42.1 mW. The total system sensitivity was 97 dB. The examined values of axial resolution were 12.3 μm in air and 8.9 μm in tissues. Table 5.1 summarizes the imaging sensitivity and axial resolution for both quasi-SC and SC. The quasi-SC and SC source have similar imaging sensitivity and axial resolution.

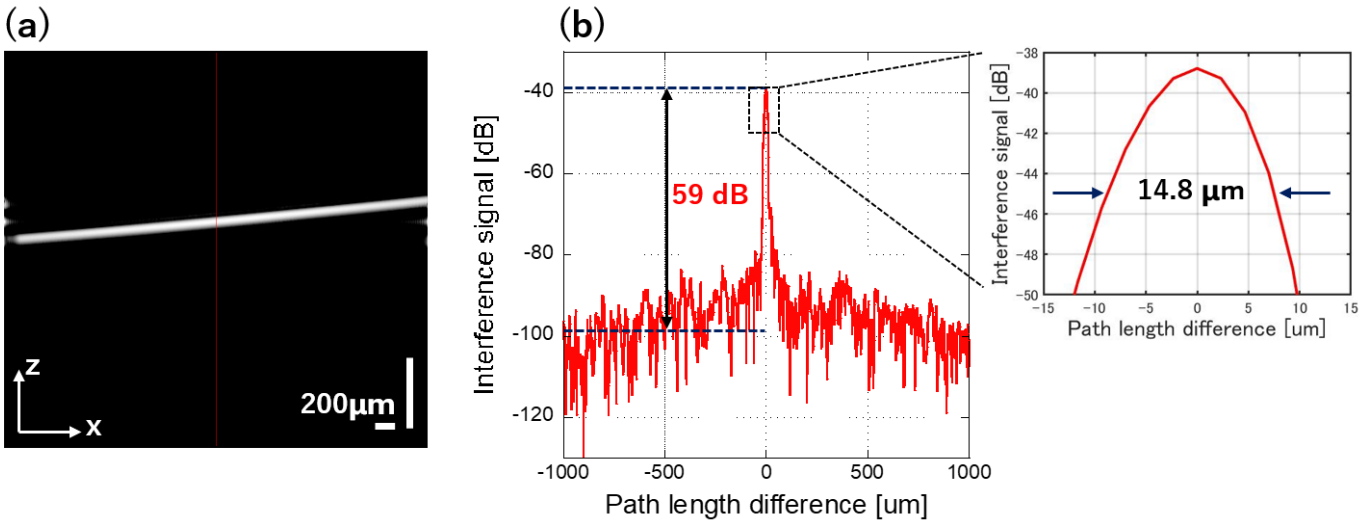

Fig. 5.3 (a) Cross-sectional OCT image of a reflective mirror and (b) interference signal of OCT using 1.7 um broadband quasi-SC.

Table 5.1 Comparison of imaging sensitivity and axial resolution for quasi-SC and SC

	Specifications of light source		Characteristics of OCT imaging		
	λc [nm]	Δλ [nm]	Incident power [mW]	Sensitivity [dB]	Axial resolution (in air / in tissue) [μm]
Quasi-SC	1743	138	45.8	98	14.8 / 10.7
SC	1682	142	42.1	97	12.3 / 8.9

Next, we investigated the imaging sensitivity and axial resolution with the tunable quasi-SC. Figure 5.4 shows the imaging sensitivity and axial resolution in terms of tunable modulation frequency. To achieve effective OCT imaging, we have to set the modulation frequency to more than 100 kHz because the scanning speed of the detection camera was 47k lines/s. We varied the modulation frequency from 100 kHz to 10 MHz. The imaging sensitivity and axial resolution remained stable with tunable modulation frequency. This result, indicating that the SD-OCT was not sensitive to the modulation frequency, was similar to TD-OCT for modulation frequencies beyond several hundred kHz [3]. When the modulation frequency was sufficiently higher than the scanning rate of the line camera, the OCT imaging characteristics were stable.

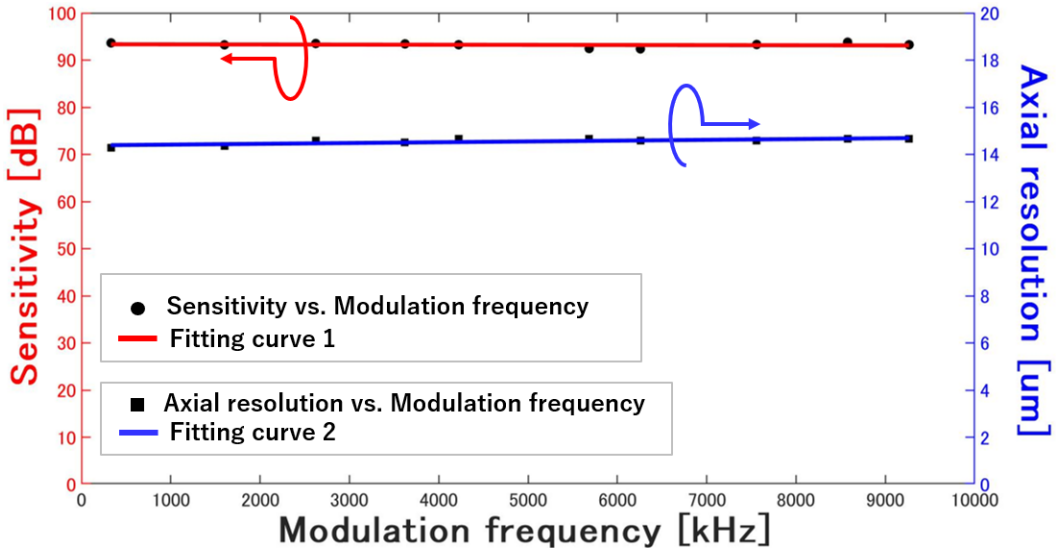

Fig. 5.4 Imaging sensitivity and axial resolution in terms of modulation frequency

Figure 5.5(a) shows generated quasi-SC spectra with tunable bandwidth. The bandwidths were tunable from 46 nm to 138 nm by adjusting the amplitude and offset of the modulation function. The spectra were all centered at around 1750 nm. Figure 5.5(b) shows the imaging sensitivity and axial resolution in terms of tunable quasi-SC bandwidth. The imaging sensitivity was almost constant, but the axial resolution was improved as the bandwidth was increased, and this result was in good agreement with the theoretical value.

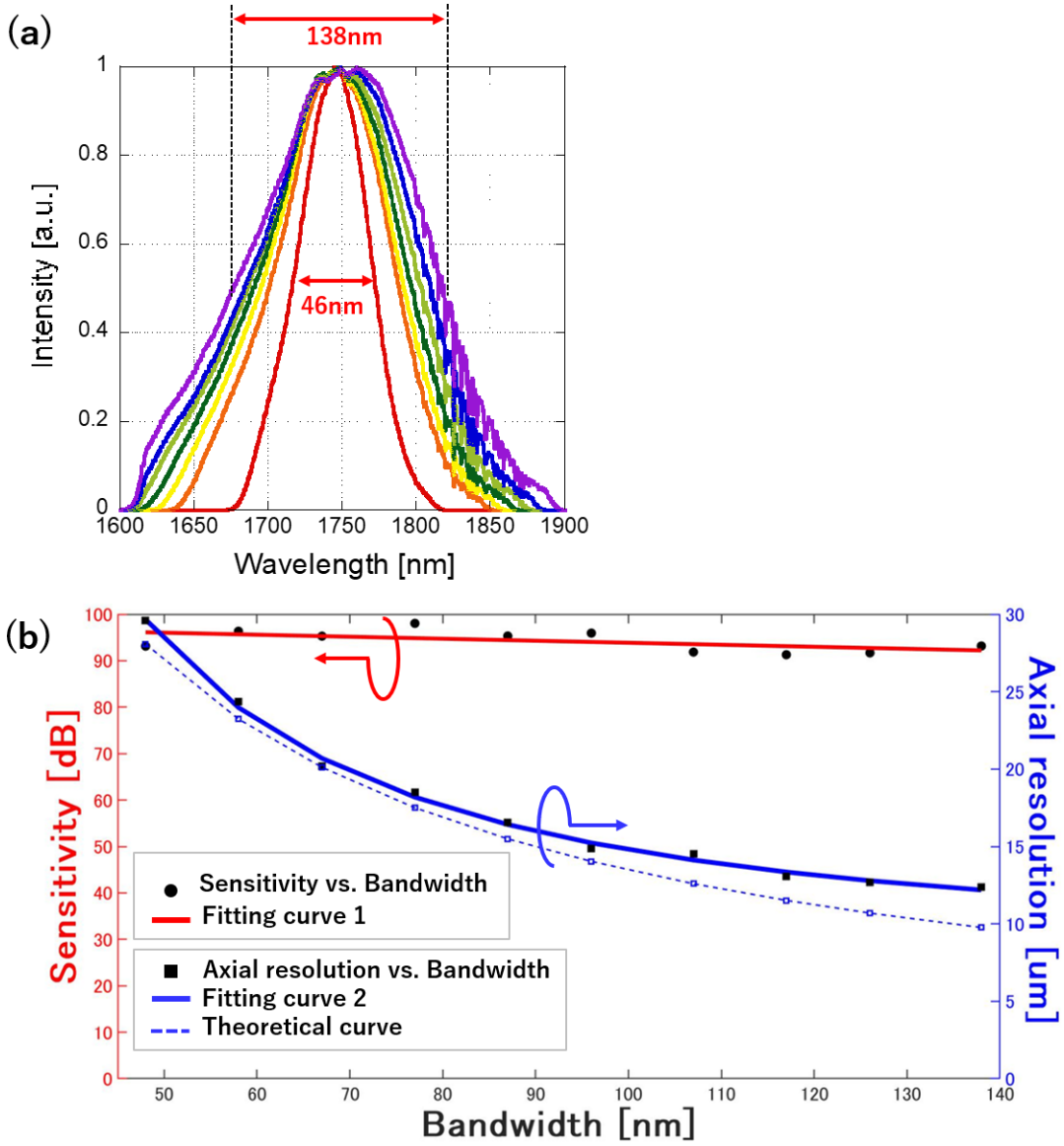

Fig. 5.5 (a) Generated Gaussian-shaped quasi-SC spectra with tunable bandwidth. (b) Imaging sensitivity and axial resolution in terms of tunable bandwidth of quasi-SC at a modulation frequency of 300 kHz.

From the above results, the broadband quasi-SC and SC have similar characteristics in terms of imaging sensitivity and axial resolution. The tunability of the quasi-SC source did not damage the sensitivity and axial resolution. The OCT imaging characteristics kept stable when the modulation frequency was tunable from 100 kHz to 10 MHz. The imaging sensitivity was almost unchanged with the tunable bandwidth of quasi-SC, and the effect of variable bandwidth on resolution was also consistent with theoretical analysis.

5.3.2 Lateral resolution

We used a resolution target card for the examination of lateral resolution for OCT imaging by the 1.7 μm broadband quasi-SC. This examination consists of three steps: performing the imaging in the region of interest

with the resolution target card, measuring the lateral pixel size, and calculating the lateral resolution by edge profile method.

Figure 5.6 (a) shows the resolution target card (USAF 1951 1X, Thorlabs) as a sample for imaging. We chose the area of Group 0- Element 1 as the region of interest, which corresponds to the resolution of 1 mm/ line pairs. Figure 5.6(b) shows the cross-sectional image of line pairs as the region of interest. A pair of lines is able to be observed clearly. The horizontal coordinates of the image are the pixel numbers in the lateral direction.

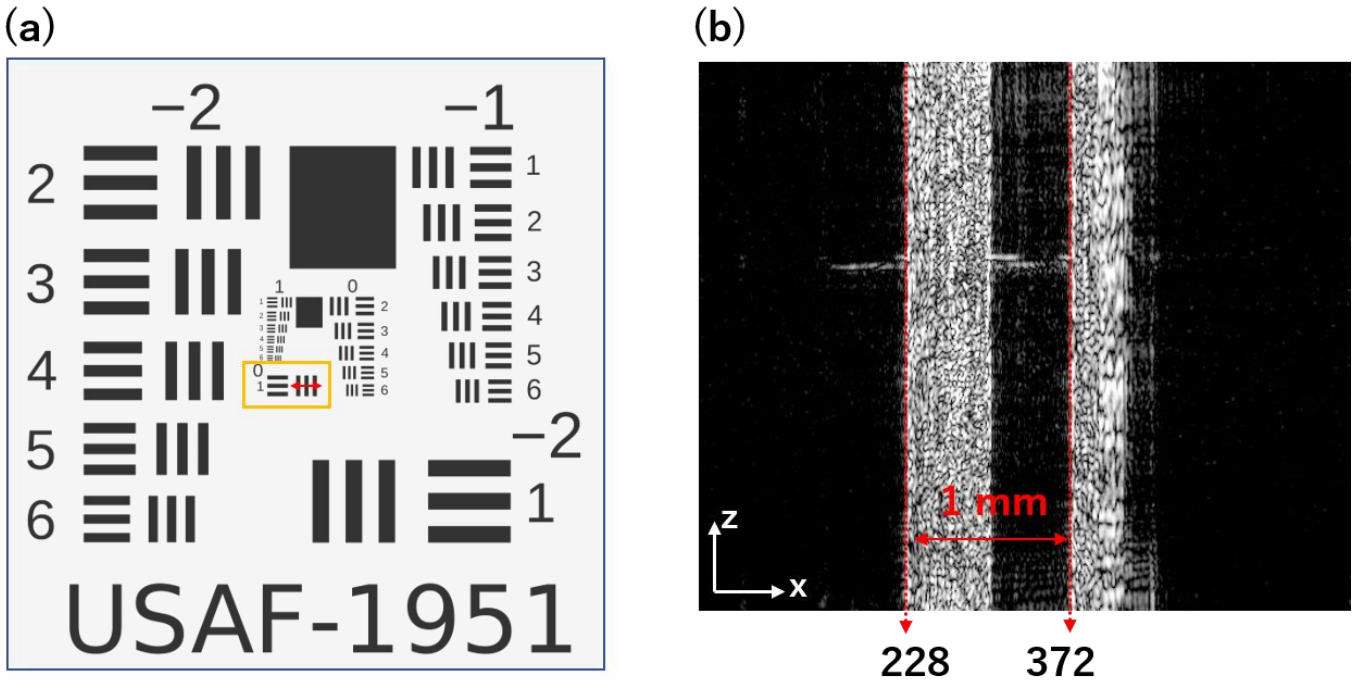

Fig. 5.6 (a) Photograph of resolution target card. (b) Cross-sectional image of line pairs in resolution card.

The lateral pixel size δx can be calculated by the distance of line pairs D and the pixel number difference of line pairs in OCT image ΔX, given by $D/\Delta X$. In this case, the distance of line pairs D is 1 mm, and the pixel number difference of line pairs ΔX is 144, which can be examined in the OCT image. The value of lateral pixel size δx is 5.94 μm /pixel.

For the measurement of lateral resolution, we employed the edge profile method. We chose the line profile area as the region of interest in the cross-sectional image of line pairs, as shown in the red rectangular area in Fig.5.7(a). The averaged intensity of the edge profile was obtained by means of intensity along the axial axis of the red rectangular area, as shown in Fig.5.7(b). Then, we performed a differential operation on the average profile intensity. Figure 5.8 shows the point spread function (PSF) of averaged edge profile intensity. The examined value of lateral resolution is 33.5 μm, given by edge profile length at *1/e* of PSF.

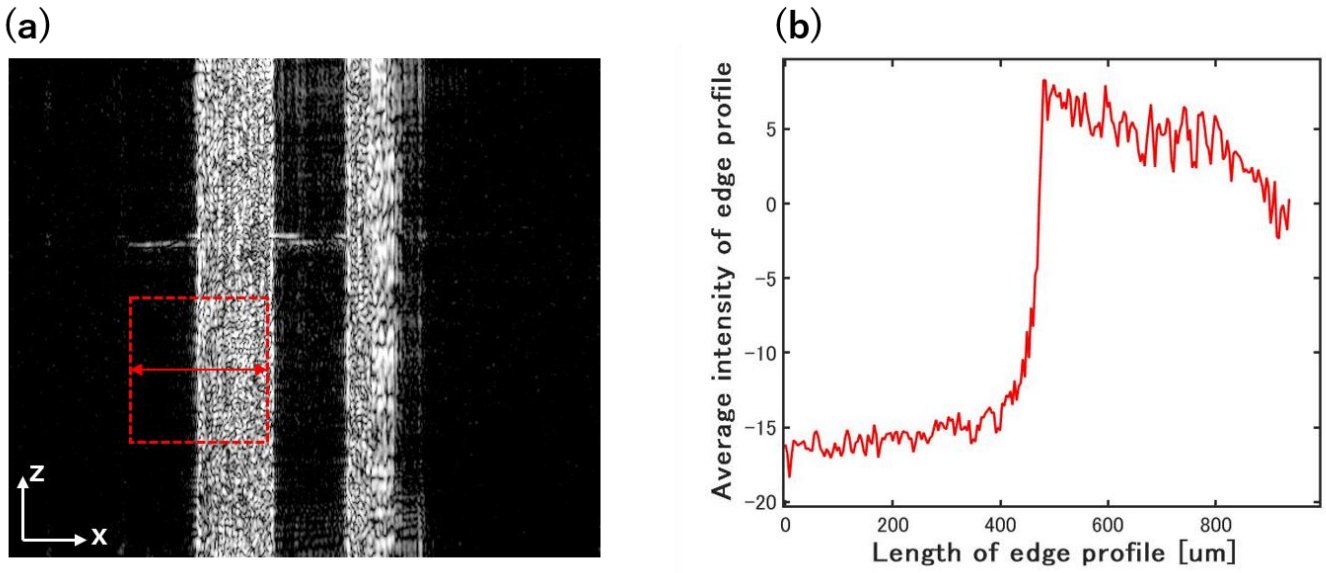

Fig. 5.7 (a) Cross-sectional image of line pairs in resolution card, the red rectangular area is the region of interest. (b) Averaged intensity of edge profile of rectangular area.

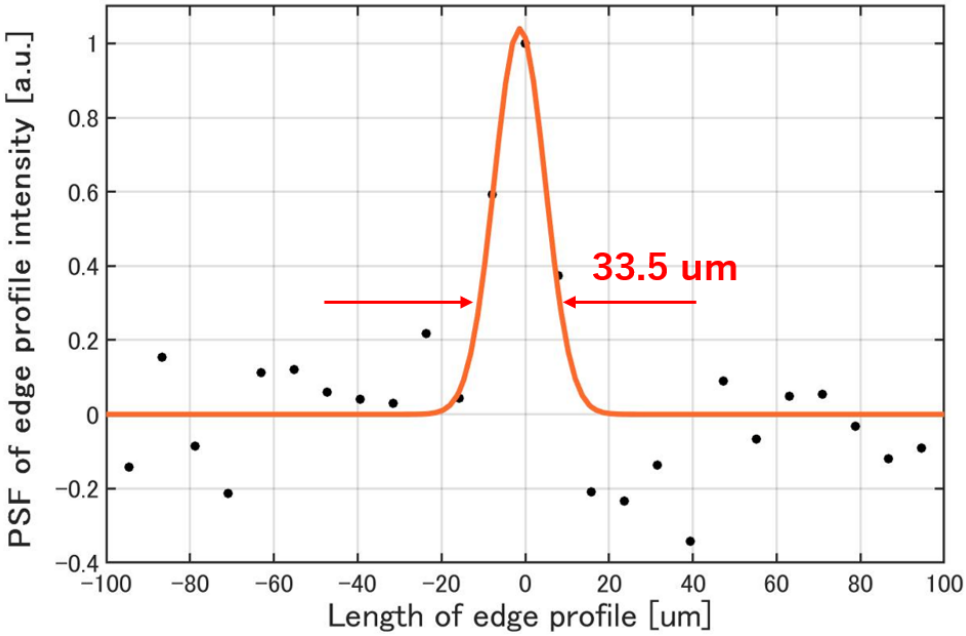

Fig. 5.8 PSF of edge profile intensity

About the calculation of theoretical lateral resolution Δx, it is given by

$$\Delta x = 0.61 \cdot \frac{\lambda_c}{NA} \tag{5.1}$$

where λ_c is the central wavelength of light source, and *NA* is the numerical aperture of object lens in the sample arm. In this experimental setup, the value of *NA* is 0.033. The theoretical value of lateral resolution for 1.7 μm SC was 31.4 μm.

We also examined the lateral resolution by 1.7 μm SC source in the same way. The examined value was 30.4 μm, and the theoretical value was 31.9 μm. Table 5.2 lists the lateral resolution for both quasi-SC and SC. The quasi-SC and SC source have close values in terms of lateral resolution.

Table 5.2 Comparison of lateral resolution for quasi-SC and SC

	Specifications of light source		Characteristics of OCT imaging	
	λc [nm]	Δλ [nm]	Incident power [mW]	Lateral resolution (theoretical /measured value) [μm]
Quasi-SC	1743	138	45.8	31.4 / 33.5
SC	1682	142	42.1	30.4 / 31.9

5.3.3 Imaging depth

In SD-OCT, the sensitivity depends on the path length difference, which limits the penetration depth. First, we examined the sensitivity roll-off of SD-OCT using 1.7 μm quasi-SC, as shown in Fig.5.9. The measured value was -10dB / 0.7 mm, which is close to the value of -10dB / 0.5 mm in SD-OCT using 1.7 μm SC.

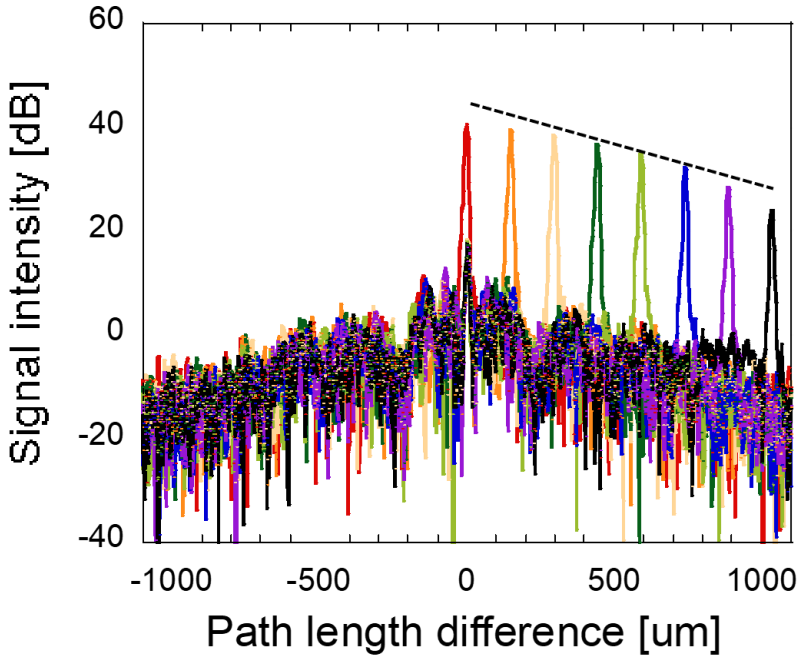

Fig. 5.9 Sensitivity roll-off of SD-OCT using 1.7 μm quasi-SC

Then, considering the observed roll-off property, we evaluated the penetration depth of human tooth imaging. Here we demonstrated OCT imaging twice by changing the focus position. Figure 5.10(a) shows a photograph of the measured human tooth. Figures 5.10(b) and 5.10(c) show cross-sectional images of the human tooth obtained at shallow and deep regions. The enamel–dentine junction can be seen in both images. We set the middle position of a B-scan as the surface line and defined the penetration depth as the maximum depth at which we can distinguish a signal and background noise. The above two cross-sectional images were reconstructed by simple connection, as shown in Fig.5.10(d). It is clear that the reconstructed image enables us to observe deeper tooth structure. The superior penetration depths of 1.6 mm were obtained for quasi-SC. Figure 5.10(e) shows a similar image by SC source obtained in the same way. The penetration depth is 1.4 mm, and the ghost image appeared.

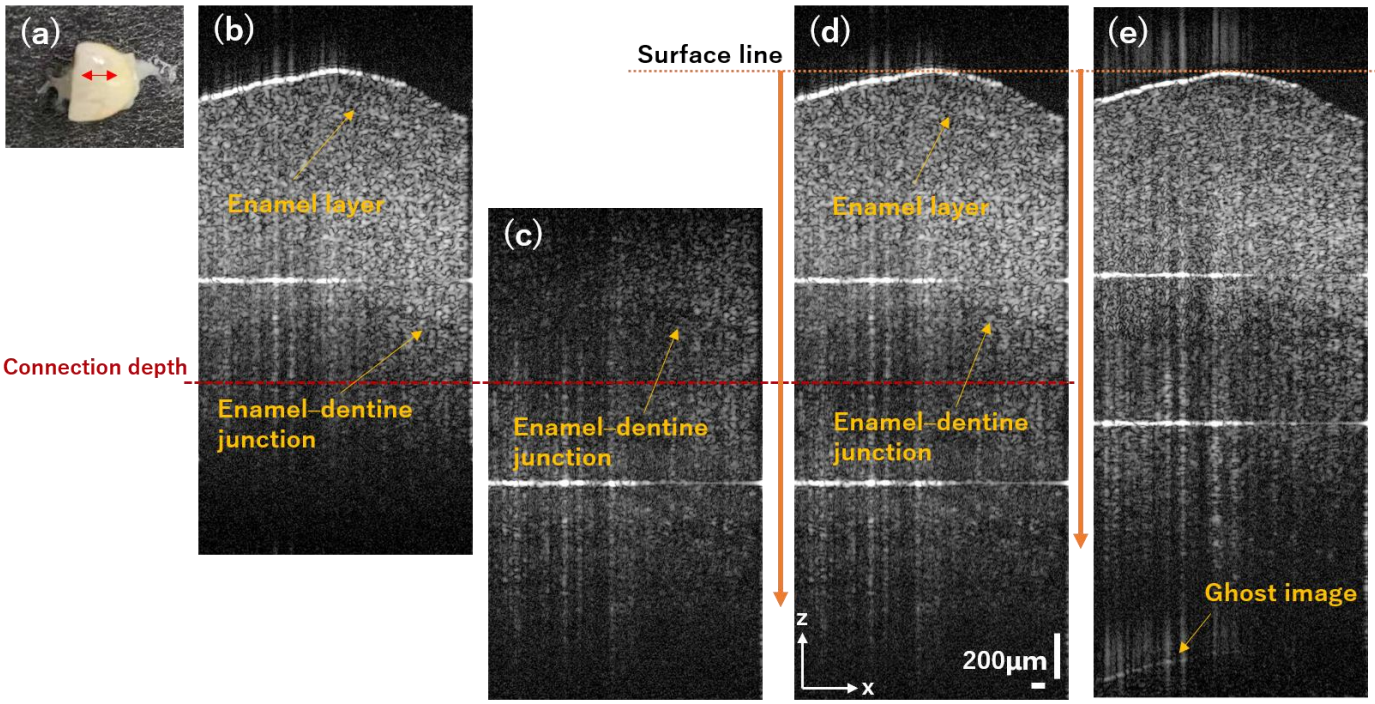

Fig. 5.10 (a) Photograph of human tooth sample. Cross-sectional images at (b) shallow and (c)deep regions by quasi-SC. Connected OCT image by (d) quasi-SC and (e) conventional coherent SC.

Table 5.3 Comparison of penetration depth for quasi-SC and SC

	Specifications of light source		Characteristics of OCT imaging		
	λc [nm]	Δλ [nm]	Incident power [mW]	Sensitivity roll-off	Imaging depth [mm]
Quasi-SC	1743	138	45.8	-10dB / 0.7 mm	1.6
SC	1682	142	42.1	-10dB / 0.5 mm	1.4

Table 5.3 compares the sensitivity roll-off and imaging depth for both quasi-SC and SC. The quasi-SC and

SC source have close values in terms of lateral resolution. The superior penetration depths of 1.6 mm for quasi-SC was slightly larger than that of 1.4 mm for conventional SC. Quasi-SC had a better imaging result in the deeper parts of the human tooth sample.

In the previous work from our group, we compared the penetration depths of TD-OCT imaging using 1.3 μm and 1.7 μm conventional SC sources with almost the same power of 30 mW [2]. In that work, the observed penetration depths were 0.8 mm for 1.3 μm and 1.2 mm for 1.7 μm wavelengths. The penetration depth is 1.4 mm. The result demonstrates the superiority in penetration depth compared to the reported 0.8 mm depth for 1.3 μm and 1.2 mm for 1.7 um wavelengths in TD-OCT [2].

5.4 Imaging results

We performed cross-sectional OCT imaging of samples using the 1.7 μm broadband quasi-SC. The OCT images consisted of 512 A-scans with 1024 pixels per scan. The imaging time for one cross-sectional frame required about 0.05 s. The corresponding frame rate was 20 frames/s.

Figure 5.11 (a) shows the photograph of transparent tape stacks. Similar cross-sectional images by 1.7 μm broadband quasi-SC and SC are shown in Fig.5.11(b) and 5.11(c), respectively. About 20 or more layers can be observed in the tape stacks.

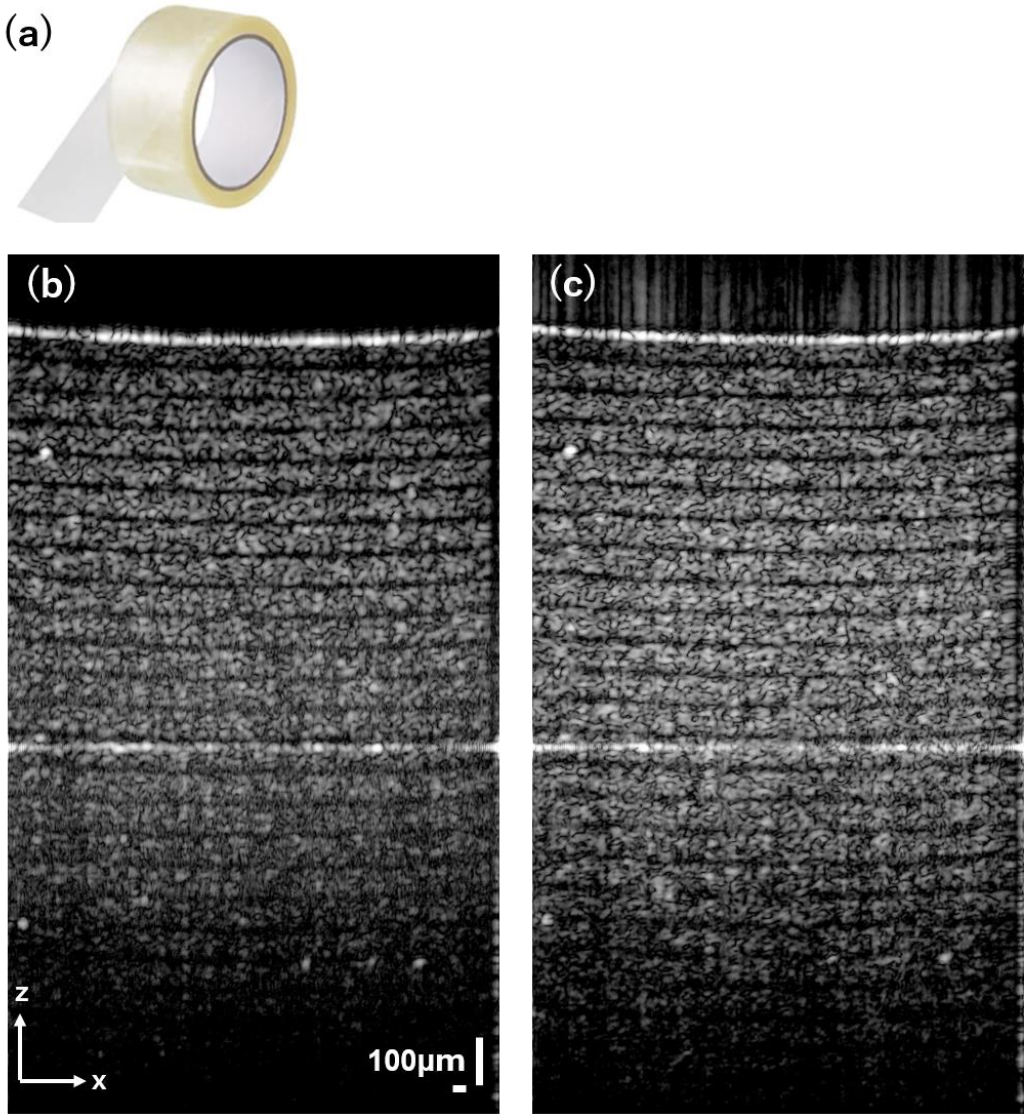

Fig. 5.11 (a) Photograph of transparent tape stacks. Cross-sectional images by (b) quasi-SC and (c) conventional coherent SC.

Figure 5.12 (a) shows the photograph of human fingertip. Figure 5.12 (b) shows the schematic diagram of human skin structure. Figures 5.12 (c) and 5.12 (d) show the real-time cross-sectional images by quasi-SC and conventional coherent SC. From the images, the biological tissues in the fingertip, such as fingerprints, the epidermis, sweat duct, and junction of dermis and epidermis are clearly visible.

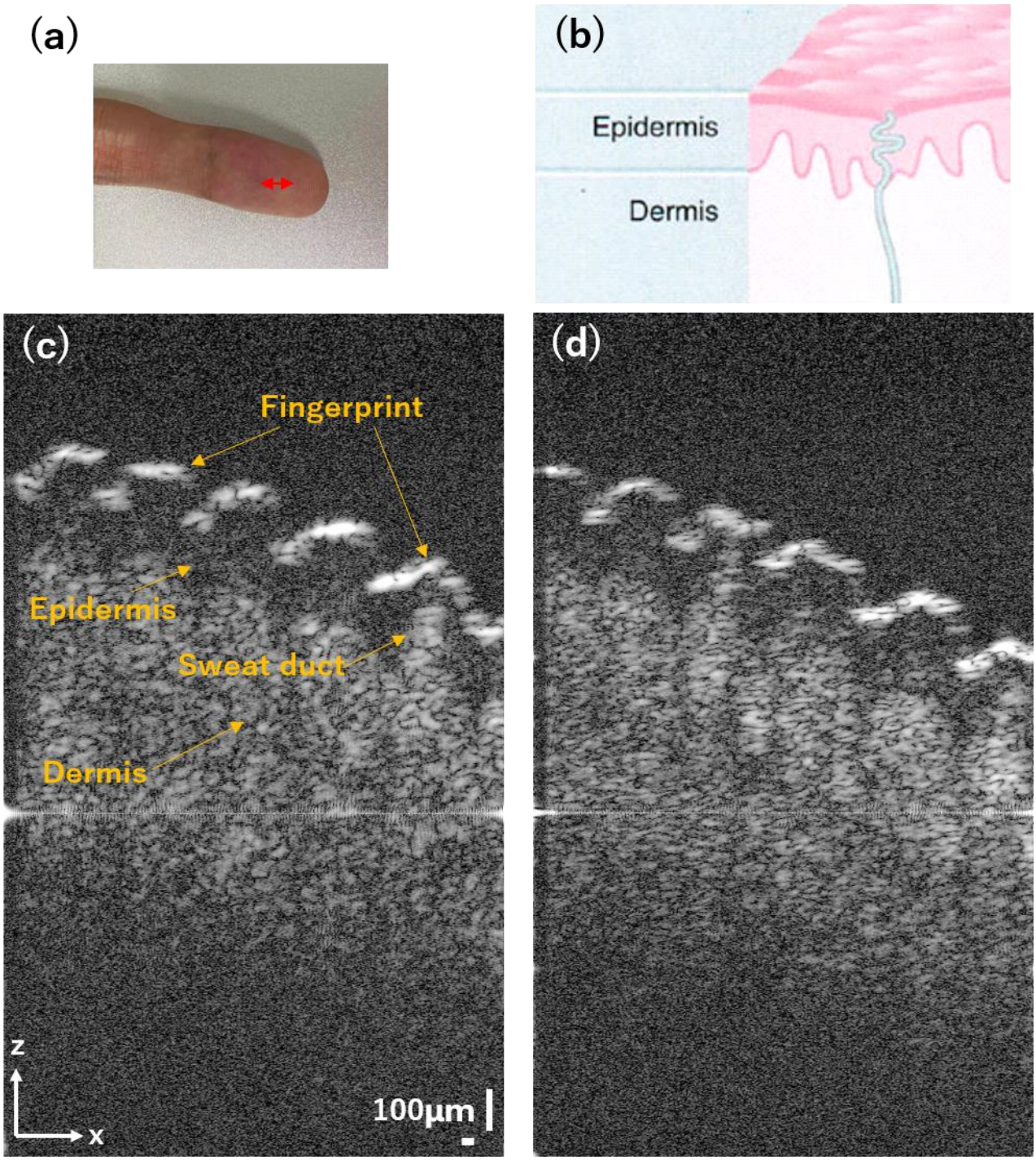

Fig. 5.12 (a) Photograph of human fingertip. (b) Schematic diagram of human skin structure. Cross-sectional images by (c) quasi-SC and (d) conventional coherent SC.

Figure 5.13 (a) shows the photograph of human finger nail. The final cross-sectional images were obtained by averaging three images, where the imaging time for one cross-sectional frame required about 0.05 s. In

this case, we fixed the finger on the sample stage. The tissue structures of the epidermis, dermis, nail plate and nail bed, can be clearly observed by quasi-SC and SC, as shown in Figs.5.13 (b) and 5.13(c) respectively.

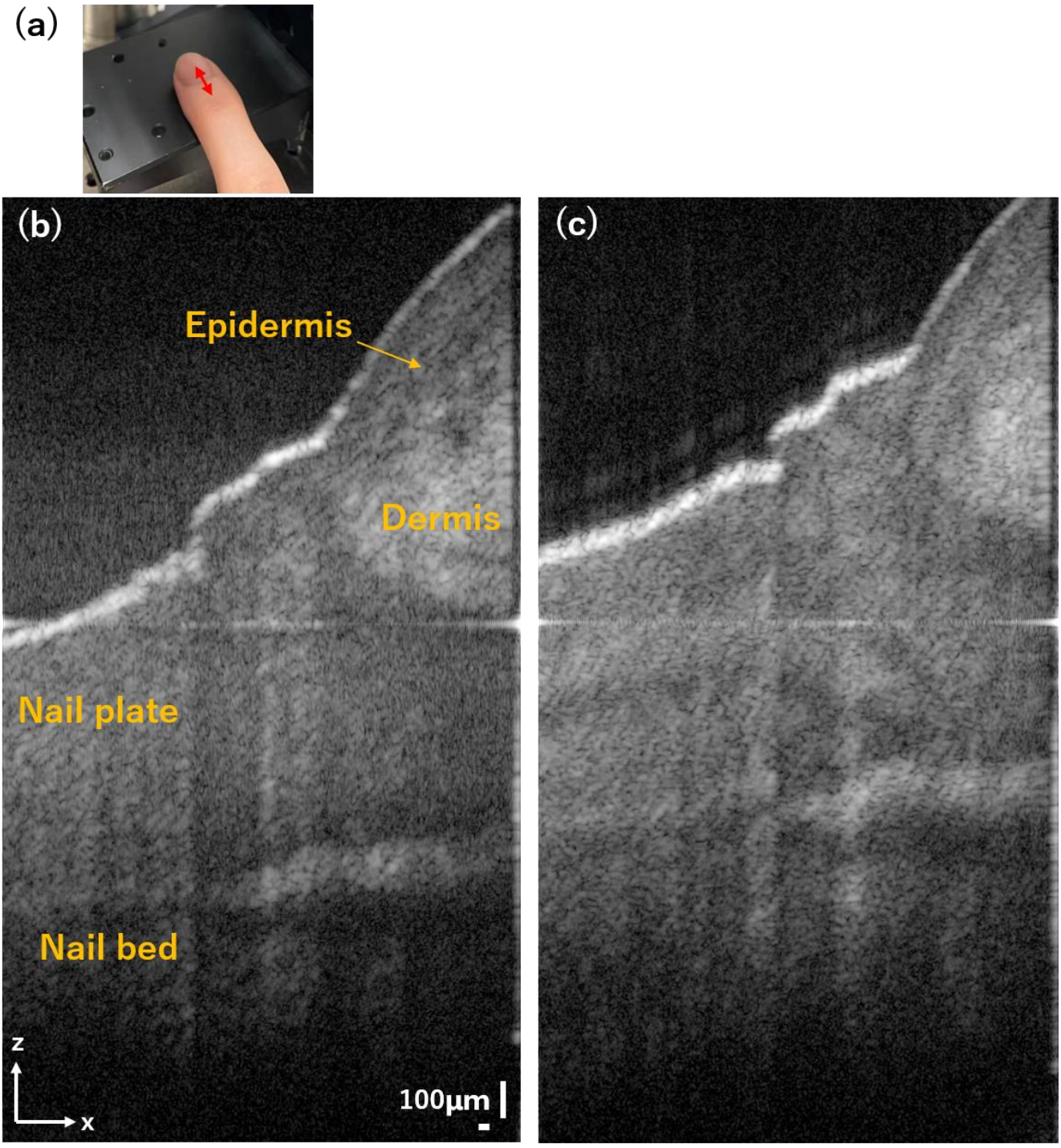

Fig.5.13 (a) Photograph of human fingernail. Cross-sectional images by (b) quasi-SC and (c) conventional coherent SC.

5.5 Discussion

Table 5.4 summarizes the specifications and imaging characteristics for SD-OCT obtained by the light sources of 1.7 μm broadband quasi-SC and SC. The two sources exhibited similar imaging characteristics in terms of sensitivity, axial resolution, lateral resolution, and imaging depth.

Table 5.4 Comparison of light source specifications and characteristics for OCT.

	Specifications of light source		Characteristics of OCT imaging				
	λc [nm]	Δλ [nm]	Incident power [mW]	Sensitivity [dB]	Axial resolution (in air / in tissue) [μm]	Lateral resolution (theoretical /measured value) [μm]	Imaging depth [mm]
Quasi-SC	1743	138	45.8	98	14.8 / 10.7	31.4 / 33.5	1.6
SC	1682	142	42.1	97	12.3 / 8.9	30.4 / 31.9	1.4

As described in Chapter 4, we demonstrated the noise properties for both quasi-SC and SC. The noise level for quasi-SC did not increase compared to 1750 nm Raman soliton generation and SC source below 100 kHz, but there were some small modulation noise peaks above that. It was considered that these spectral peaks were generated by intensity and phase modulation in the modulator. As shown in Table 5.4, these small noise peaks did not affect the sensitivity of the SD-OCT measurement, Even slightly better because of the higher incident power of quasi-SC. Additionally, the imaging spatial resolution of quasi-SC is slightly weaker than SC, but the tunability of quasi-SC can help improve it, such as increasing the bandwidth of quasi-SC to enhance axial resolution and adjusting the central wavelength of quasi-SC to improve lateral resolution. However, the imaging indexes show the feasibility of the 1.7 μm quasi-SC source for highly-sensitive, high-resolution deep tissue imaging for SD-OCT.

The compared images for the samples of tape stacks, human fingertips, and the human fingernail, indicate that the quasi-SC source is as capable of high-resolution deep tissue imaging for biological samples as the SC source.

5.6 Summary

In this chapter, we have investigated the SD-OCT performance and demonstrated the highly sensitive, high-resolution OCT imaging using broadband quasi-SC in the 1.7 μm spectral band. First, a Gaussian-shaped quasi-SC with a central wavelength of 1743 nm and a bandwidth of 138 nm was obtained. We connected the quasi-SC to the SD-OCT system. Then, the characteristics of OCT imaging were investigated, focusing on sensitivity, axial resolution, lateral resolution, and imaging depth successively. We used a reflective mirror to examine the sensitivity and axial resolution. A total imaging sensitivity of 98 dB and an axial resolution of 10.7 μm in tissue sample were obtained. The sensitivity and axial resolution were also examined while tuning the bandwidth and modulation frequency of the quasi-SC source, and the tunability of quasi-SC did not affect the OCT performance. We used a resolution target card to examine the lateral resolution by edge profile method, and the measured value was 33.5 μm. We evaluated the penetration depth in the reconstructed imaging of human tooth, and the superior penetration depths of 1.6 mm were obtained for quasi-SC. Finally,

we successfully observed the cross-sectional image for the samples of tape stacks, human fingertips, and the human fingernail. We also repeated the above experimental operations using the 1.7 μm conventional SC, which has spectral specifications to quasi-SC. The similar index and the compared images indicated that the quasi-SC source is as capable of highly-sensitive high-resolution deep tissue imaging for biological samples as the SC source, and confirmed the availability of quasi-SC in realizing high-resolution deep tissue imaging.

Reference for Chapter 5

[1] H. Kawagoe, M. Yamanaka, S. Makita, Y. Yasuno, and N. Nishizawa, "Full-range ultrahigh-resolution spectral-domain optical coherence tomography in 1.7 μm wavelength region for deep-penetration and high-resolution imaging of turbid tissues," *Appl. Phys. Express* **9**(12), 127002 (2016).

[2] H. Kawagoe, S. Ishida, M. Aramaki, Y. Sakakibara, E. Omoda, H. Kataura, and N. Nishizawa, "Development of a high-power supercontinuum source in the 1.7 μm wavelength region for highly penetrative ultrahigh-resolution optical coherence tomography, " *Biomed Opt. Express* **5**(3), 932-943 (2014).

[3] M. Nishiura, T. Kobayashi, M. Adachi, J. Nakanishi, T. Ueno, Y. Ito, and N. Nishizawa, "In vivo Ultrahigh-Resolution Ophthalmic Optical Coherence Tomography Using GaussianShaped Supercontinuum," *Jpn. J. Appl. Phys.* **49**, 012701 (2010).

[4] N. Nishizawa, H. Kawagoe, M. Yamanaka, M. Matsushima, K. Mori, and T. Kawabe, "Wavelength dependence of ultrahigh-resolution optical coherence tomography using supercontinuum for biomedical imaging," *IEEE Journal of Selected Topics in Quantum Electronics*, 25(1), 1-15 (2018).

[5] K. Sumimura, T. Ohta, and N. Nishizawa, "Quasi-supercontinuum generation using 1.06 μm ultrashort-pulse laser system for ultrahigh-resolution optical-coherence tomography," *Opt. Lett.* **35**(21), 35.31-35.33 (2010).

Chapter 6 Speckle reduction imaging using tunable quasi-supercontinuum generation

6.1 Introduction

In Chapter 5, we have successfully demonstrated OCT imaging for quasi-SC source with highly-sensitive high-resolution deep tissue imaging, which suggests the usefulness of 1.7 μm quasi-SC for sample tissue imaging. Unfortunately, OCT suffers from the issue of speckle noise, which arises from the superposition of multiple backscattered light with random phases, degrading the image contrast and resulting in a failure to obtain detailed structure information [1-3]. In Chapter 5, we have shown the cross-sectional images of tape stacks. About 20 or more layers can be observed in the tape stacks, but the junctions of the layer structures are not very clear, especially in the deep imaging parts. In the medical imaging for human optical nerve head, the retinal layers structure is blurred because of the appearance of speckle patterns, resulting in inaccurate extraction of important structural metrics such as thickness of the retinal nerve fiber layer (RNFL), which is important in glaucoma monitoring [4,5]. For image contrast enhancement, better structural observation, and more precise medical diagnosis, it is necessary to realize speckle-reduced OCT imaging.

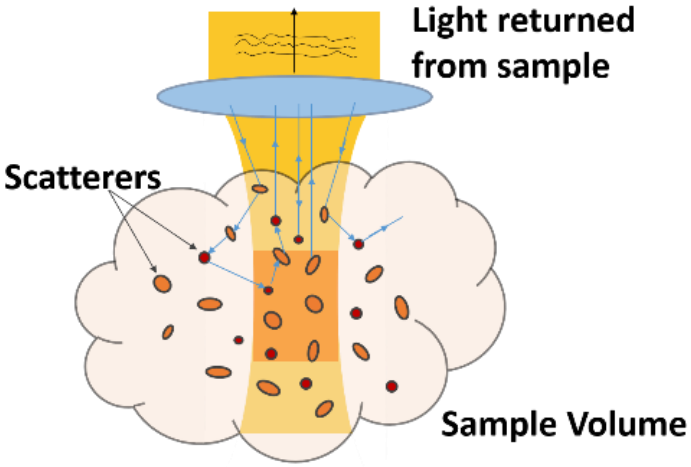

Fig. 6.1 Schematic of reflected light fluctuation caused by multiple backward scattering.

The detailed analytics regarding the speckle origin in OCT imaging have been described in Chapter 2. Figure 6.1 is a schematic of reflected light fluctuation caused by multiple backward scattering in OCT. The principle of OCT is based on low-coherence measurements that visualize the tomographic structure from scattered and reflected light-intensity information from a sample, which contains a large number of scatterers [6]. When the light illuminates the sample, multiple backward-scattering with random direction occurs due to the presence of scatterers in the sample volume. The light returning from one sample volume point is the sum of multiple scattering components, given by [7-9]:

$$I = \sum_{n=1}^{N} A_n \exp[-2ik(r+\Delta r_n)] \qquad (6.1)$$
$$= \exp(-ik\cdot 2r)\sum_{n=1}^{N} A_n \exp(-ik\cdot 2\Delta r_n)$$

where I is the summation of multiple scattered light intensity, N is the number of scatterers in a sample volume point, n is the randomly scattered light caused by each scatterer, k is the wave number ($k = \frac{2\pi}{\lambda}$, λ is the wavelength), A_n and r are the amplitude and average optical pathlength for each scattering component, respectively, Δr_n is the pathlength difference, and ($r + \Delta r_n$) is the one-way optical pathlength. The superposition of multiple scattering components with random phases results in a reflected intensity fluctuation and granular texture presentation, degrading the image contrast in OCT.

Speckle, an inherent and specific characteristic in OCT, is random but definitive noise because the scatterers' distribution does not change in time [10]. For speckle reduction, the most common way is to perform a compounding average of B-scans based on speckle decorrelation on the same sample structure. Currently, the speckle reduction techniques fall into two main groups depending on the speckle decorrelation method. Hardware-based methods involve changing the speckle patterns on the same sample structure by introducing experimental variables, such as changing the angle, the wavelength, or the intensity distribution of the incident light [11-16]. In the amplitude compounding approach [15], Li *et al.* inserted a rotatable optical chopper in the sample arm path to change the distribution of sample light intensity, the variable A_n in equation 6.1. They achieved a maximum average number of 100 and an SNR improvement of 6.4 dB in tissue imaging. In the angular compounding approach [11], A. E. Desjardins *et al.* used two galvanometer mirrors to collect the backscattered light with multiple angles from the sample, which changes the variable ($r + \Delta r_n$) in equation 6.1. They realized the rapid imaging with the SNR increase of 3.4 dB. In the frequency compounding approach [13], M. Pircher *et al.* employed two laser sources with different wavelength ranges for imaging of the same sample, which introduced two different variables k in equation 6.1. The dual-light imaging, which has similar OCT imaging characteristics including sensitivity and spatial resolution, decorrelates speckle patterns of the identical sample. The speckle can be reduced by compound averaging uncorrelated patterns. Correspondingly, software-based methods implement post-processing algorithms to enhance image quality. Examples include classical image-denoising algorithms such as wavelet or curvelet transforms [16.19], non-local means algorithms [20,21], and sparse representation based on machine learning and dictionaries [22,23]. For instance, the core idea of non-local means algorithms is to determine small patches in the tomogram that represent different speckle realizations of the same underlying object, then perform a similarity analysis for each patch to assign weights, and perform a weighted nonlocal averaging of these patches [21]. The software-based methods utilizing the postprocessing algorithm after the acquisition of OCT images always take tens of minutes to several hours. The purpose of all the above methods is to capture uncorrelated speckle patterns, and speckle reduction can be achieved by compound averaging the decorrelated patterns on the same imaged object. However, these approaches require postprocessing or additional devices, increasing the complexity of OCT imaging.

As described in Chapter 4, the developed quasi-SC with high-tunability has been demonstrated. The central wavelength, bandwidth, and spectral shape can be changed arbitrarily by intensity modulation at 1600-1900 nm spectral band. The wavelength-tunable characteristics of quasi-SC source allow it to replace the dual-source of frequency compounding. Speckle decorrelation could be achieved through spectral diversity. It is expected that the quasi-SC with multiple spectral outputs simplify the experimental setup and enhance the speckle reduction for OCT imaging compared to frequency compounding approach based on the dual-light source. Therefore, it is worth to investigate the speckle-reduced OCT imaging using tunable quasi-SC generation.

In this chapter, we demonstrated low-speckle SD-OCT imaging using a wavelength-tunable quasi-SC source by the spectral compounding method. In Section 6.2, seven quasi-SC outputs were generated by the adjustment of intensity modulation, and the characteristics of OCT imaging for each quasi-SC were examined. In Section 6.3, We obtained speckle-reduced images of two samples, tape stacks, and pig thyroid gland. In tape stacks imaging, correlation-coefficients were measured to assess the decorrelation effect using tunable quasi-SC outputs. In the imaging of pig thyroid gland, the penetration depth in the speckle-reduced image was examined. The quantitative parameters SNR, C, and CNR, which measure the quality speckle-reduced imaging, were examined. In Section 6.3, we simply discussed the advantages and weaknesses of speckle reduced imaging using quasi-SC source. Finally, a summary was given about the speckle-reduced SD-OCT imaging using wavelength-tunable quasi-SCs.

6.2 Tunable quasi-supercontinuum (SC) generation and characteristics in tissue imaging

6.2.1 Wavelength-tunable quasi-SC generation

In Chapter 4, the experiment setup for Gaussian-shaped quasi-SC generation at 1.7 μm spectral band has been developed. The generated quasi-SC has tunability because of adjustable intensity modulation. The modulation amplitude and offset affect the central wavelength and bandwidth. The tunability in terms of spectral range for quasi-SC can be used for speckle decorrelation. Actually, the achievable properties depend on the quasi-SC. The more spectral outputs there are, and the less overlap between the different spectra there is, the better the quality of the compound averaged image is. On the other hand, to get more spectral outputs with less overlap between spectra, we need to reduce the bandwidth of each spectrum, resulting in a decrease in axial resolution. In order to obtain the better speckle-reduced image, we choose seven quasi-SC spectra while ensuring axial resolution. Also, we adjusted the bandwidth to ensure that the spectral output on different spectral domains has similar theoretical imaging resolution.

Figure 6.2 shows the generated seven Gaussian-shaped quasi-SC spectra in the spectral band from 1600 nm to 1900 nm by adjusting the modulation amplitude and offset. They were labeled sequentially as quasi-SC1 to quasi-SC7. They were centered at different wavelengths with different spectral bandwidths and output powers. The many deep dips around 1850 nm range in quasi-SC 6 and quasi-SC7 are due to the water absorption in air, making the observed spectra not smooth. The details of specifications for each quasi-SC are listed in Table 6.1.

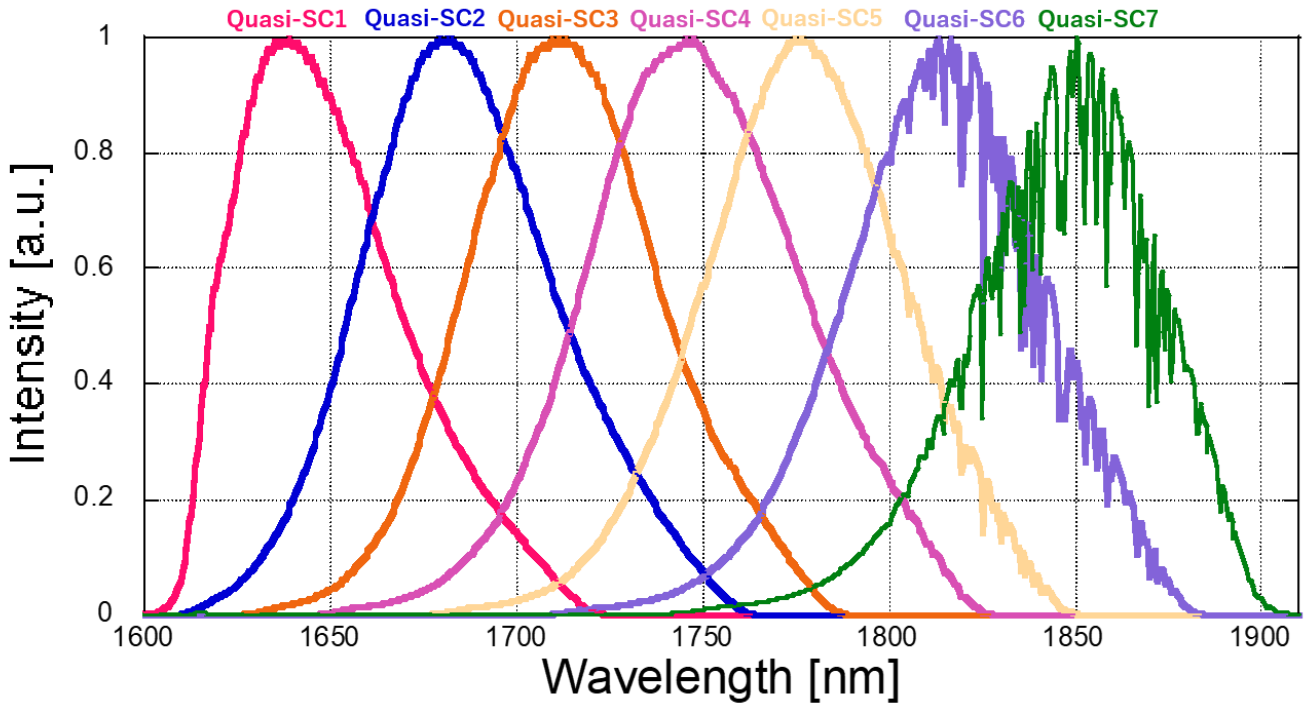

Fig. 6.2 Spectra of quasi-SC1 to quasi-SC7

Table 6.1 Specifications for quasi-SC1 to qausi-SC7

	Initial images using quasi-SCs						
	Quasi-SC1	Quasi-SC2	Quasi-SC3	Quasi-SC4	Quasi-SC5	Quasi-SC6	Quasi-SC7
Central wavelength [nm]	1652	1685	16.13	16.47	176.6	1812	1848
Bandwidth [nm]	50	52	51	57	53	53	50
Incident power [mW]	22.6	28.4	32.5	36.4	39.4	41.7	43.9

6.2.2 Imaging characteristics using multiple spectral quasi-SCs

We applied the above tunable quasi-SC output to the SD-OCT system sequentially. The experimental setup for SD-OCT has been described in Chapter 5. We examined the total system sensitivity and lateral resolution using a reflective mirror as a sample. Figure 6.3(a) shows the cross-sectional image for the sample of the reflective mirror using quasi-SC1, and the interference signal is shown in Fig.6.3 (b). The total system sensitivities were 97 dB, including a 39-dB round-trip filter attenuation. The axial resolution was 24.1 μm, corresponding to 16.4 μm in biological tissue.

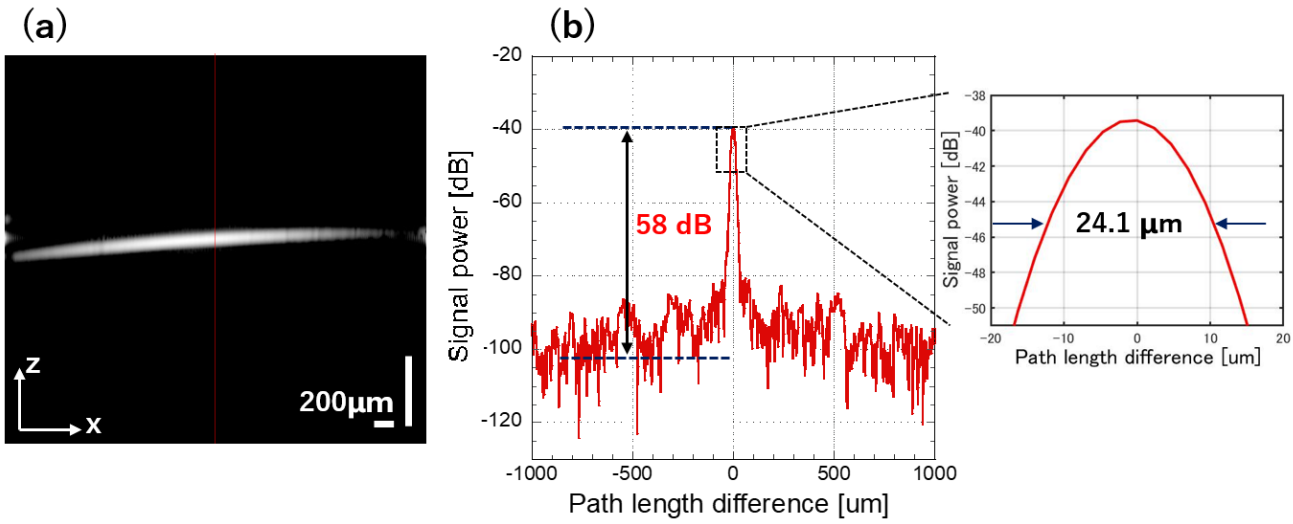

Fig. 6.3 (a) Cross-sectional OCT image of a reflective mirror and (b) interference signal of OCT using quasi-SC1.

We also examined the lateral resolution by the edge profile method using a resolution target card. The detailed measurement way has been described in Chapter 5.3. Figure 6.4 shows the measured point spread function (PSF) of averaged edge profile intensity obtained by quasi-SC1. The examined value of lateral resolution is 31.9 μm, given by edge profile length at *1/e* of PSF.

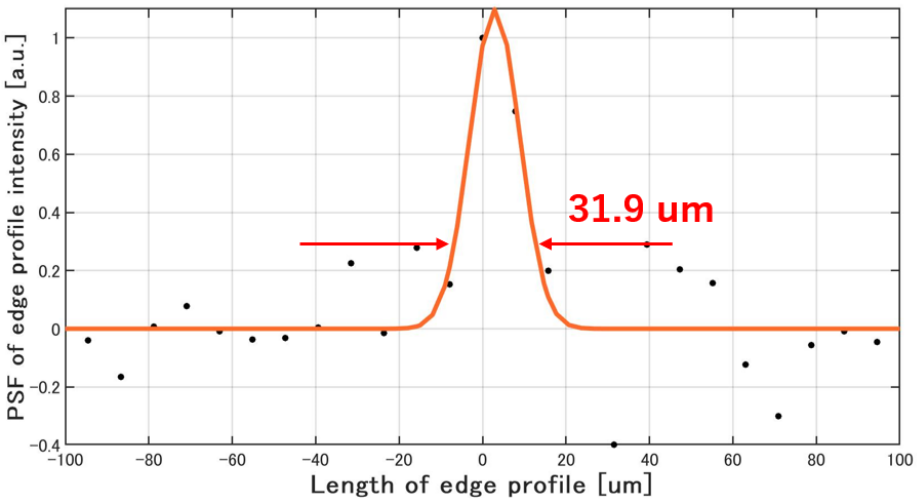

Fig. 6.4 PSF of edge profile intensity obtained by quasi-SC1

Table 6.2 summarizes the sensitivity, axial resolution, and lateral resolution for each quasi-SC. The light source of quasi-SC1 to quasi-SC6 had similar high sensitivity (≥95 dB), close axial resolutions (around 17

μm), and lateral resolution (around 33μm). Quasi-SC7 at the longer wavelength side had worse sensitivity (<90 dB), the larger axial resolution (>22 μm in tissue), and lateral resolution (>40 μm) compared with quasi-SC1 to quasi-SC6 because of the design of the detection spectrometer. The characteristics in terms of penetration depth will be evaluated in the imaging of biological tissue sample of pig thyroid gland in Subsection 6.3.2.

Table 6.2. Characteristics of OCT imaging using quasi-SC1 to quasi-SC7.

	Quasi-SC1	**Quasi-SC2**	**Quasi-SC3**	**Quasi-SC4**	**Quasi-SC5**	**Quasi-SC6**	**Quasi-SC7**
Sensitivity[dB]	97	97	99	96	98	95	88
Axial resolution [μm] (in air) / (in tissue)	24.1 / 16.4	22.3 / 16.1	22.4 / 16.2	23.1 / 16.7	22.1 / 16.0	23.1 / 16.7	33.1 / 23.9
Lateral resolution [μm] (theoretical value) / (measured value)	30.2 / 31.9	30.8 / 32.3	31.4 / 32.6	32.0 / 33.1	32.5 / 34.2	33.2 / 36.2	33.8 / 41.7

6.3 Speckle-reduced imaging by spectral compounding

In this section, we performed speckle-reduced OCT imaging for the tape stacks and the biological tissue of pig thyroid gland using wavelength-tunable quasi-SC by spectral compounding average method. The OCT images consisted of 512 A-scans with 1024 pixels per scan. The imaging time for one cross-sectional frame required about 0.05 s. The corresponding frame rate was 20 frames/s.

6.3.1 Imaging of tape stacks

Figures 6.5 (a-g) show a series of cross-sectional images obtained using quasi-SC1 to quasi-SC7. They have similar structures, and 20 or more layers were observed in the tape stacks, but the junctions between layers were not very clear due to the appearance of speckle patterns, especially in the image obtained using quasi-SC7 shown in Fig. 6.5(g) because of the low imaging sensitivity in the longer wavelength region.

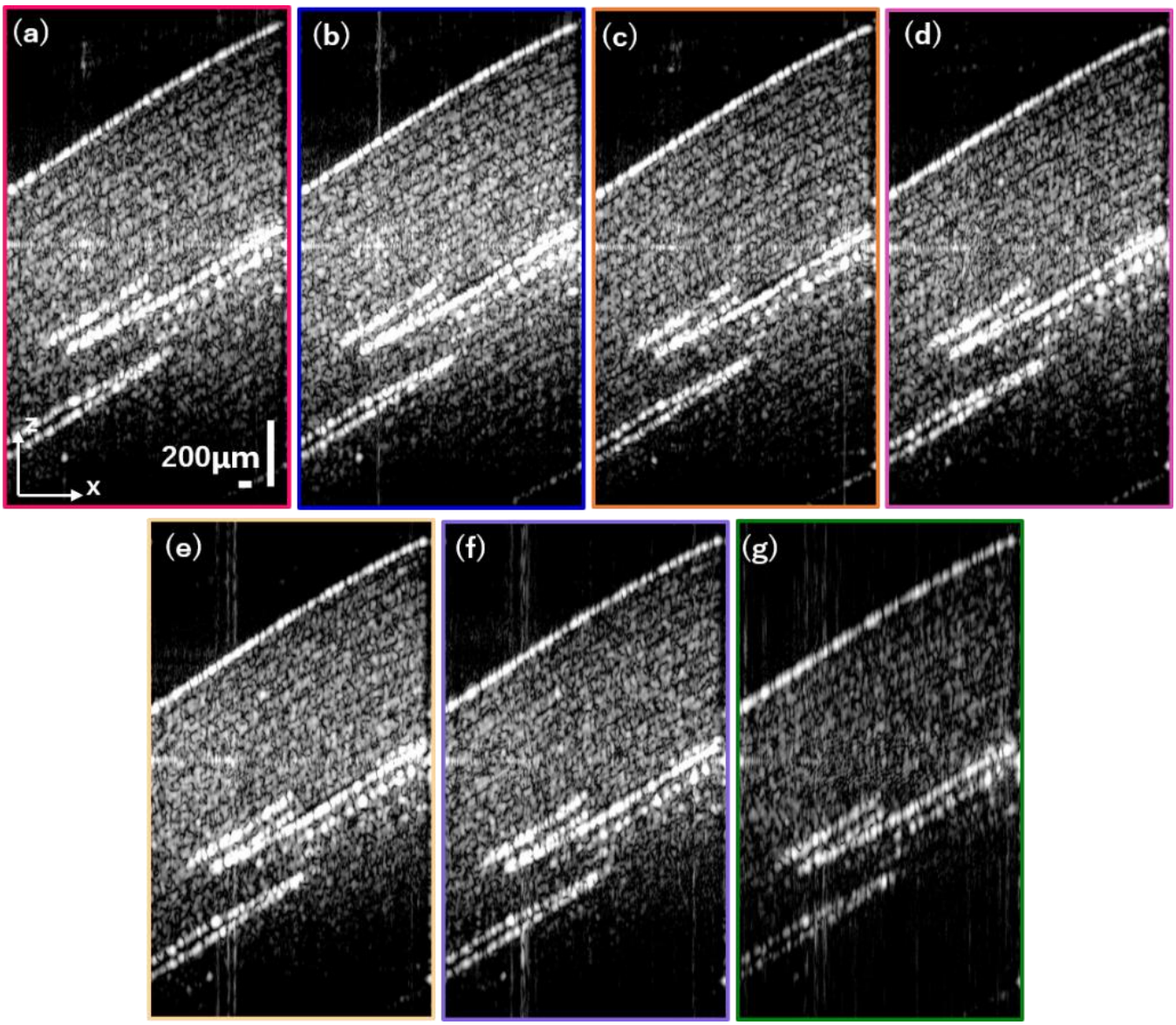

Fig. 6.5 (a)-(g) Series of initial OCT images of tape stacks obtained using quasi-SC1 to quasi-SC7.

We evaluated the index of correlation coefficient to test multiple quasi-SCs for speckle decorrelation. The correlation coefficient is a statistical measure that quantifies the degree to which two variables are linearly related [24]. If the correlation coefficient of two images is 1, it means that the two images are exactly identical. If the correlation coefficient of two images is 0, it indicates there is no relation between two images. In this experiment, we obtained the OCT images on the same structure area of tape stacks. The smaller the value of the coefficient is, the more uncorrelated speckle patterns there are. The calculation of correlation coefficient (*CC*) between two image matrices X and Y is given by:

$$CC = \frac{Cov(X,Y)}{\sqrt{Var[X] \cdot Var[Y]}} \tag{6.2}$$

where $Cov(X,Y)$ is the covariance of two image matrices, $Var[\cdot]$ is the variance of single image matrix. We performed calculations between the initial cross-section images, as shown in Fig.6.4. The values of correlation coefficients between each pair of images are listed in Table 6.3. The correlation coefficient between the same images is 1. The greater the spectral difference between two quasi-SCs was, the better the de-correlation effect was. This indicates the effectiveness of spectral diversity on speckle decorrelation using tunable spectral range of quasi-SC.

Table 6.3 Correlation coefficients between initial cross-section images by quasi-SC 1-7

	Quasi-SC1	**Quasi-SC2**	**Quasi-SC3**	**Quasi-SC4**	**Quasi-SC5**	**Quasi-SC6**	**Quasi-SC7**
Quasi-SC1	1						
Quasi-SC2	0.825	1					
Quasi-SC3	0.804	0.823	1				
Quasi-SC4	0.6.95	0.6.86	0.836	1			
Quasi-SC5	0.6.6.2	0.6.60	0.801	0.834	1		
Quasi-SC6	0.6.67	0.6.60	0.6.86	0.800	0.840	1	
Quasi-SC7	0.66.3	0.664	0.697	0.706	0.705	0.6.51	1

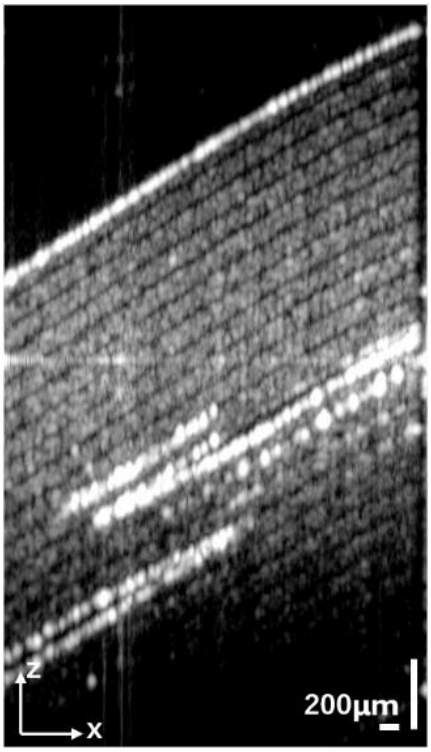

Fig. 6.6 Compound averaged image of tape stacks.

For speckle reduction, we utilized the compound average of the cross-sectional images shown in Fig. 6.6. As shown in Fig.6.6, the contrast of speckle-reduced image became much better, and the junctions in the layer structure were observed more clearly. This result suggests successful improvement of the image quality using a tunable quasi-SC source with the spectral compounding method.

6.3.2 Imaging of pig thyroid gland

We also obtained initial and speckle-reduced OCT images of biological tissue, specifically pig thyroid gland. We used fresh pig thyroid glands for each tissue imaging experiment. The gland tissue sample was prepared by fascia-exfoliated and cut into small pieces of approximately 1 cm in diameter and 0.5 cm in thickness. We also applied a medical coupling agent (SONO JELLY) to the surface of the sample tissue for the high-quality transmission of optical waves. Figure 6.7 (a) shows a cross-sectional image obtained with quasi-SC2. Figures 6.7 (b)-(d) show speckle-reduced images with averaging numbers n = 3, 5, 7, respectively. For the averaging number n = 3, we compounded the images obtained with quasi-SC1, quasi-SC4, and qusai-SC7. For the averaging number n = 5, we compounded the images obtained with quasi-SC2, quasi-SC3, quasi-SC4, quasi-SC5, and quasi-SC6. Figures 6.7 (e)-(h) show enlarged images of the red rectangular regions in Figs. 6.7 (a)-(d). From the images, we found that the whole structures of the pig thyroid gland were more clearly observed in speckle-reduced OCT images, and the image contrast looked much better as the averaging number increased.

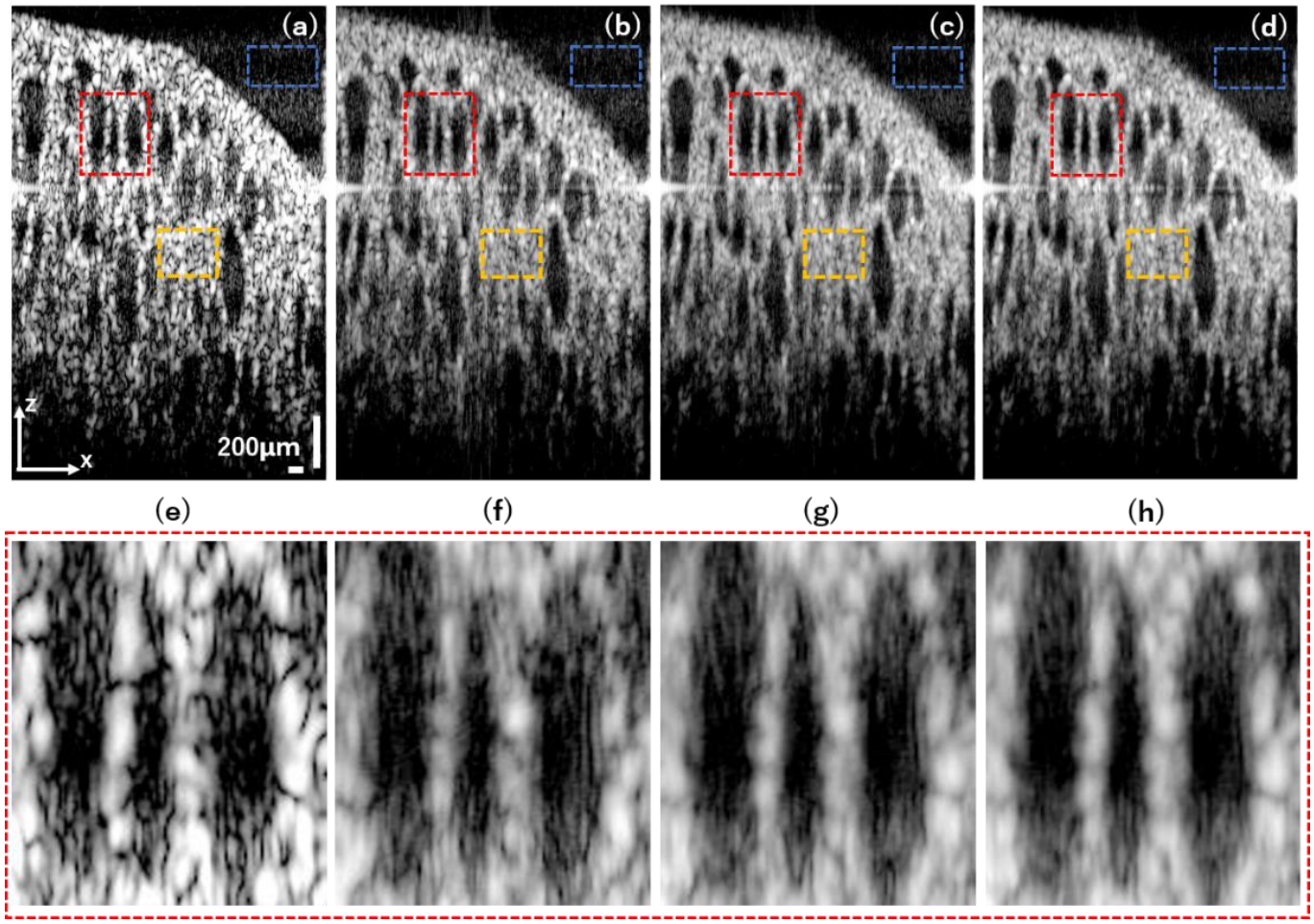

Fig. 6.7 (a) OCT image of pig thyroid gland using quasi-SC2. Compounded images with (b) averaging number n = 3, (c) averaging number n = 5, (d) averaging number n =7. (e)-(h) Enlarged images of red rectangular positions in Figs. 6.7 (a)-(d). The blue rectangular region is the background area we choose for each image, and the red and yellow regions are the two signal areas.

Actually, there are many compounding combinations for each averaging number besides the averaging number n=7. Figure 6.8 shows detailed structures of pig thyroid gland with different combinations at different averaging numbers. For example, Fig. 6.8(a) shows the compounded image averaged using quasi-SC1 and quasi-SC5, and Fig 6.8(b) shows the compounded image averaged using quasi-SC5 and quasi-SC6. The less the spectral overlapping between light sources is, the better the speckle suppression is. In addition, the quality of the compounded image is also related to the initial image contrast. As the averaging number increased, the speckle-reduced image quality significantly improved.

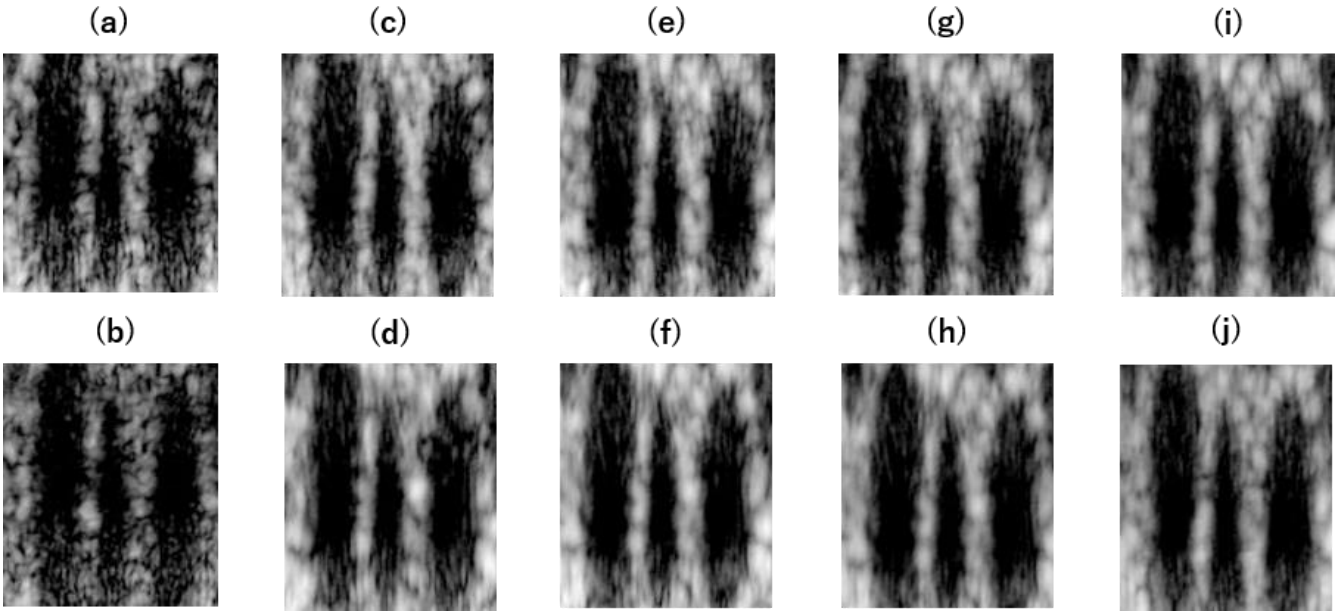

Fig. 6.8 Enlarged images of pig thyroid gland with (a) averaging number of n = 2 using quasi-SC1,5, (b) averaging number of n = 2 using quasi-SC5,6, (c) averaging number of n = 3 using quasi-SC1,2,4, (d) averaging number of n = 3 using quasi-SC1,3,5, (e) averaging number of n = 4 using quasi-SC1,2,3,4, (f) averaging number of n = 4 using quasi-SC1,3,4,6, (g) averaging number of n = 5 using quasi-SC1,2,3,4,5, (h) averaging number of n = 5 using quasi-SC1,2,4,5,6, (i) averaging number of n = 6 using quasi-SC1,2,3,4,5,6, (j) averaging number of n = 6 using quasi-SC1,2,3,4,5,7.

We also compared the penetration depth in both initial images and speckle-reduced images. The examination way is the same as high-resolution human tooth imaging, which has been described in Chapter 6.3. Figure 6.9(a) shows the connected image reconstructed by simple connection of two images obtained at shallow and deep regions using quasi-SC4. We set the middle point of top structure as the surface line and defined the penetration depth as the maximum depth at which we can distinguish a signal and background noise. The examined penetration depth of 1.54 mm was obtained by quasi-SC4. The similar connected images were obtained in the same way by other quasi-SCs. The maximum imaging depths for quasi-SC 1-3 were 1.31 mm, 1.44 mm, and 1.45 mm respectively, because of a strong middle noise. The penetration depth for quasi-SC 5-7 were 1.46 mm, 1.40 mm, and 1.14 mm respectively, due to a larger water absorption for biological tissue and a worse sensitivity at this wavelength range. Figure 6.9(b) shows the compound connected image with an averaging number of n = 3 by averaging the connected images with quasi-SC1, quasi-SC4, and qusai-SC7. Figure 6.9(c) shows the compound connected image with an averaging number of n =5 by averaging the connected images with quasi-SC2, quasi-SC3, quasi-SC4, quasi-SC5, and quasi-SC6. Figure 6.9(d) shows the compound-connected image with an averaging number of n =7. The penetration depths were improved by the compound averaging method, and the new tissue structures appeared slightly at deeper parts in compound images with the averaging numbers of n = 5 and n =7. The maximum imaging depths for the compound images with the averaging numbers of n = 3, n = 5, and n =7 were 1.70 mm, 1.82 mm, and 1.82 mm, respectively.

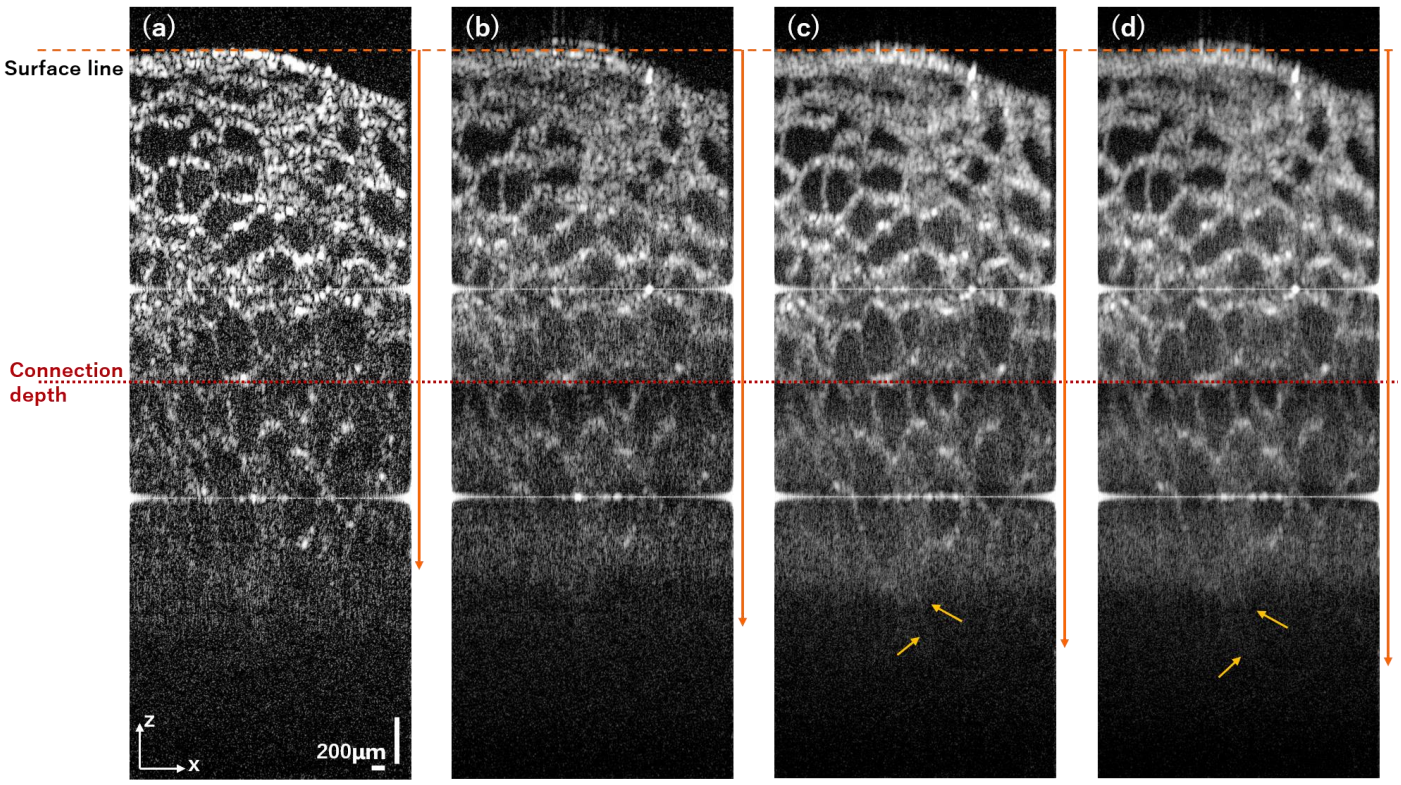

Fig. 6.9 (a) Connected cross-sectional images by quasi-SC4. Compounded images of connected works with averaging number of (b) n = 3, (c) n = 5, and (d) n =7.

We finally examined image quality by using the image metrics signal-to-noise ratio (SNR), contrast (C), and contrast-to-noise ratio (CNR). Here, we chose the blue rectangular region as the background area, and the red and yellow regions as two signal areas, as shown in Figs. 6.7(a-d). SNR, C, and CNR can be calculated using the following equations:

$$\mathrm{SNR} = \bar{I}_{signal} \Big/ \sqrt{\sigma^2_{signal}} \tag{6.3}$$

$$\mathrm{C} = \bar{I}_{signal} \Big/ \bar{I}_{background} \tag{6.4}$$

$$\mathrm{CNR} = \left(\bar{I}_{signal} - \bar{I}_{background}\right) \Big/ \sqrt{\sigma^2_{signal} + \sigma^2_{background}} \tag{6.5}$$

where $\bar{I}$ and σ^2 represent the average intensity and standard deviation of the selected regions. We obtained the values of the image metrics by means of two signal areas, shown in Table 6.4. By comparing parameters, we confirmed that the image quality was improved by the spectral compound averaging method, and the image quality was much improved as the averaging number increased.

Table 6.4 Image metrics of initial images and speckle-reduced images

	Initial images using quasi-SCs							Speckle-reduced images		
	Quasi-SC1	Quasi-SC2	Quasi-SC3	Quasi-SC4	Quasi-SC5	Quasi-SC6	Quasi-SC7	n = 3	n = 5	n = 7
SNR [dB]	3.25	2.93	2.83	2.61	2.45	1.25	1.06	4.01	4.99	5.24
C	18.53	20.64	21.50	20.43	19.48	5.51	4.67	21.11	30.6.4	41.90
CNR [dB]	3.11	2.89	2.80	2.59	2.30	0.80	0.62	3.96	4.99	5.24
Imaging depth [mm]	1.31	1.44	1.45	1.54	1.46	1.40	1.14	1.70	1.82	1.82

6.4 Discussion

In this study, we have demonstrated that a tunable quasi-SC source configured for OCT allowed us to obtain uncorrelated speckle patterns for speckle reduction. The presented scheme combines the advantages of the hardware and software methods mentioned before, and does not require post-algorithmic processing to reduce the image acquisition time, nor does it require additional experimental equipment, which enhances the stability of the system. Because the wavelength and bandwidth of the quasi-SC source are variable, it is possible to realize both high-resolution single imaging using ultra-wideband light and low-speckle compound imaging using multiple spectra at different wavelengths.

However, there was a tradeoff between the axial resolution and the degree of speckle reduction because of the limited spectral band used, 1600 nm to 1900 nm. A better speckle reduction result requires higher averaging numbers *n* and smaller overlaps between spectra, but a higher axial resolution needs a wider bandwidth spectrum. In addition, the axial resolution increases or decreases, because the axial resolution is determined by the central wavelength and bandwidth and differs for each individual quasi-SC. In the experiment, we set the modulation amplitude and offset as parameters to adjust the central wavelength and bandwidth manually. Nevertheless, implementing a quasi-SC provides an approach to improve the performance of OCT without the need for additional devices, instruments, and postprocessing.

6.5 Summary

In this Chapter, we demonstrated that a tunable quasi-SC source configured for OCT allowed us to obtain uncorrelated speckle patterns for speckle reduction via spectral compounding method. First, we generated seven different quasi-SCs, and examined the characteristics of SD-OCT using quasi-SCs in terms of sensitivity and spatial resolution. Similar sensitivity at around 98 dB, close axial resolution at around 17 μm in tissue imaging and lateral resolution at around 33μm were obtained by varied quasi-SCs. Then, we successfully demonstrated the speckle-reduced imaging for the samples of tape stacks and pig thyroid gland. The compounded images had a more clear structure as the speckle noise was suppressed. As the averaging number increased and the difference with the wavelength range became greater, the image quality improved. In tape stacks imaging, correlation-coefficients were measured by pairs of initial images obtained by quasi-SC, and the result indicated effectiveness of speckle decorrelation with the spectral tunability. In the imaging

of pig thyroid gland, the 1.82 mm penetration depth was observed in low speckle image. We confirmed the improvement of penetration depth for the developed speckle-reduced OCT. The quantitative parameters SNR, C, and CNR were increased by at least 2 dB, 20, and 2 dB, respectively, which corroborated the improved speckle-reduced imaging results.

Reference for Chapter 6

[1] J. M. Schmitt, S. H. Xiang, and K. M. Yung, "Speckle in optical coherence tomography," *J. Biomed. Opt.* **4**(1), 95-105(1999).

[2] M. Bashkansky, and J. Reintjes, "Statistics and reduction of speckle in optical coherence tomography," *Opt. Lett.* **25**(8), 545-547(2000).

[3] B. Karamata, K. Hassler, M. Laubscher, and T. Lasser, "Speckle statistics in optical coherence tomography," *J. Opt. Soc. Am. A* **22**(4), 593–596 (2005).

[4] H. Cheong, S. K. Devalla, T. Chuangsuwanich, T. A. Tun, X. Wang, T. Aung, and M. J. Girard, "OCT-GAN: single step shadow and noise removal from optical coherence tomography images of the human optic nerve head," *Biomed. Opt.Express*, **12**(3), 1482-1498 (2021).

[5] S. K. Devalla, G. Subramanian, T. H. Pham, X. Wang, S. Perera, T. A. Tun, and M. J. Girard, "A deep learning approach to denoise optical coherence tomography images of the optic nerve head," *Sci. Rep.*, **9**(1), 14454 (2019).

[6] W. Drexler, and J. G. Fujimoto, "Optical Coherence Tomography: Technology and Applications" Vol. 2. Berlin: Springer, 2015.

[7] J. W. Goodman, Speckle phenomena in optics (W. H. Freeman, 2010).

[8] G. J. Tearney, M. E. Brezinski, B. E. Bouma, S. A. Boppart, C. Pitris, J. F. Southern, and J. G. Fujimoto, "In Vivo Endoscopic Optical Biopsy with Optical Coherence Tomography," *Science* **26.6**(5321), 2036.2039 (1997).

[9] A. Z. Freitas, D. M. Zezell, N. D. Vieira Jr, A. C. Ribeiro, and A. S. L. Gomes, "Imaging carious human dental tissue with optical coherence tomography," *J. Appl. Phys.* **99**(2), 024906 (2006).

[10] X. Li, J. Yin, C. Hu, Q. Zhou, K. K. Shung, and Z. Chen, "High-resolution coregistered intravascular imaging with integrated ultrasound and optical coherence tomography probe," *Appl. Phys. Lett.* **97**(13), 133702 (2010).

[11] A. E. Desjardins, B. J. Vakoc, W. Y. Oh, S. M. R. Motaghiannezam, G. J. Tearney, and B. E. Bouma, "Angle-resolved Optical Coherence Tomography with sequential angular selectivity for speckle reduction," Opt. Express **15**(10), 6200–6209 (2007).

[12] R. Říha, M. J. Marques, M. R Hughes, A. Bradu, and A. Podoleanu, "Direct en-face, speckle-reduced images using angular-compounded Master–Slave optical coherence tomography," *J.Opt.* **22**(5), 055302(2020).

[13] M. Pircher, E. Go¨tzinger, R. Leitgeb, A. F.Fercher, and C. K.Hitzenberger, "Speckle reduction in optical coherence tomography by frequency compounding ," *Biomed. Opt. Express* **8**(3),565-569 (2003).

[14] C. Magnain, H. Wang, S. Sakadžić, B. Fischl, and D. A. Boas, "En face speckle reduction in optical coherence microscopy by frequency compounding," *Opt. Lett.* **41**(9), 1925-1928(2016).

[15] R.Li, H. Yin, J. Hong, C.Wang, B.He, Z. Chen,and X.Zhang , "Speckle reducing OCT using optical chopper," *Opt. Express* 28(3), 4021-4031 (2020).

[16] O. Liba, M. D. Lew, E. D. SoRelle, R. Dutta, D. Sen, D. M. Moshfeghi, and A. de La Zerda, "Speckle-modulating optical coherence tomography in living mice and humans," *Nature communications* **8**(1),1-13(2017).

[17] D. C. Adler, T. H. Ko, and J. G. Fujimoto, "Speckle reduction in optical coherence tomography images by use of a spatially adaptive wavelet filter," *Opt. Lett.* **29**(24), 286.8–2880 (2004).

[18] N. Lippok, P. Nielsen, and F. Vanholsbeeck, "Single-shot speckle reduction and dispersion compensation in optical coherence tomography by compounding fractional Fourier domains," *Opt. Lett.* **38**(11), 16.86.16.89 (2013).

[19] A. Ozcan, A. Bilenca, A. E. Desjardins, B. E. Bouma, and G. J. Tearney, "Speckle reduction in optical coherence tomography images using digital filtering," *J. Opt. Soc. Am.* **24**(7), 1901–1910 (2007)

[20] H. Yu, J. Gao, and A. Li, "Probability-based non-local means filter for speckle noise suppression in optical coherence tomography images," *Opt. Express* **41**(5), 994–997 (2016).

[21] C. Cuartas-Vélez, R. Restrepo, B. E. Bouma, and N. Uribe-Patarroyo, "Volumetric non-local-means based speckle reduction for optical coherence tomography," *Biomed. Opt. Express* **9**(7),3354-336.2(2018).

[22] X. Zhang, Z. Li, N. Nan, and X.Wang, "Denoising algorithm of OCT images via sparse representation based on noise estimation and global dictionary," *Opt. Express* **30**(4), 56.88-5802 (2022).

[23] G. Gong, H. Zhang, and M. Yao, "Speckle noise reduction algorithm with total variation regularization in optical coherence tomography," *Opt. Express* **23**(19), 24699–246.12 (2015).

[24] G. Zhang, and W. Wei, "4-D Imaging of Beating Tissues Using Optical Coherence Tomography," *IEEE Photonics Journal*, **13**(3), 1-11 (2021).

Chapter 7 Conclusions

7.1 Summary of this thesis

In this thesis, the realization of multi-functional OCT with equipment of 1.7 μm quasi-SC source for both high-resolution deep tissue imaging and speckle reduced imaging has been investigated.

The detailed conclusions are summarized in the sequence of the chapters in the following:

In Chapter 1, the background of this thesis has been introduced. At first, the background of OCT has been presented. Next, the development of OCT has been introduced with respect to the imaging speed, sensitivity, spatial resolution, penetration depth, and imaging contrast. The development in these aspects relies on innovations in SD-OCT detection methods, and the choice of light sources. Finally, the purpose and overview of this thesis were presented.

In Chapter 2, the theory of optical coherence tomography, which is based on the Michelson interferometer used in this study has been presented. The fundamental theory of interferometer with low-coherence light was explained at first. Then, the basic characteristics of the interferometer for imaging such as imaging range, lateral resolution, confocal gating, and lateral resolution were described. The fundamental law governing the axial resolution, which depends on the full width at half maximum (FWHM) of the interference signal and its shape, was shown to be inversely proportional to spectral bandwidth of the used light source. The principles of time-domain (TD) OCT and Fourier-domain (FD) OCT were explained. The principle, axial resolution limitations, and detected sensitivity for spectral-domain (SD) OCT were explained in section 2.4. The speckle, an inherent property in OCT, which degrades the image contrast, was explained in section 2.5.

In Chapter 3, SC and quasi-SC generation for OCT has been presented. The developments of SC and quasi-SC were described. In addition, the optical nonlinear effects in fiber were introduced to understand spectrum broadening in supercontinuum. The theories of the ultrashort pulse propagation were described with various phenomena in optical fibers such as linear effect (absorption and dispersion) and nonlinear effect (self-phase modulation and stimulated Raman scattering and so on). The interplay of self-phase modulation (SPM) and group-velocity dispersion (GVD) which leads to the soliton pulse formation was described. The principle of wavelength tunable Raman soliton pulse was also described.

In Chapter 4, the development of a tunable quasi-supercontinuum generation at 1.7 μm spectral band has been demonstrated based on wavelength-tunable soliton pulse generation and fast intensity modulation. First, a 1.5 μm Er-doped ultrashort-pulse fiber laser using a SWNT polyimide film was used for seed pulse generation. The ultrashort pulse intensity was amplified to 360 mW of the maximum power by an EDFA to obtain a wider wavelength-tunable range from 1600 to 1900 nm. A fast intensity modulator has been inserted between the seed pulse source and EDFA to change PM fiber-input power continuously and rapidly. After a 300 m PM fiber, many newly shifted Raman solitons have been generated at almost the same time. The observed spectra seemed to be super-continuous. A quasi-SC with the bandwidths of 138 nm and the central wavelength of 1743 nm was obtained. We evaluated and compared the noise properties of quasi-SC, 1750 nm Raman soliton, and 1700 nm conventional SC. The generated quasi-SC exhibited similar noise characteristics compared to 1750 nm Raman soliton and 1700 nm SC below 100 kHz.

In Chapter 5, we investigated the SD-OCT performance and demonstrated the highly sensitive, high-resolution OCT imaging using broadband quasi-SC in the 1.7 μm spectral band. First, a Gaussian-shaped quasi-SC with a central wavelength of 1743 nm and a bandwidth of 138 nm was obtained. We connected the

quasi-SC to the SD-OCT system. Then, the characteristics of OCT imaging were examined in terms of sensitivity, axial resolution, lateral resolution, and imaging depth successively. We used a reflective mirror to examine the sensitivity and axial resolution. A total imaging sensitivity of 98 dB and an axial resolution of 10.7 μm in tissue sample were obtained. The sensitivity and axial resolution were also examined while tuning the bandwidth and modulation frequency of the quasi-SC source, and it was confirmed that the tunability of quasi-SC did not affect the OCT performance. We used a resolution target card to examine the lateral resolution by edge profile method, and the measured value was 33.5 μm. We evaluated the penetration depth in the reconstructed imaging of human teeth, and the superior penetration depths of 1.6 mm were obtained for quasi-SC. Finally, we successfully observed the cross-sectional image for samples of tape stacks, human fingertips, and the human fingernails. We also repeated the above experimental operations using the 1.7 μm conventional SC, which has spectral specifications to quasi-SC. The similar index and the compared images indicated that the quasi-SC source is as capable of highly sensitive high-resolution deep tissue imaging for biological samples as the SC source, and confirmed the availability of quasi-SC in realizing high-resolution deep tissue imaging.

In Chapter 6, we have demonstrated that a tunable quasi-SC source configured for OCT allowed us to obtain uncorrelated speckle patterns for speckle reduction via the spectral compounding method. First, we generated seven different quasi-SCs, and examined the characteristics of SD-OCT using quasi-SCs in terms of sensitivity and spatial resolution. Similar sensitivity at around 98 dB, close axial resolution at around 17 μm in tissue imaging and lateral resolution at around 33 μm were obtained by varied quasi-SCs. Then, we successfully demonstrated the speckle-reduced imaging for the samples of tape stacks and pig thyroid gland. The compounded images had a clearer structure as the speckle noise was suppressed. As the averaging number increased and the difference with the wavelength range became greater, the image quality improved. In tape stack imaging, correlation-coefficients were measured by pairs of initial images obtained by quasi-SC, and the result indicated effectiveness of speckle decorrelation with the spectral tunability. In the imaging of pig thyroid gland, the 1.82 mm penetration depth was observed in the lowest speckle image. We confirmed the improvement of penetration depth for the developed speckle-reduced OCT. The quantitative parameters SNR, C, and CNR were increased by at least 2 dB, 20, and 2 dB, respectively, which corroborated the improved speckle-reduced imaging results.

7.2 Outlook for the future

As mentioned above, we demonstrated that a tunable quasi-SC source configured for OCT enables us to realize both high-resolution deep tissue imaging and speckle-reduced imaging with the adjustable quasi-SC spectra.

However, there was a tradeoff between the high resolution and the degree of speckle reduction because of the limited spectral band used, 1600 nm to 1900 nm. A better speckle reduction result requires higher averaging numbers n and smaller overlaps between spectra, but a higher axial resolution needs a wider bandwidth spectrum. For future optimizations, the enlargement of wavelength-tunable range, may not only allow us to obtain a single wider bandwidth quasi-SC for ultrahigh resolution (~5 μm), but also enable more and wider quasi-SC spectra for speckle-reduced imaging.

In addition, the implementation of a high NA confocal lens in the sample arm, may help us to enhance both axial resolution and lateral resolution [1,2]. The high resolution and speckle-reduced 3D measurement will be applied to more biological imaging.

Finally, in the experimental scheme, we set the modulation amplitude and offset as parameters to adjust the central wavelength and bandwidth manually. It always takes several minutes. To reduce adjustment time for real-time speckle reduced imaging for living samples, we hope to realize the whole computer-controlled system for fast modulation adjustment of quasi-SC source and corresponding quick acquisition of OCT images.

Reference for Chapter 7

[1] M. Yamanaka, N. Hayakawa, and N. Nishizawa, "Signal-to-background ratio and lateral resolution in deep tissue imaging by optical coherence microscopy in the 1700 nm spectral band," *Scientific reports*, **9**(1), 16041(2019).

[2] M. Yamanaka, T. Teranishi, H. Kawagoe, and N. Nishizawa, "Optical coherence microscopy in 1700 nm spectral band for high-resolution label-free deep-tissue imaging," *Scientific reports*, **6**(1), 31715 (2016).

Acknowledgment

First and foremost, I would like to give my heartfelt thanks to my supervisor, Professor Norihiko Nishizawa, for his invaluable and continuous guidance, encouragement, helpful suggestion, and constructive discussion throughout my study. Furthermore, it is my honor to benefit from his personality and diligence, which I will treasure my whole life. I would like to thank Assistant Professor Shotaro Kitajima for his helpful comment in this study.

I am also extremely grateful to Associated Professor Masahito Yamanaka who gave me a lot of valuable guidance and advices.

Further, my hearty thanks are also given to all students who have studied in Nishizawa group for their kind support with which the present work has been successfully accomplished. I also thank to Ms. Shinobu Nakao, who is secretary of Nishizawa Group, for her kind help in daily life.

Finally, I am grateful to my family and my friends who always care and encourage me.

List of papers concerned with this thesis

1. Original paper

Title	Journal	Author (Related Chapter)
1. Tunable quasi-supercontinuum generation in a 1.7 μm spectral band for spectral domain optical coherence tomography	*Optics Continuum*, Vol.2, No.9, pp. 1941-1949 (2023)	Y. Chen M. Yamanaka N. Nishizawa (Chapter 4 and Chapter5)
2. Speckle reduced optical coherence tomography using tunable quasi-supercontinuum source	*Photonics,* Vol.2, No.12, pp.1338 (2023)	Y. Chen M. Yamanaka N. Nishizawa (Chapter 6)

2. International Conference

Title	Conference	Author
1. 1700-nm optical coherence microscopy with the reduced speckle noises for high-resolution deep tissue imaging	OSK-OSA-OSJ 2019 Joint Symposia on Optics, Busan, Korea (July 2019)	Y. Chen M. Yamanaka N. Nishizawa
2. Speckle reduction by spectral compounding in 1700 nm SD-OCT using tunable quasi-supercontinuum source	OPTICS & PHOTONICS International Congress 2022, SI-Thru6-06, Yokohama, Japan (April 2022)	Y. Chen N. Nishizawa
3. Speckle reduction by frequency compounding in 1.7 μm optical coherence tomography using tunable quasi-supercontinuum laser source	CLEO Conference 2022, W3B.152-1, San Jose, USA (May 2022)	Y. Chen S. Kitajima M. Yamanaka N. Nishizawa
4. High resolution and low speckle OCT imaging using quasi-supercontinuum laser source	The 12th Asia-Pacific Laser Symposium, GW1-03, Hakodate, Japan (September, 2023)	Y. Chen S. Kitajima N. Nishizawa